Energy Reports 8 (2022) 11607–11637

Contents lists available at ScienceDirect

Energy Reports

journal homepage: www.elsevier.com/locate/egyr

Review article

Promising transparent and flexible thermoelectric modules based on p-type CuI thin films—A review

Aicha S. Lemine [a,b], Jolly Bhadra [b,c], Noora J. Al-Thani [b], Zubair Ahmad [b,c,*]

[a] Department of Mechanical and Industrial Engineering, Qatar University, Doha 2713, Qatar
[b] Qatar University Young Scientists Center (QUYSC), Qatar University, Doha 2713, Qatar
[c] Center for Advanced Materials (CAM), Qatar University, Doha 2713, Qatar

ARTICLE INFO

Article history:
Received 10 May 2022
Received in revised form 14 August 2022
Accepted 7 September 2022
Available online xxxx

Keywords:
Thermoelectric
CuI
Thin films
Transparent
Flexible
Energy conversion

ABSTRACT

The state-of-the-art thermoelectric technology owns a unique capability of direct, noise-free, and efficient conversion of waste heat into valuable electricity. The conventional thermoelectric generators are complex and expensive in fabrication, which restricts their use in wearable and miniaturized electronics to fulfill the current and rapid growth in demands for sufficient self-powered energy harvesters. Herein, this comprehensive review paper highlights the promising and next-generation thermoelectric generators based on flexible, transparent, abundant, non-toxic, and lightweight p-type Copper Iodide (CuI) thin films. It introduces the principles of energy conversion within thin-film thermoelectric generators and the structure of p–n junction including the criteria in the selection of substrates, p-type and n-type materials, connecting electrodes, and modules designed to sustain its mechanical flexibility and optical transparency. This review underlines the morphology and properties of CuI thin-film thermoelectric generators to figure out the latest trends in advanced synthesis and characterization techniques. It draws attention to its promising applications in wearable biosensing, energy harvesting, and smart miniaturized electronics. It discusses also the challenges and prospects in boosting the thermoelectric performance of CuI thin-film generators. This targeting to exceed the unity in its Figure-of-Merit (ZT) values for excellent output power generation, large-scale production for commercialization, and long-term stability for reliable thermoelectric applications.

Contents

* Correspondence to: PO Box 2713, Doha, Qatar.
E-mail address: zubairtarar@qu.edu.qa (Z. Ahmad).

https://doi.org/10.1016/j.egyr.2022.09.020

1. Introduction

Nowadays, the rising costs of fossil fuel and their negative impacts on the environment is directing global attention towards the utilization of alternative renewable and sustainable energy sources (Klochko et al., 2021). This global attention is also driven by the incrementation in the world's population and energy consumption in various sectors (Yang et al., 2022). There is an emergent need for developing alternative technologies to attain the desired global energy and environmental security for current and future generations. Recently, the Thermoelectric (TE) technology has proven its pioneering performance among other renewable energy-based technologies leading to growing attention in its research publications, as displayed in Fig. 1. TE is a green energy competitor with unique capabilities in the energy conversion of waste heat into valuable electrical energy for thermal management and power generation (Zheng et al., 2014). It has attractive features such as solid-state, high reliability, no emissions of toxic gases, no moving parts, noise-free, long life, and low maintenance (Martín-González et al., 2013; Yang et al., 2021). It has been utilized extensively in different fields of energy sources, heating, refrigeration, temperature sensors, and semiconductors (Riffat and Ma, 2003).

The conventional power supply sources such as chemical batteries are not favorable for wearable and wireless electronics due to their expensive costs, large sizes, and complex operating mechanisms (Liu et al., 2010). The integration of TE devices into miniaturized, wireless, and wearable self-powering electronic devices requires flexibility and transparency properties (Jia et al., 2021). This draws the need of developing novel TE power supply technology based on energy harvesters exhibiting transparency, mechanical flexibility, and lightweight properties, as observed from the increasing publications trend in Fig. 1. The efficiency of the flexible TE harvesters in power generation is dependent on the type of energy source, generator performance, and size (Jouhara et al., 2021). The efficiency advancement of flexible TE modules should be based on the selection of earth-abundant and non-toxic raw materials, as well as adopting large-scale production techniques (Jaldurgam et al., 2021). This will facilitate their low production cost with adequate performance in comparison to TE devices based on rare and expensive raw materials such as Bismuth (Bi) and Tellurium (Te), which require more complex synthesis methods (Jaldurgam et al., 2021). Thus, the fabrication of low-cost TE with acceptable performance is more practical to be used broadly than producing a higher-performance TE device with an unexpected price and limited use (Kawazoe et al., 1997).

The fabrication of TE devices on a flexible and transparent substrate has an economical advantage in the marketplace and an improvement on the end-user lifestyle through smaller, more portable, less expensive, more flexible, transparent, and unlimited self-powering capabilities (Kawazoe et al., 1997). This describes the growing attention to the research field of transparent and flexible thermoelectrics, as shown in Fig. 1. The flexible TE generators could be fabricated in different modules to satisfy different power and design requirements of nano- and micro-energy applications for fast and large-scale production. The thin-film module has outstanding TE properties suitable for several miniaturization electronics (Wang et al., 2020a; Fan et al., 2015; Karthikeyan et al., 2020; Tappura and Jaakkola, 2018). The thin-film structure enables attaining TE materials with low dimensional quantum confinement leading to lower lattice thermal conductivity (Ma et al., 2021b). The addition of transparency to flexible thin-film TEs provides other routes for their further utilization in external glass walls/windows or electronic screens to harvest their waste heat (Ma et al., 2021b). The TE devices based on thin films of Copper Iodide (CuI) have exhibited an attractive TE efficiency in flexible and transparent applications as they possess high transparency with wide bandgaps, which reflects the incrementing publication trend on it in the field of transparent and flexible thermoelectrics, as shown in Fig. 1 (Jun et al., 2018; Lee et al., 2021). They owe also a long average free layer that reduces the scattering of charge carriers and leads to a rapid response speed than their bulk counterparts (Lee et al., 2021). Whereas the TE devices based on BiTe materials have recorded higher TE efficiencies but with much more expensive fabrication on large scale (Qiu et al., 2019). Currently, the preparation of low-cost and high-performance TE devices based on CuI thin films is an alternative approach to replace the TE devices based on expensive, rare, and toxic materials (Qiu et al., 2019).

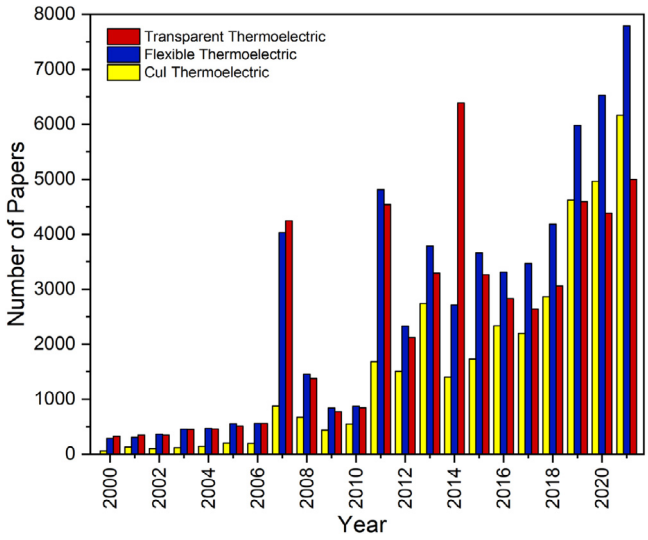

Fig. 1. The Number of papers published on transparent thermoelectric (red color), flexible thermoelectric (blue color), and CuI thermoelectric (yellow color) from 2000 to 2021.

Herein, this paper will review comprehensively the research works done on TE generators for flexible and transparent applications based on p-type CuI thin films. The paper aims to address the:

(a) Properties and characterization tools of structural, mechanical, optoelectronic, electrical, thermal, and thermoelectric properties correlated with CuI thin film-based TE devices.
(b) Synthesis techniques to integrate various modular designs of TE generators for the ideal fitting between flexibility and power requirements.
(c) Design module and drawbacks of conventional planar-structured TE devices compared to flexible TE modules.
(d) Proper selection of TE components including substrates, p-type, n-type, and connecting electrodes to match the flexible and transparent power requirements.
(e) Promising applications of p-type polycrystalline γ-CuI thin film TE devices in wearable biosensing, energy harvesting, and smart miniaturized electronics.
(f) Existing challenges and the future trends in advancing the performance of CuI thin film-based TE devices.

2. Thermoelectric CuI thin films properties and characterizations

The remarkable properties of the promising polycrystalline γ-CuI p-type thin-film for transparent and flexible TE modules are investigated via a set of advanced characterization techniques to satisfy tremendous potential TE applications as follows:

2.1. Structural and morphology

The structural and morphological properties of thin-film p-type CuI are frequently characterized before their TE application using the X-ray diffraction patterns (XRD), Field Emission Scanning Electron Microscopy (FE-SEM), Atomic Force Microscopy (AFM), and Raman Spectroscopy (Hamid Elsheikh et al., 2014). The typical XRD patterns of γ-phase CuI thin films grown on a flexible PET substrate showed diffraction lattice planes of (111), (200), (220), (311), and (331) at peaks 25°, 30°, 42°, 50°, and 67°, respectively, as displayed in Fig. 2a (Yamada et al., 2017). These diffraction peaks are consistent with the standard peaks of γ-phase CuI film in the Joint Committee on Powder Diffraction Standards (JCPDS no. 10-897-072) (Yue et al., 2017). The dominant diffraction plane of (111) is frequently detected for the γ-phase CuI films due to its facile growth along the direction of <111> (Yue et al., 2017). The presence of plane (220) indicates the absence of an annealing post-treatment process for the deposited γ-CuI films (Yue et al., 2017). This suggests the important role of annealing heat treatment on the grain growth along with particular orientation. The undetectable of any additional peaks in XRD patterns of CuI reveals the disidentification of any other phases in particular the copper oxidations as Cu_2O or CuO (Yang et al., 2016c).

The Debye–Scherrer semi-empirical Eq. (1) is frequently reported for the calculation of crystallite size (D) for CuI films (Baerlocher and Mccusker, 1994):

$$D = \frac{0.9\lambda}{\beta \cos\theta} \tag{1}$$

Where the λ is the wavelength of the X-rays typically 1.789 Å, the β is full width at half maximum (FWHM) in radians for the highest intensity diffraction plane (111), and θ is the Braggs angle in radians (Baerlocher and Mccusker, 1994). The typical crystallite size of the as-deposited γ-CuI film is reported to be around 38.6 nm and undergoes growth with annealing at 250 °C to 49.9 nm (Kim et al., 2014a). This average grain size is commonly compared to that determined from the FE-SEM micrographs utilizing the ImageJ software and is found to be around 44 nm, as presented in Fig. 2b (Yamada et al., 2017). This FE-SEM micrograph shows the homogeneous compact structure without cracks or voids and composed of crystalline grains with lateral diameters ranging from 200 to 300 nm. The typical unit cell of γ-CuI could be expected from the calculations on XRD data, as demonstrated in Fig. 2c (Yamada et al., 2017). The resultant is a cubic face-centered (FCC) unit cell with a lattice parameter of 0.599 nm. The I anions are positioned at the vertices of FCC and Cu cations positioned on 1/4, 1/4, 1/4, and at the center of the tetrahedron (Yamada et al., 2017). Additionally, the film topography is more insight using the AFM characterization technique, as shown in Fig. 2d (Yamada et al., 2017). The typical values of RMS roughness are reported in the range of 22–27 nm for CuI/PET, which is twice the values of CuI films deposited on the rigid glass substrate (O'Dwyer et al., 2017).

The Raman spectrum with laser excitation of 532 nm has been examined for thin films of CuI deposited on a quartz substrate, as displayed in Fig. 2e (Kaushik et al., 2017). The Raman of γ-phase CuI semiconductor indicates its phonons vibration modes, which are the longitudinal optic (LO) and transverse optic (TO). The TO vibration mode of Cu-I bonding vibration in a thin film of CuI is observed at 125/cm, while the LO peak is at 140/cm, which could be partially merged into the wide TO peak (Murmu et al., 2021). The disorder of the CuI film structure is attributed to the broadening of the TO peak. The additional peak noticed at 485/cm characterizes the Raman signal of the quartz substrate (Murmu et al., 2021). This Raman spectrum of CuI film coincides with XRD patterns in differentiating it from other copper oxidation spectra of CuO and Cu_2O, which further could assist in eliminating the oxidation of CuI film during its synthesis. The microstructure and thickness of fabricated CuI films could be investigated by cross-sectional FE-SEM analysis. Fig. 2f shows the cross-sectional FE-SEM image of γ-CuI film revealing its columnar growth and average thickness of 500 nm (Krishnaiah et al., 2021).

2.2. Mechanical properties

The flexibility of TE devices based on thin films is investigated through their bending properties and stability at consecutive cycles of bending using a homemade bending machine, as demonstrated in Fig. 3a (Coroa et al., 2019). This setup is built up with in-situ resistance measurements dependent on the bending radius. In each cycle, the critical bending radius corresponds to the bending curvature radius upon which the resistance reaches 5%–10% of its original value. Thus, its system involves 2 grips, one of which is connected to the stage undergoing forth and back movements in minimal step incrementation of 0.01 mm. Whereas the other one is connected to the fixed arm holding the sample at the substrate end. The substrate at its initial length (L) is bent to a bending length expressed as L-dL with a bending radius (r) in the center of the sample, which is calculable based on Eq. (2) (Coroa et al., 2019).

$$r = \frac{L}{2\pi\sqrt{\frac{dL}{L} - \frac{\pi^2 h^2}{12L^2}}} \tag{2}$$

Where L is the initial sample length, dL/L is the rate of change in length of the sample, and h is the total thicknesses of the film (t_f) and substrate (t_s). The bending flexibility of n-type GZO and p-type CuI semiconducting thin films on Kapton substrate have been characterized individually by tensile and compressive analysis, as demonstrated in Fig. 3b and c (Coroa et al., 2019).

The CuI thin films subjected to a tensile force have shown a linear degradation of electrical resistance with the incrementation in the number of bending cycles to 80 cycles and then initiation of a plateau in R change, as illustrated in Fig. 4a (Coroa et al., 2019). The CuI films subjecting to compressive forces exhibited a maximum of 3.6% in R_0at full 100 bending cycles. This

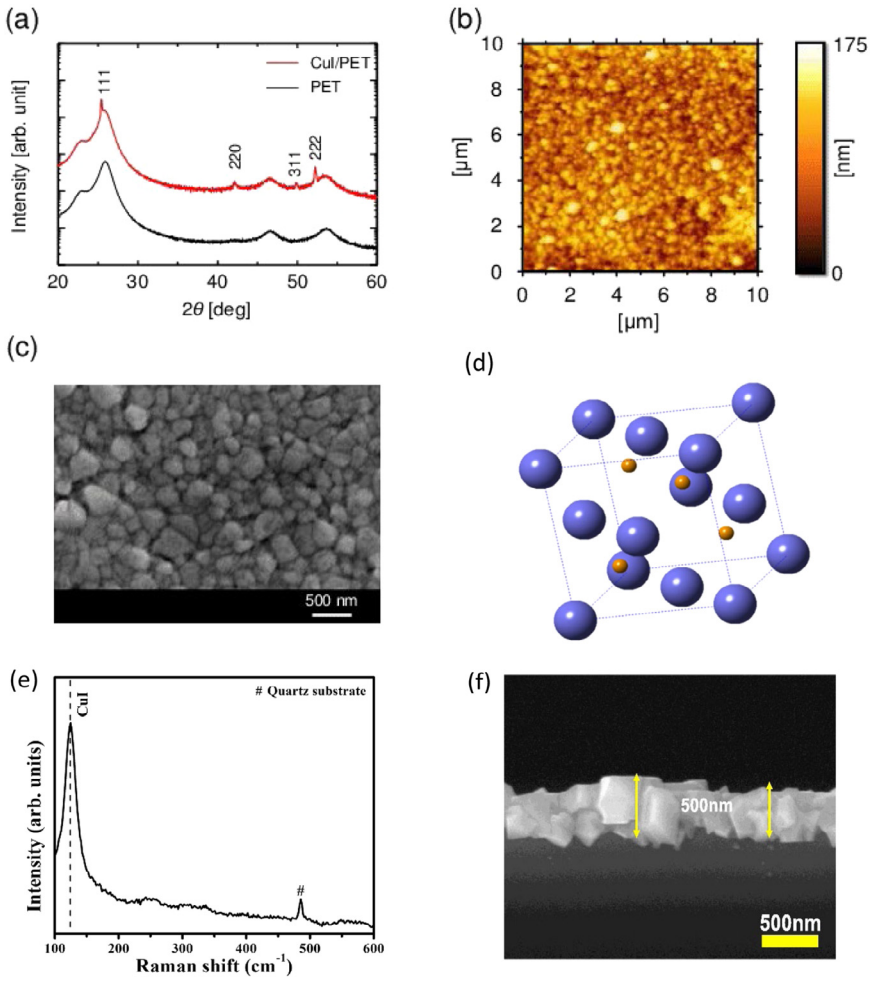

Fig. 2. The Structural and morphological characterizations of CuI films using (a) X-ray diffraction patterns, (b) AFM images of CuI film deposited on PET substrate, and (c) Top view FE-SEM surface image (Yamada et al., 2017), with permission of Wiley Online Library, copyright 2017. (d) A unit cell of γ-CuI (Faustino et al., 2018), with permission of Springer Nature, copyright 2018. (e) Raman spectrum of CuI film deposited on quartz substrate (Kaushik et al., 2017), with permission of Elsevier Ltd., copyright 2017. (f) Cross-sectional FE-SEM image of as-deposited CuI on Si/SiO_2 substrates (Krishnaiah et al., 2021), with permission of Elsevier Ltd., copyright 2021.

is referred to as the columnar grains of CuI imposed on the compressive forces causing additional compaction of its lattice and then facilitating the electron flow (Hu et al., 2021a). While the tension forces on CuI disrupt its lattice and result in the formation of film cracks, which limited the flow of electrons (Hu et al., 2021a). The CuI thin films exposed to compressive forces after 100 tension cycles have reduced 7.1% of its R_{int} compared to one compressive cycle (Coroa et al., 2019). The lowest value of R_{int} has been observed after 13 compression cycles and yields around 0.4% of the change in resistance value from its R_0 before the application of tensile forces. The additional compression of CuI film led to a minor rise in the R_{int} value at 100 cycles. This does not apply to CuI film that has not undergone the tension forces and then R_{int} remains stable after 100 cycles.

The GZO thin films exhibited a dissimilar behavior to the CuI films due to their ceramic nature owing to their compact structure causing a varied resistance in high sensitivity to the compression than tension forces, as displayed in Fig. 4c (Coroa et al., 2019). In the tension mode of GZO, the resistance has increased due to the growth of moderate superficial cracks across the film without deep adequate cracks that will obstruct the flow of charge carriers (Yang et al., 2022). The subsequent compression of GZO films following its tensile cycles has caused the formation of cracks in the contradictory face of the film, which is in contact with the substrate. This has disturbed the remaining carriers' flow in-depth, as shown in Fig. 4d (Coroa et al., 2019). Inclusive, thin films of CuI deposited on flexible and transparent Kapton substrate have shown over 100 bending cycles a remarkable minimized resistance variation irrespective of the applied bending mode as it has never surpassed 10% (Coroa et al., 2019). The deposition of CuI films on PET substrate has shown also improved electrical conductivity under compressive stress, while it undergoes degradation with tensile stress (Labonte et al., 2017). This is referred to as the enhancements in the compactness of grains at the compressive strain in polycrystalline CuI thin films (Labonte et al., 2017). This further confirms that the TE modules based on CuI thin films have suitable mechanical flexibility for implementation onto thermal energy sources in curved structures such as clothes (Rousti et al., 2021), human bodies (Dey et al., 2016), and hot-water tubes (Tervo et al., 2009).

2.3. Optoelectronic properties

The CuI has frequently been characterized as a p-type semiconductor with a wide band and high transmittance exceeding 70% in the visible spectrum (Sirimanne et al., 2003). It owns a good absorption in a direct bandgap of 3 eV at which the free excitons undergo recombination with a strong contribution of Cu vacancy defects to its band transport (Sirimanne et al., 2003). These optoelectronic properties of CuI are typically characterized

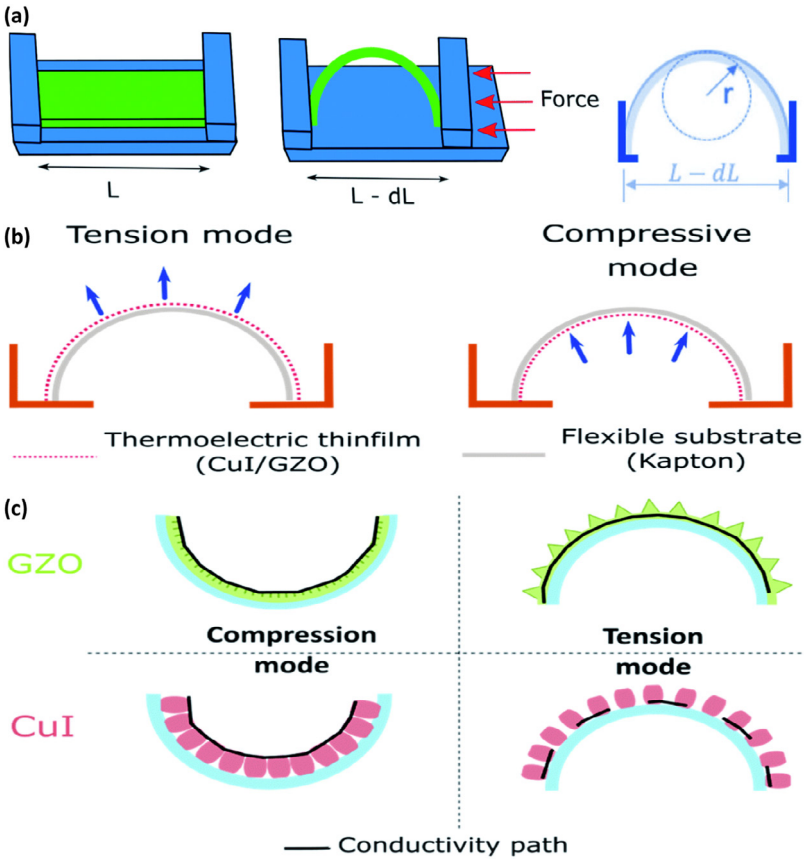

Fig. 3. The Schematics of (a) a homemade bending machine with bending radius (r) obtained for every displacement (L-dL) and two conductive wires connected to the sample ends for its resistance measurements. (b) The bending analysis of CuI/GZO thin films grown on flexible Kapton substrate under tension and compressive forces. (c) The conductivity path of CuI and GZO at tension and compression modes (Coroa et al., 2019), with permission of RSC Adv., copyright 2019.

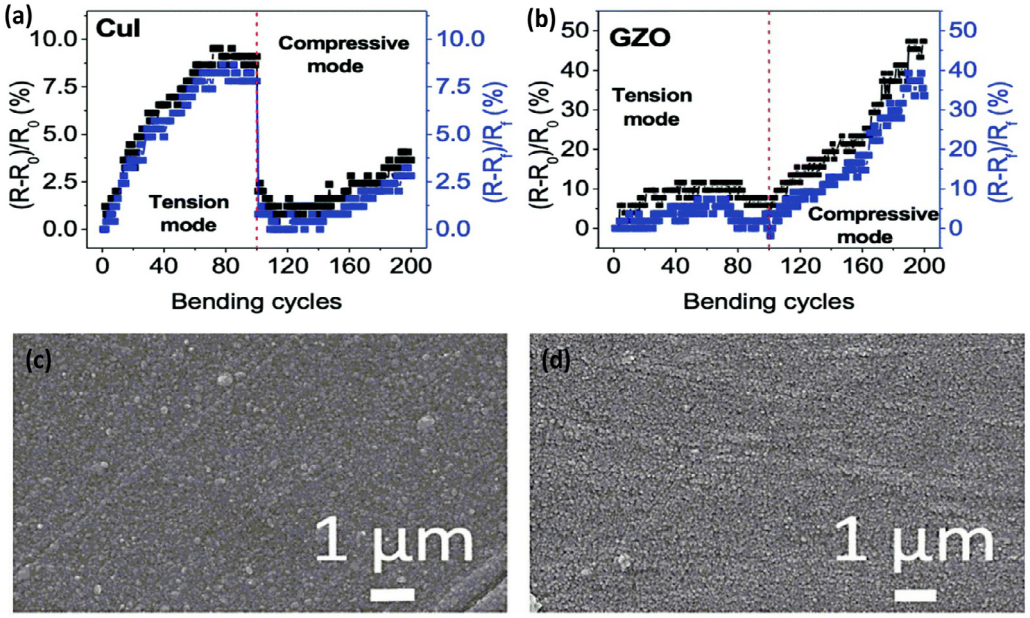

Fig. 4. The Mechanical characterization of flexible TE device based on CuI/GZO films grown on Kapton (CS) substrate. The bending properties of (a) CuI and (b) GZO thin films at 100 consecutive cycles in tension mode followed by 100 consecutive cycles in compressive mode. The corresponding SEM micrographs of (c) CuI and (d) GZO thin films (Coroa et al., 2019), with permission of RSC Adv., copyright 2019.

using UV–visible transmission measurements in a wavelength range of 400 to 430 nm, as displayed in Fig. 7a (Zhang et al., 2019). The optical band gap of CuI film is calculated utilizing the relationship between the intrinsic absorption coefficient (α) and

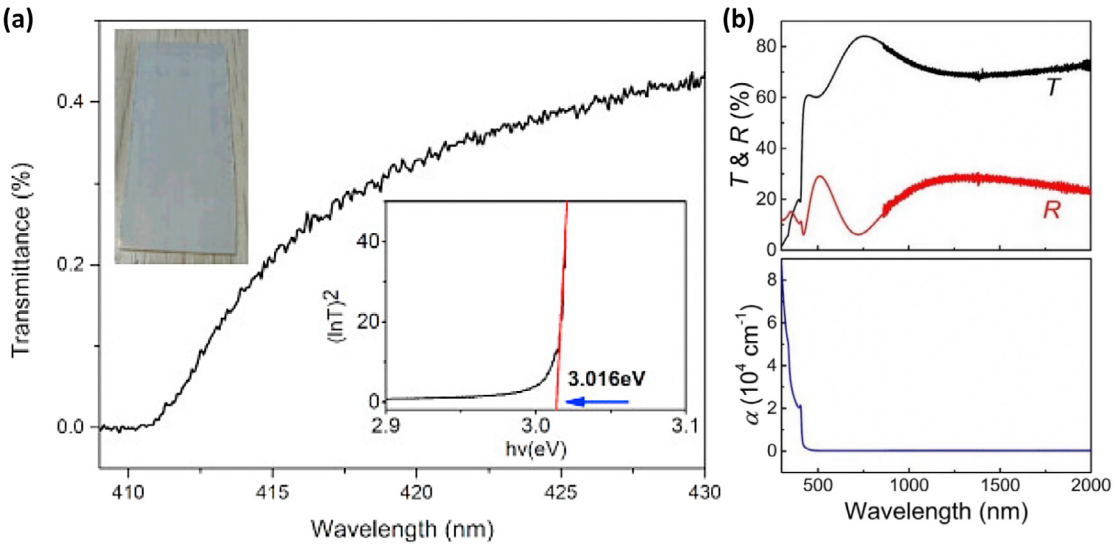

Fig. 5. (a) The UV–VIS spectrum for optoelectronic characterization of flexible and transparent γ-CuI p-type thin film deposited on a soda-lime glass substrate by magnetron sputtering technique and the inset is its optical band gap energy based on the second-order derivative of transmission spectrum (Zhang et al., 2019), with permission of Elsevier Ltd., copyright 2019. (b) The Optoelectronic properties of intrinsic absorption coefficient (α), reflectance (R), and Transmittance (T) for the γ-CuI film deposited on glass substrate using reactive sputtering technique (Yang et al., 2016a), with permission of Proc. Natl. Acad. Sci., copyright 2016.

(hv) using Eq. (3) (Gong and Krishnan, 2019):

$$\alpha = \frac{1}{t} \ln\left(\frac{(1-R)^2}{T}\right) \tag{3}$$

Where the T is the transmittance of CuI film, t is the thickness of the film, and R is the reflectance and it is neglected if R≪1. The absorption coefficient (α) is given by the Tauc relation in Eq. (4) (Gong and Krishnan, 2019):

$$(\alpha hv)^2 = A\left(hv - E_g\right) \tag{4}$$

Where the hv is the photon energy, A is the absorbance, and E_g is the optical bandgap. The E_g of CuI film is found to be 3.016 eV, as demonstrated in the inset of Fig. 5a (Zhang et al., 2019). This satisfies the requirement of E_g>3 eV for transparent TE applications (Garner et al., 2019). It is reported that the transmittance of CuI film varies with its deposition method (Van Toan et al., 2020). For instance, the deposition of CuI using the thermal evaporation method resulted in higher transmittance of 80% in the wavelength of 400–800 nm compared to the iodination method (Dong et al., 2019).

This is referred to as the effect of film roughness, which is in the range of 80–100 nm for the iodination method exceeding the thermal evaporation method with smaller roughness close to 8 nm (Dong et al., 2019). Thus, the surface roughness of the film has a direct contribution to its scattering properties of light leading to alteration in the transmission properties of CuI thin film (Malik and la Hidalga-Wade, 2017). Additionally, the deposited CuI thin films on glass substrate using the reactive sputtering technique have shown a higher transmittance of 60%–85% within the wavelength range of 400–800 nm, as displayed in Fig. 5b (Yang et al., 2016a). This is slightly lower than the typical transmittance of n-type transparent semiconductors reaching 80%–90% (Mehta et al., 2012). This could be attributed to the strong reflections at the film/substrate interface and the surface of the films (Mehta et al., 2012). While the intrinsic absorption coefficient of CuI thin films has shown a very small α<200/cm at a wavelength of 450 nm, as presented in Fig. 5b (Yang et al., 2016a). This points to the remarkable transparency of CuI thin films in the near-infrared (NIR) and visible wavelength regions (Amalina et al., 2013). Recently, the doping of CuI thin films with metal ions such as Zn, Al, and Pb using the SILAR method has affected directly the morphology of CuI films resulting in a noteworthy change in its surface roughness, which in return changed its transmission behavior (Chen et al., 2021c).

2.4. Electrical properties

The first reported CuI thin films by Bädeker in 1907 have shown a relatively low electrical resistivity of $4.5^{*}10^{-2}$ Ω cm in a thickness of 200–300 nm with full transparency in the visible light range (Chu et al., 2020). The CuI films have exhibited p-type semiconductor at its stable zincblende phase (γ-CuI) at temperatures below 350 °C (Wang et al., 2020a). Then its crystal structure transforms in temperatures of 350–380 °C to wurtzite phase (β-CuI) and at higher temperatures to the rock salt phase (α-CuI) (Wang et al., 2020a). The α- and β-CuI films are conductors due to the moveable Cu ions (Wang et al., 2020a). While the γ-CuI phase is semiconductor with valence band maximum (VBM) consisting of hybridization orbitals of I 5p and Cu 3d, as well the V_{cu} forming shallow acceptor states directly on top of the VBM, as demonstrated in Figs. 6a and b (Liu et al., 2021). The lowest conduction band minimum (CBM) in CuI film is based on Cu-s states (Liu et al., 2021). The adequate intersection between the adjacent I 5p orbitals intervening in a Cu 3d orbital resulted from the bulky spatial spread of I 5p orbitals. This has led to minor hole effective mass around $m_h = 0.3m_e$ and returned to higher electrical mobility across CuI film (Mehdizadeh Dehkordi et al., 2015). The acceptor states contribute to such enhanced mobility via providing the hole–electron delocalization above the valence bands (VB). The Cu 3d orbital controls the electronic properties of CuI, while the filled d^{10} states and s^2p^6 shells derive their VB (Liu et al., 2021). Thus, the absorption occurs at the direct bandgap of 3eV allowing the recombination of free excitons, and the V_{Cu} defects contribute dominantly to the band transport (Mehdizadeh Dehkordi et al., 2015).

Recently, the CuI in amorphous structure has shown an identical hole effective mass and VBM bonding state to the crystalline phase, as illustrated in Fig. 6c (Liu et al., 2021). The tetrahedral structure is observed for a network of amorphous CuI with 2-center bonds of I and Cu sp^3 hybrids. It has 3 neat-degenerate states consistent VBM with less sensitivity to structural disorder due to its Cu-I-Cu unit. The V_{Cu} in γ-CuI exhibited the minimum

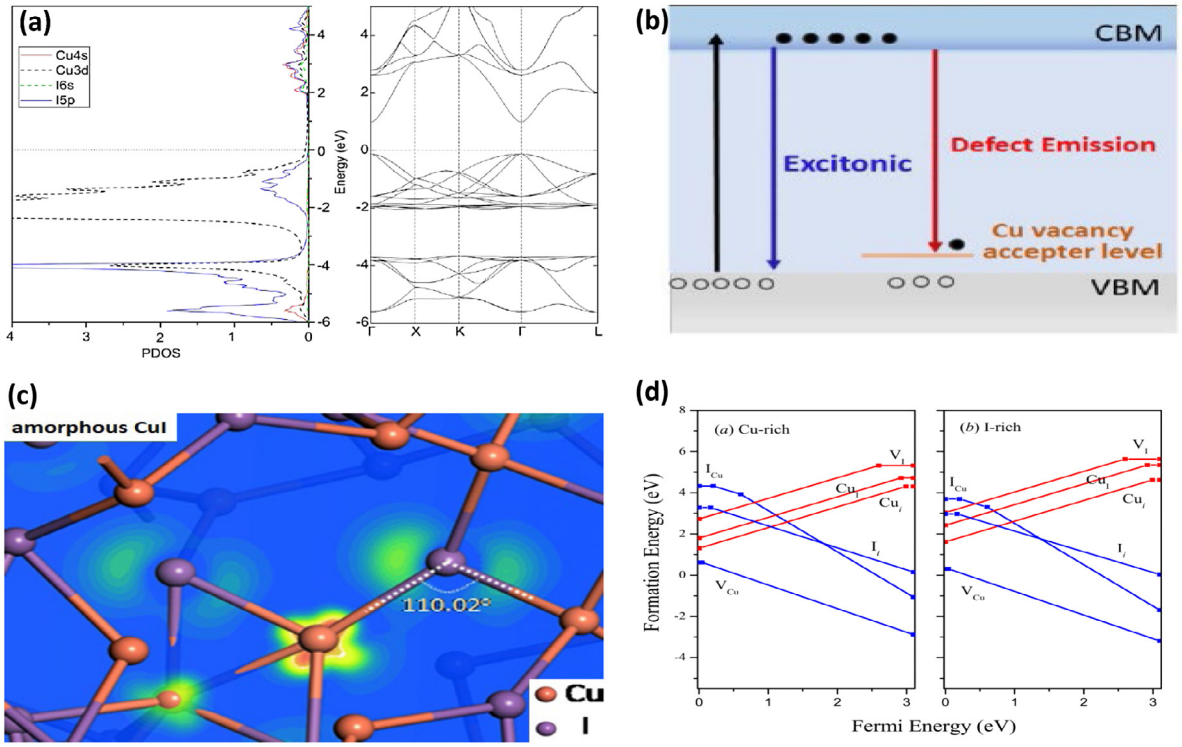

Fig. 6. The Electrical characterization of γ-CuI thin films using (a) the band structure and corresponding projected density of state (PDOS) (Kurtoglu et al., 2012), with permission of IOP Publishing Ltd., copyright 2012. (b) Photoluminescence emission band structure of thin-film γ-CuI besides Cu acceptor states (Annadi et al., 2019), with permission of American Chemical Society, copyright 2019. (c) The wave function of the VBM state in an amorphous CuI (Zhang et al., 2020b), with permission of American Physical Society, copyright 2020. (d) Formation energies of native defect calculated at the Cu-/I-rich condition (Wang et al., 2011a), with permission of AIP Publishing, copyright 2011.

formation/ionization energy either in I- or Cu-rich equilibrium growth circumstances based on first-principals pseudopotential calculations, as presented in Fig. 6d (Liu et al., 2021). This low formation energy of V_{Cu} is referred to as the VBM with antibonding character to high-energy d^{10} orbitals compared to other defects such as Cu interstitial (Cu_i), Cu antisite (Cu_I), I vacancy (V_I), I antisite (I_{Cu}), and I interstitial (I_i) (Tan et al., 2014). Whereas the antibonding above the VB has shown tolerance to crystallographic defects and then reserving the optoelectronic properties even in the existence of defects (Bai et al., 2021). This defect tolerance ability is further aided by the giant iodine anion having a small coordination number of around 2 (Bai et al., 2021). This facile formation of V_{Cu} advantaged the deposited thin films of γ-CuI in exhibiting high conductivity and large hole concentrations of 10^{17}–10^{20}/cm^3 (Lee et al., 2020a). This has overcome the bulk single crystal of CuI showing carrier mobility, concentration, and resistivity of 12.81 cm^2/V s, 4.08*10^{16}/cm^3, and 11.97 Ω cm, respectively (Lee et al., 2020a). These electrical properties are characterized frequently using the 4-point electrical conductivity and Hall effect measurements, as summarized in Table 1 (Yamada et al., 2016; Klochko et al., 2019b). Additionally, the γ-CuI has a stable cubic structure facilitating its depositions using different techniques at low temperatures (Tappura and Jaakkola, 2018). This promising characteristic of unstrict deposition conditions for CuI thin films makes it a satisfactory candidate for transparent TE applications based on large-scale production.

2.5. Thermal properties

The thermal conductivity (k) of p-type CuI semiconductors involves two main contributions of phonon thermal conductivity (k_{ph}) and electronic thermal conductivity (k_e) (Carvalhaes-Dias et al., 2018). The last is generated for the heat transfer of holes and electrons flow, while k_{ph} is caused by the phonons scattering. The k is calculated based on Wiedemann–Franz law as shown in Eq. (5) (Yadav et al., 2019):

$$k = k_e + k_{ph} = \sigma LT + k_{ph} \quad (5)$$

Where T is the absolute temperature, σ is the electrical conductivity, and L is the Lorenz factor equivalent to 2.4*10^{-8} W Ω/K^2 and 1.5*10^{-8} W Ω/K^2 for ideal metals and ideal non-degenerate semiconductors, respectively (Yadav et al., 2019). The γ-CuI is considered as a non-degenerated semiconductor and then its k_e varies in the range of 002–0.06 W/m K depending on hole concentration (p), as displayed in Fig. 7a (Liu et al., 2021).

This figure shows the slight incrementation in k values with increasing the p of CuI film. Whereas the value of K_{ph} does not depend on variations in electrical properties of CuI film. Recently, the CuI thin film deposited on a glass substrate has exhibited the lowest total k of 0.55 W/m K at room temperature with a power factor (PF) reached 3.75*10^{-4} W/m K^2 (Junior et al., 2018). This k is much lower than that of phonon-liquid material Cu_2Se on glass with k around 1.0 W/m K at RT (Liu et al., 2013). Thus, the k_{ph} is commonly eliminated in values close to 0.5 W/m K, which is attributed to the strong phonon scattering at grain boundaries of polycrystalline γ-CuI thin films, as well as the heavy element iodine (Yang et al., 2017b). The prototype of a transparent and flexible TE module based on the γ-CuI thin film has shown an ultrahigh power density reaching 2.4 mW/cm^2 in a temperature difference (ΔT) close to 50 K, as presented in Fig. 7c (Liu et al., 2021). The taken infrared image during these measurements displays the electrical contacts in cold due to their different emissivity in comparison to the CuI film sample, as exposed in Figs. 7b and d (Liu et al., 2021).

Table 1
The Hall effect measurements of hole transport properties for the most common transparent p-type semiconductors (Yamada et al., 2016; Klochko et al., 2019b).

Material	Form	Growth temperature [°C]	Hall mobility (μ_H) [cm^2/V s]	Hole concentration (n_P) [1/cm^3]	Band gap (E_g) [eV]
γ-CuI	Poly. film	RT	2.4	$8.6*10^{19}$	3.1
γ-CuI	Poly. film	150	9.0	$9.2*10^{17}$	3.1
γ-CuI	Bulk crystal	150–180	43.9	$4.3*10^{16}$	3.1
γ-CuI	Bulk crystal	60	12.81	$4.08*10^{16}$	3.1
$CuAlO_2$	Poly. film	700	10.4	$1.3*10^{17}$	3.5
$SrCu_2O_2$	Poly. film	300	0.46	$6.1*10^{17}$	3.3

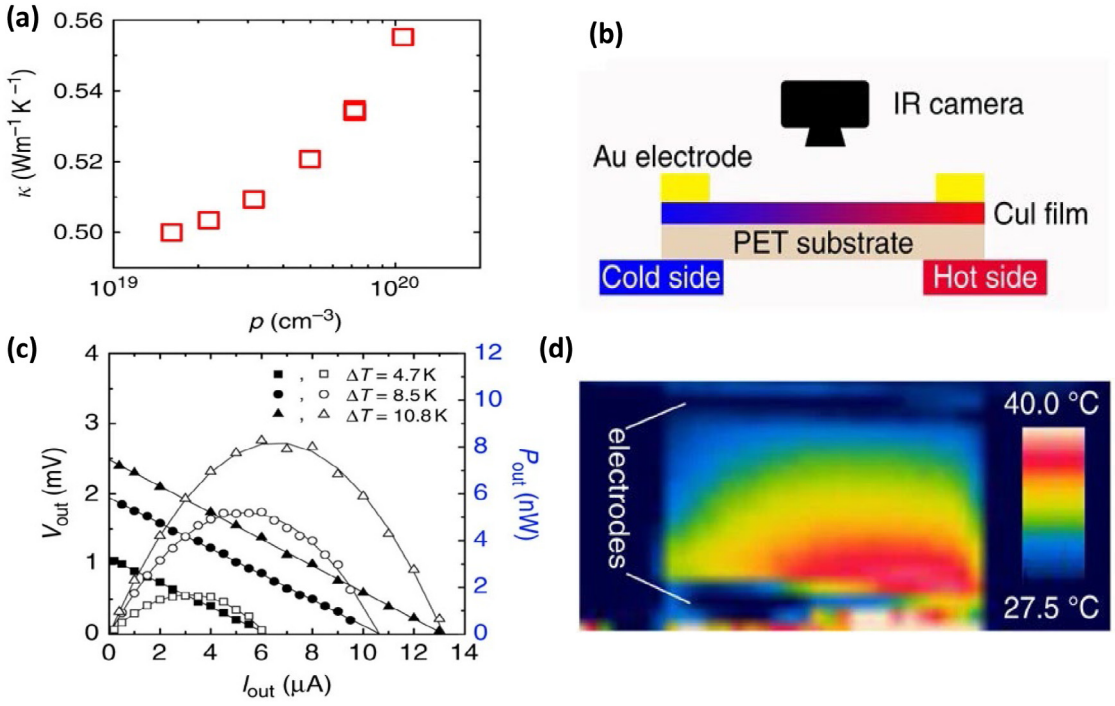

Fig. 7. The Single-leg TE module based on a γ-CuI thin film deposited on PET substrate: (a) Thermal conductivity (k) dependence on hole concentration (p) at 300 K, (b) schematic of output power (P_{out}) measurements, (c) output voltage (V_{out}) and P_{out} in terms of output current (I_{out}) at three diverse temperature gradients, and (d) taken infrared image for one of the measurements (Yang et al., 2017b), with permission of Springer Nature, copyright 2017.

2.6. Thermoelectric properties

The γ-CuI growth at iodine-rich conditions has advantaged in increasing the p-type conductivity considering the dominated V_{Cu} (He and Tritt, 2017). The highest electrical conductivity for p-type CuI is 283 S/cm obtained through the sputtering technique at controlled iodine partial pressure, which is observed to increase the electrical conductivity of deposited CuI films, as presented in Fig. 8a (Liu et al., 2021). This conductivity has not changed in the air but has degraded during the storage of CuI films for 3 months (Liu et al., 2021). The TE performance of deposited CuI is frequently quantified based on calculations of either dimensional or non-dimensional Figure-of-Merit denoted as FOM and ZT, respectively (Li et al., 2017a). As previously discussed, the α is calculated in the total visible transmission region of spectra and corrected for reflectance (Yang et al., 2016a). If the reflectance is negligible, then the FOM is simplified using Eq. (6) (Liu et al., 2021):

$$FOM = \frac{-1}{R_s \ln T} \tag{6}$$

Where Rs is the CuI film resistance and T is its transmittance in the visible light region. The computed FOM for CuI shows a significantly very high value of $1.3*10^6$ M/Ω relative to other transparent p-type conductors and closer to the standard ITO with $4*10^6$ M/Ω, as shown in Fig. 8b (Liu et al., 2021).

Consequently, the CuI shows the highest p-type conductivity compared to other p-type metal oxides but it still needs more improvements to overcome the n-type transparent conducting oxides. The electrical conductivity of CuI is directly dependent on its carrier mobility (μ), carrier concentration (n), and elementary charge (e) as shown in Eq. (7) (Wan et al., 2010):

$$\sigma = e * n * \mu \tag{7}$$

Based on the industry-standard ITO, the electron mobility of 50 cm^2/V s and concentration of $10^{21}/cm^3$ is attainable at high conductivity reaching 10^4 S/cm. The most recent reported p-type CuI thin films have shown enhanced Hall mobility to 3.5–9 cm^2/V s and hole concentrations of $10^{20}/cm^3$ (Ruan et al., 2021). The n in Eq. (7) is related to the intrinsic facile formation of mobile electric charge carriers either through dopants or defects (Wan et al., 2010). The deposition in chalcogen elements of Se^{2-} or S^{2-} and I-rich conditions have been the most feasible approaches for incrementing the n values (Murmu et al., 2021). The additional holes during the I^- substitution could be easily activated as free holes into VBM considering the energy levels of dopant to be positioned above these VBM, which in return will increase significantly the σ of CuI film (Murmu et al., 2021).

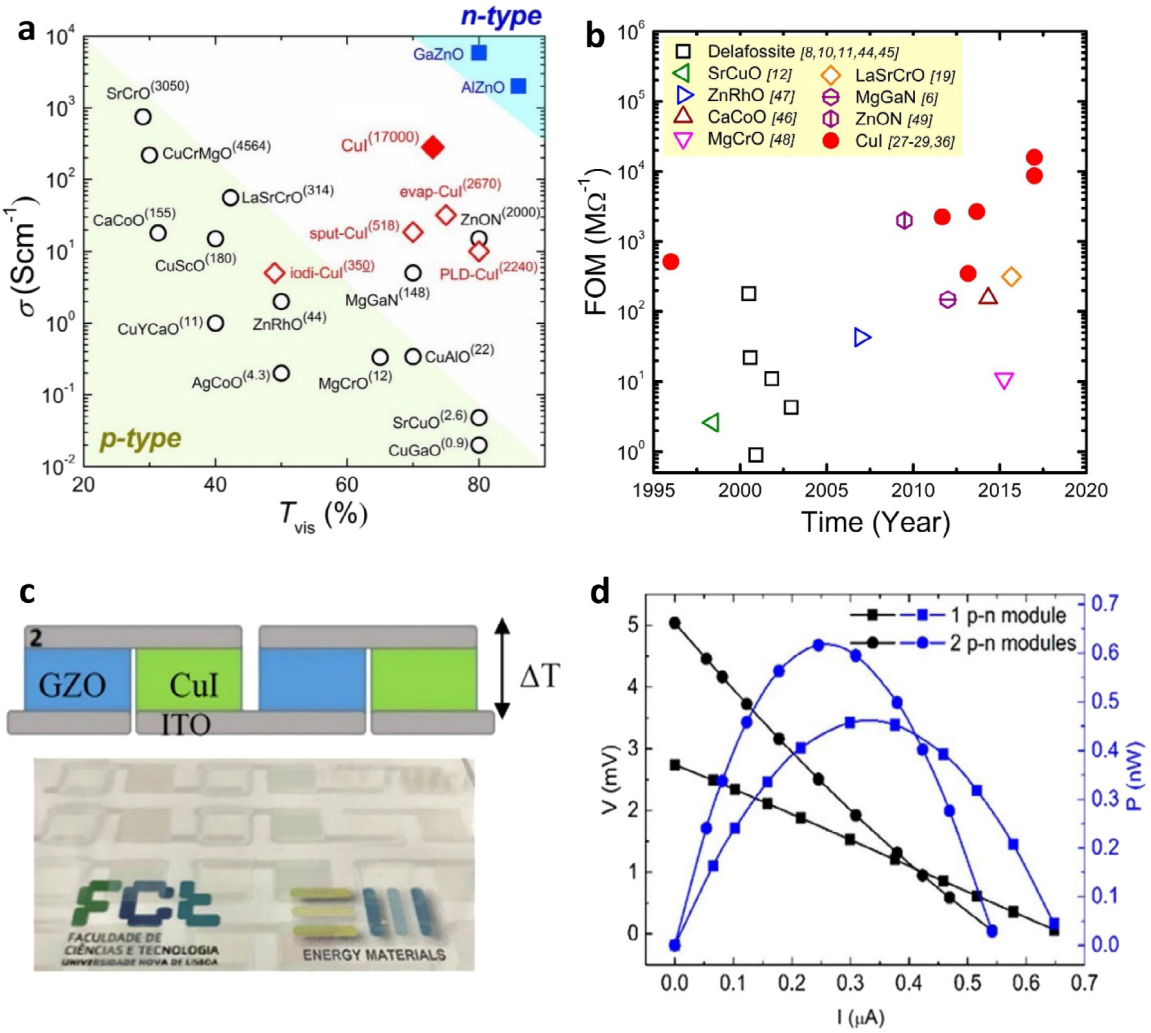

Fig. 8. (a) The Dependence of electrical conductivity at RT on transparency of CuI compared to other n- and p-type transparent TE thin films and (b) the development of dimensional Figure-of-Merit (FOM) for CuI and other p-type transparent thin films (Yang et al., 2016a), with permission of Proc. Natl. Acad. Sci., copyright 2016. (c) The Photograph and (d) TE properties of TE p–n modules based on CuI/GZO deposited on a glass substrate (Faustino et al., 2018), with permission of Springer Nature, copyright 2018.

Whereas, the μ is in inverse proportionality to the carrier effective mass (m^*) but is in direct proportionality to the carrier scattering time (τ), as displayed in Eq. (8) (Li et al., 2017a):

$$\mu = \frac{e*\tau}{m^*} \tag{8}$$

The τ is modifiable via extrinsic factors such as tuning film deposition technique, defects, grain boundaries, and ionized dopants, while the m^* is an intrinsic parameter (Li et al., 2017a). Thus, enhancing μ and τ are feasible through adopting epitaxial growth methods for deposition of CuI films in high quality, as well as enlarging of grain size (Chen, 2016). The highest Hall mobility of 44 cm^2/V s has been reported for CuI in its single crystal form but not in the polycrystalline thin film form, which still needs more improvements (O'Dwyer et al., 2017). On the other hand, the TE material had better exhibit low thermal conductivity, high Seebeck coefficient, and electrical conductivity to undergo high TE performance, as presented in Eq. (9) (Zebarjadi et al., 2012):

$$ZT = \frac{S^2*\sigma}{k}T \tag{9}$$

Where the ZT is the dimensionless Figure-of-Merit, k is the thermal conductivity, S is the Seebeck coefficient, σ is the electrical conductivity, and T is the absolute temperature (Zebarjadi et al., 2012). The challenge is in the difficulty of simultaneous controlling of these parameters due to their interdepends on each other and then improving one leads to the sacrifice of others (Hamid Elsheikh et al., 2014).

Consequently, more efforts are made currently to develop new TE materials based on non-toxic, earth-abundant, and inexpensive elements for large-scale production (Hamid Elsheikh et al., 2014). The CuI has been shown to fulfill these criteria with high TE performance overcoming other transparent TE materials (Liu et al., 2017). This is due to its strong phonon scattering and heavy iodine element resulting in low k and high S of 237 μV/K for the γ-CuI thin films (Kennedy et al., 2020). The TE modules require the coupling of transparent n- and p-type TE materials to build the p–n junctions like other complementary electronics (Brahmbhatt and Agrawal, 2015). To date, there is still a deficiency in highly p-type conductive transparent and flexible TE material (Brahmbhatt and Agrawal, 2015). A preliminary study has grown CuI thin films at 300 nm using the reactive sputtering at RT and it exhibited a high ZT value of 0.21 at 300 K (Liu et al., 2021). This ZT value is higher by 100 times than the n-type transparent conducting oxides (TCOs) and 1000 times than the p-type TCOs. This has led to the fabrication of a TE prototype based on transparent and flexible CuI thin films in ultrahigh power density reaching 2.4 mW/cm^{-2} at ΔT of 50 K. Recently,

Table 2
The thermoelectric properties of transparent and flexible n-type GZO and p-type CuI thin films module (Faustino et al., 2018; Liu et al., 2021).

Material	Thickness [nm]	Hall mobility (μ_H) [cm^2/V s]	Hole concentration (n_p) [$10^{20}/cm^3$]	Electrical conductivity (σ) [S/cm]	Seebeck coefficient (S) [μV/K]	Power factor (PF) [μW/m K^2]	Thermal conductivity (k) [W/m K]
p-type CuI	302	4.1	1.7	3.1	206.0	0.47	0.48
n-type GZO	306	15	5.9	3.1	−60	0.5	2.17

the n-type GZO and p-type CuI thin films have been deposited using solid iodination technique for fabrication of flexible and invisible p–n TE modules, as displayed in Figs. 8c and d (Liu et al., 2021). The TE properties of this p–n TE module are summarized in Table 2 (Faustino et al., 2018; Liu et al., 2021). Its generated output power was comparable to the recognized TE bulk component of Sb_2Te_3/Bi_2Te_3 with a ZT value close to the unity (Kanatzidis, 2010). These reported outcomes have further accelerated the novelty of CuI as the most promising transparent TE material to be implemented in promising applications such as TE windows, miniaturized chips power reversion or on-cooling, and body-heat-driven wearable electronics (Twaha et al., 2016).

3. Thermoelectric CuI thin films synthesis techniques

The fabrication of CuI thin films is essential for TE device flexibility, transparency, efficiency, and miniaturization. The most common and effective approaches to synthesizing low defects and high TE performance for a significant breakthrough in advancements of CuI thin films for portable and wearable applications are based on the following techniques:

3.1. Physical Vapor Deposition (PVD)

The Physical Vapor Deposition (PVD) is based on vacuum coating techniques to deposit atoms of the coating material forming a thin film over the substrate through condensation from the vapor phase to the solid phase (Lv et al., 2015). The method of iodine vapor has been the most popular route since 1907 for deposition of γ-CuI thin films using a Cu reaction with iodine vapor (Lv et al., 2015). The exposure of Cu film to iodine vapor leads to its rapid conversion into CuI, as illustrated in Fig. 9a (Liu et al., 2021). The synthesis of transparent and flexible CuI thin film could take only 20 min through its acceleration at moderate temperatures around 120 °C due to the high volatility of iodine (Chen et al., 2018b). The rate of iodization decreases gradually at high temperatures exceeding 150 °C. The grown CuI thin films exhibited satisfactory p-type semiconducting properties with Hall mobility of 6 cm^2/V s and hole density of $5*10^{18}/cm^3$ (Liu et al., 2021). While it shows a rough surface with a root-mean-square (RMS) roughness above 30 nm due to the fast chemical reaction between iodine and Cu (Liu et al., 2021). Recently, a newly developed solution iodination method at room temperature based on dipping the Cu film into iodine dissolved ethanol solution (Zhang et al., 2019). The resultant thin film of p-type CuI exhibited a high Hall mobility of 34 cm^2/V s, transparency above 70%, and low resistivity around 0.02 Ω cm (Zhang et al., 2019). The solid-iodination method has been further developed to easiness the deposition of γ-CuI via a chemical reaction between the solid-phase iodine and Cu_3N at room temperature, as displayed in Fig. 9b (Liu et al., 2021). The deposited CuI thin films showed high Hall mobilities ranging from 9 to 21 cm^2/V s, an enhanced surface morphology with RMS close to 10 nm, and optical transmittance of 70% at 500 nm (Liu et al., 2021).

The pulsed laser deposition (PLD) technique of CuI films uses the KrF excimer laser to sinter the CuI ceramic target, as presented in Fig. 9c (Liu et al., 2021). The increase of growth temperature for the PLD-grown CuI thin films has reduced ionized impurity scattering leading to a decrease in hole concentration but an increase in the Hall mobility. The modulable values of hole concentrations are observed in a wide range of $5*10^{16}$–$10^{19}/cm^3$ along with the maximum Hall mobility reaching 20 cm^2/V s at the growth temperature of 240 °C. The deposited CuI film surface exhibited a similar rough RMS to the iodization deposition route close to 4 nm. Whereas the lower growth temperatures attained smooth surfaces, then the PLD technique was inadequate for limited large-area mass fabrication, high cost, and low deposition efficiency (Wang et al., 2016). On the other hand, the thermal evaporation technique has shown effective deposition of transparent and flexible CuI thin film with a low RMS value of 2 nm at room temperature (RT), as shown in Fig. 9d (Liu et al., 2021). The elevated annealing temperature resulted in an enlarged grain size (Lal et al., 2019). While the enhanced substrate temperature equivalent to 120 °C resulted in the highest conductivity of 100 S/cm and good Hall mobility of 25 cm^2/V s (Lal et al., 2019).

Moreover, the sputtering techniques of direct current (DC), magnetron sputtering, and nonreactive radio frequency (RF) have shown their feasibility for depositing CuI thin films (Alam and Ramakrishna, 2013). Whereas reactive sputtering own intrinsic advantages compared to the conventional DC and RF sputtering assigned to the uneasiness in sintering a CuI target. The DC sputtering source uses commonly the metallic disk of Cu along with continuous input of iodine vapor, as illustrated in Fig. 9e (Liu et al., 2021). The Cu target owns high conductivity increasing the possibilities of high film uniformity as a result of high plasma density. Such a technique permits the modulation of the Cu/I ratio and then attaining the highest conductivity of CuI at 283 S/cm with I-rich CuI (Liu et al., 2021). The frequently reported kinetics and growth mechanism for the sputtered CuI thin films investigate the interface properties of the adatom/substrate (Graužinyte et al., 2019). These properties are determined by the growth rate and deposition temperature, which play a crucial role in synthesizing smooth CuI surfaces with RMS of 2–3 nm in a uniform structure (Graužinyte et al., 2019). This was achievable at a high growth rate and high substrate temperature of 358 °C. Additionally, thermal evaporation is a promising technique for CuI thin film deposition. This is due to its simplicity, good reproducibility via commercialized CuI powder and growth of smooth and high-quality CuI films over large areas at plastic-compatible temperatures (Kaushik et al., 2017).

3.2. Chemical Vapor Deposition (CVD)

The techniques of chemical vapor deposition are favored for cost-effective manufacturing through solution-based printing and coating routes, which do not rely on costly high-vacuum processing chambers (Zhao et al., 2019b). The additional advantages of the solution process are component adjustment, easy operation, and atmospheric deposition capabilities in large areas (Zhao et al., 2019b). This enables the direct deposition of CuI film on the substrate at relatively low temperatures near room temperature. The resultant CuI film exhibited ultrahigh transparency of 90% in a smooth RMS of 0.6 nm and high mobility around 5.1 cm^2/V s (Saleemi, 2014). This promising synthesis approach

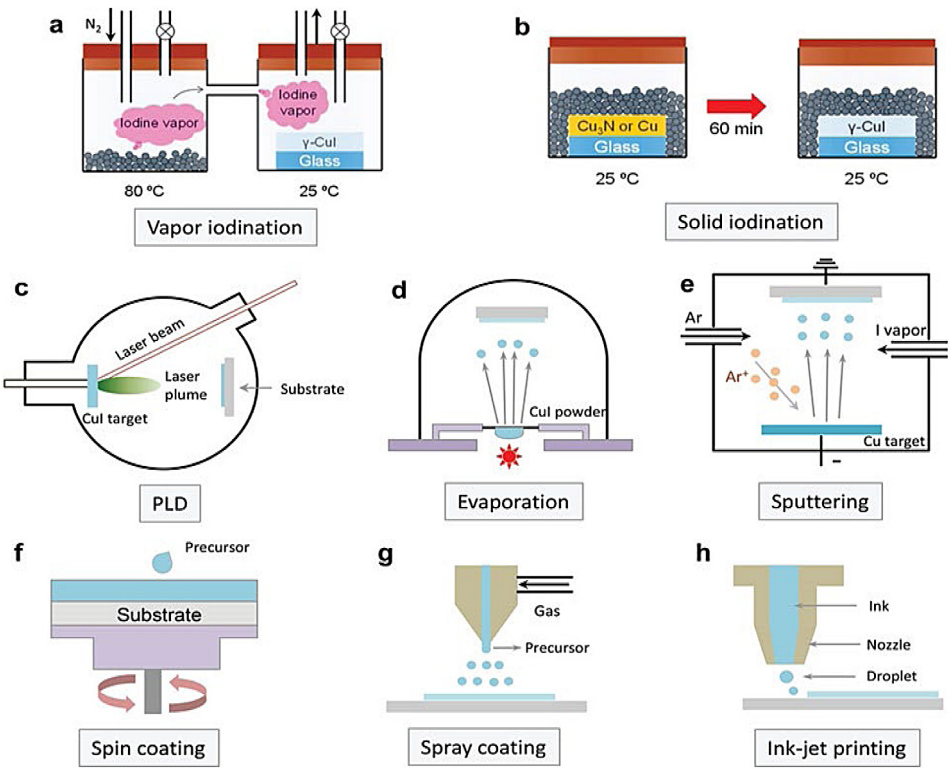

Fig. 9. The Schematics of different CuI thin film deposition techniques using (a) vapor and (b) solid iodination routes (Yamada et al., 2016), ACS Publications, copyright 2016. (c) Pulsed laser deposition (PLD), (d) thermal evaporation, (e) reactive sputtering, (f) spin coating, (g) spray coating, and (h) inkjet printing (Liu et al., 2021), with permission of Wiley Online Library, copyright 2021.

overcomes the metal oxide thin films based on solution processes, which demand ultrahigh annealing temperatures exceeding 300 °C for densification of deposited CuI film and conversion of precursor (Saleemi, 2014). The increase of annealing temperature along with the acceleration of iodine decomposition above 60 °C will lead to dramatic enhancements in the film crystallinity and appearance of the new CuO phase subsequently at 200 °C annealing in the air (Shi et al., 2005).

The spray coating and ink-jet printing are the most scalable CVD techniques for deposition of CuI thin films, as demonstrated in Figs. 9g and h (Liu et al., 2021). While the spin-coating has limitations for large area deposition due to wasting 95% of the solution throughout the film deposition despite its good reproducibility and simplicity, as displayed in Fig. 9f (Liu et al., 2021). The film coating or annealing methods, as well the solvent selection need high considerations to synthesize high-quality CuI thin films using the CVD techniques. The solvent characteristics contribute to defining the dynamics of film-forming and then affect its quality despite the adopted solution-processed method (Snyder and Toberer, 2010). Recently, acetonitrile is used as the most commonly low-toxic solvent for CuI thin film deposition based on solution processing routes (Snyder and Toberer, 2010). However, it resulted in poor film uniformity and crystallinity due to its fast volatility during the coating process owing to its low boiling point. This raises the need to regulate the solvent evaporation rate, as well as consider other characteristics such as its viscosity and solute–solvent coordination interaction (Ortega et al., 2017).

The Cu^{+} tends to have solid coordination complexes with the solvent involving N^{-} and S^{-} ligands due to its soft acid character (Ortega et al., 2017). The antisolvent treatment is used to improve film crystallinity and diminish the solvent residues at low annealing temperatures of CuI thin films. Thus, spin coating and thermal annealing are the most frequently utilized deposition and post-treatment approaches, respectively. The speedy spin throughout the process of CuI film coating results in uncontrollable and fast solvent evaporation causing the fast crystallization and aggregation of the CuI cluster (Inudo et al., 2013). This leads to the development of alternative chemical deposition techniques for growing high-quality thin film of CuI on large areas with great uniformity and smooth surface (Inudo et al., 2013). The blade/bar coating is the most promising approach for effective improvements of film quality and crystallinity for halide perovskite and metal oxide semiconductors (Liang et al., 2018). The CuI has low formation energy causing the photonic processing techniques suitable for reducing post-annealing time and temperature compared to traditional thermal heating (Liang et al., 2018). The accurate interaction between CuI film and photons is attainable through the use of light sources such as a flash laser and deep ultraviolet annealing, which delivers the energy in a short time range of μs to ms (Soni et al., 2012).

On the other hand, the PVD methods such as evaporation, PLD, and sputtering are capable to grown CuI thin films with high conductivity, dense structure, and high film purity, which fulfills the requirements of transparent TE devices, as presented in Table 3 (Ma et al., 2021b; Liu et al., 2021). Whereas industrial mass production favored the deposition of CuI films using evaporation and sputtering techniques. In contrast, the PLD and molecular beam epitaxy are appropriate for only research at a laboratory scale due to their inadequate scale of film growth (Zhang et al., 2021). However, the CuI thin films deposited using CVD solution-based techniques such as spin coating and inkjet printing have shown the presence of impurities and loose film density resulting in exhibiting deficiency in its electrical conductivity (Oh et al., 2017). The prominent benefit of solution-processed is the facile combination of different atoms that is suitable for examining the doping/alloying effect on TE performance of CuI films (O'Dwyer et al., 2017). This doping capacity of γ-CuI films besides its

Table 3
The effect of different deposition techniques on the properties of p-type CuI thin films (Ma et al., 2021b; Liu et al., 2021).

Deposition technique	Growth temperature [°C]	Hall mobility (μ_H) [cm^2/V s]	Hole concentration (n_P) [1/cm^3]	Electrical conductivity (σ) [S/cm]	Transmittance at 500 nm [%]	RMS [nm]
Solid iodination	120–150	9–21	$4*0^{17}$–10^{18}	1	70%	8–12
Solution iodination	RT	34	10^{18}–10^{19}	50	60%	30
Vapor iodination	120	6	10^{18}–10^{19}	5	50%	30–80
PLD	70–240	8–20	$5*10^{16}$–10^{19}	100	80%	1–4
Sputtering	RT	3–9	10^{19}–10^{20}	156–283	>60%	2–3
Evaporation	RT-200	2–25	10^{19}–10^{20}	100	>60%	2–5
Molecular beam epitaxy	240	10	10^{18}	0.01–1	–	–
Spin coating	RT-150	0.5–7	$7*10^{16}$–$5*10^{19}$	0.025–3,5	>70%	0.6–20
Ink-jet printing	60	10.5	$2.2*10^{16}$	–	>80%	3.24

high hole concentration and conductivity makes it the most suitable transparent p-type conductor for TE energy conversion in transparent TE applications (O'Dwyer et al., 2017).

3.3. Post-treatment processes

The as-deposited at room temperature (25 °C) CuI thin films have shown high electrical resistivity of $3.1*10^{-2}$ Ω cm with relatively low Hall mobility (μ_H) and concentration (n_P) of 2.4 cm^2/V s and $8.9*10^{19}$/cm^3, respectively (Yang et al., 2016a). This raises the crucial role of post-treatment processes in particular the annealing for as-deposited CuI thin films to suppress their electrical transport properties and then thermoelectric performance through phase stability and defect removal. The mid-heat treatment of CuI at 100–150 ° C under an inert atmosphere has enhanced the μ_H up to 9–10 cm^2/V s, which overcomes other p-type semiconductors with wide-bandgap deposited in high temperatures exceeding 400 °C (Nandy et al., 2007). It is frequently reported that the solution-processed CuI p-type thin films require high-heat treatment (>250 °C) for impurity decomposition, sufficient conductivity enhancement, and atomic rearrangement for structural stabilization (Kokubun et al., 1971). The spin coating is the most common solution technique for deposition of CuI thin films based on CuI/Acetonitrile solution, as demonstrated in Fig. 10a (Parker and Singh, 2011). The deposited CuI films had undergone heat treatment at different temperatures from RT up to 200 °C. The X-ray diffraction (XRD) analysis of CuI thin films spin-coated showed its diffraction patterns with the highest intensity peak at the diffraction angle of 25.5°, which is recognized as the (111) plane of γ-CuI based on JCPDS card no. 06-0246, as displayed in Fig. 10b (Parker and Singh, 2011).

The XRD patterns confirm that elevating the annealing temperature of the film resulted in dramatic enhancements in its crystallinity. It is noticed the appearance of an additional CuO phase at 200 °C annealing temperature. The film surface has been examined through Atomic Force Microscopy (AFM). The AFM images displayed a strong topography dependence on the annealing temperature, as presented in Fig. 10c (Parker and Singh, 2011). The RMS roughness of CuI film has increased sharply from 0.58 to 5.76 nm at high annealing temperatures from RT to 100 °C. This is referred to as the thermally induced crystalline agglomeration matching the observations in XRD patterns (Yang et al., 2016b). The RMS roughness has decreased to 3.75 nm at an annealing temperature of 200 °C, which is probably caused by incrementations in surface energy. This drives the atoms to sites of lower energy and returns in uniform distribution of surface atoms (Yang et al., 2016b). It is also possible to be caused by the existence of the CuO phase and then filling the area voids between the crystallization peaks of CuI. Additionally, the fabricated CuI films at different annealing temperatures exhibited transmittance spectra in the visible region, as shown in Fig. 10d (Parker and Singh, 2011). The CuI film transmittance has increased at high annealing temperatures above 100 °C, which is a result of the enhanced film crystallinity and then reduction of light scattering.

The bandgap (E_g) of CuI films annealed in temperature ranges from RT to 100 °C has increased from 2.95 to 2.99 eV, as displayed in the inset of Fig. 10d (Parker and Singh, 2011). Then it decreased to 2.92 eV at 200 °C annealing temperature. The incrementation in the E_g is referred to as the gradual lattice perfection and then the annihilation of localized states in the band structure of CuI film (Amalina et al., 2010). Whereas the decline in E_g at 200 °C is assigned to the appearance of the CuO phase with smaller E_g of 2.0 eV, which decreased the overall E_g. The elemental mapping of Cu and I in γ-CuI film as-deposited at RT and annealed at 200 °C has been examined using the Transmission Electron Microscopy (TEM), as presented in Fig. 11a and b, respectively (Murmu et al., 2021). In elemental mapping of Cu, it is evidenced by the formation of distinct Cu-rich regions at an annealing temperature of 200 °C. This is due to the diminution of high mobility I in CuI thin films during the heat treatment and then resulting in Cu-rich regions (Amalina et al., 2010). The high vacuum annealing of the γ-CuI film has declined significantly its vacancy concentration of Cu (V_{Cu}) compared to the as-deposited film, as illustrated in Figs. 11c and d, respectively (Murmu et al., 2021). The annealed CuI films showed also a lower hole concentration than the RT deposited films due to the insignificant formation of oxygen-assisted V_{Cu}.

The annealed CuI thin films own a higher Seebeck coefficient, which is combining the result of the reduction in hole concentration and energy-dependent scattering to charge carriers at grain boundaries between the CuI film and Cu-rich region. This mechanism in energy filtering of charge carriers allowed transportation of only high-energy holes across the potential barrier (V_b). The annealed p-type CuI films filter out the low-energy holes through its V_b, as demonstrated in Fig. 11f (Murmu et al., 2021). It is reported that the Seebeck value of annealed CuI films in an argon atmosphere is higher than the films annealing in a vacuum (Molina-Lopez, 2020). This is referred to as the low V_b values in vacuum annealed CuI thin films even if it has lower hole concentrations (Molina-Lopez, 2020). Additionally, the electrical properties of γ-CuI thin films including its Hall mobility (μ_H), hole concentration (n_P), and electrical conductivity (σ) have been all examined using the Hall-transport measurements at RT, as summarized in Table 4 (Murmu et al., 2021; Kennedy et al., 2020). The Hall coefficients of as-deposited and annealed CuI films exhibited positive values indicating the p-type semiconductor film with holes as its major charge carriers. The annealing of CuI films leads to a significant drop in its σ from 24.1 to 1.25 S/cm for the RT deposited film and 250 ° C annealed film, respectively.

Similarly, the n_P was higher for the as-deposited CuI film with $3.35*10^{19}$/cm^3 and declined by 1 order of magnitude at 250 °C annealed film reaching $5.11*10^{18}$/cm^3. Interestingly, the μ_H has varied slightly between the RT deposited and annealed films

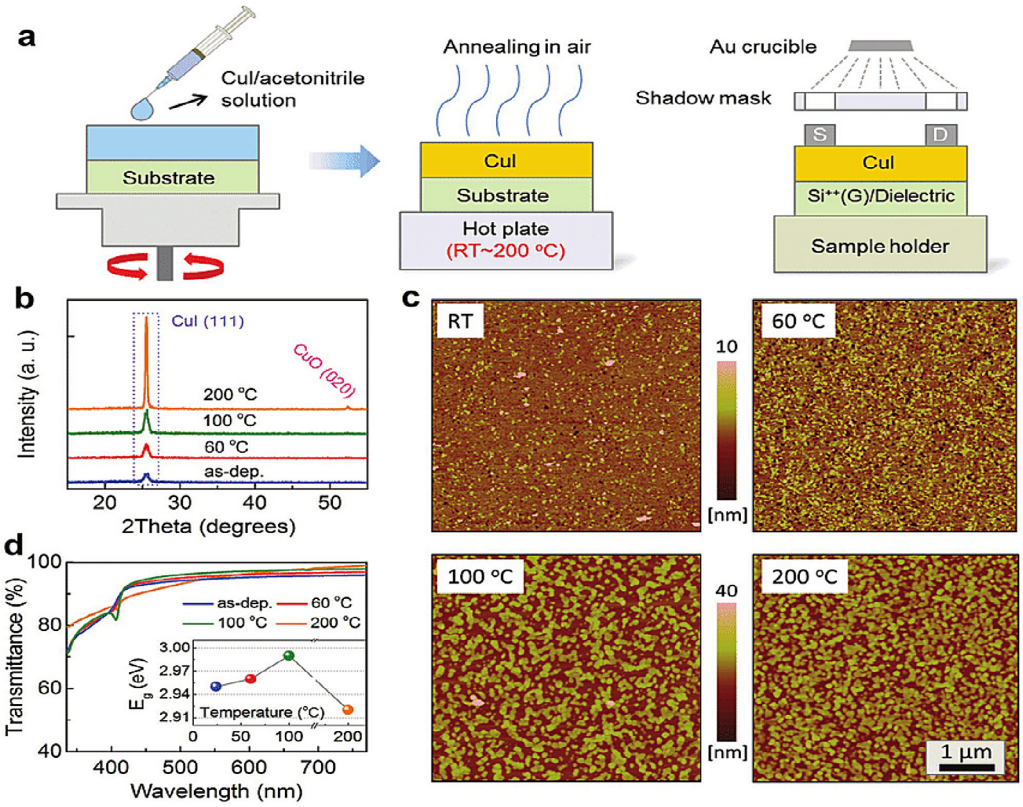

Fig. 10. The CuI thin film synthesis using (a) spin-coating process, and its characterization based on (b) X-ray diffraction patterns, (c) Atomic force microscope images, and (d) Optical transmittances and bandgaps (inset) of annealed CuI thin films at various temperatures of RT, 60, 100, and 200 °C (Liu et al., 2018b), with permission of Wiley Online Library, copyright 2018.

Table 4
The dependence of electrical and thermoelectric properties of p-type CuI thin films on post-treatment annealing temperatures (Murmu et al., 2021; Kennedy et al., 2020).

CuI annealing temperature (T_{anneal}) [°C]	Film thickness [nm]	Hall mobility (μ_H) [cm^2/V s]	Hole concentration (n_P) [$10^{18}/cm^3$]	Electrical conductivity (σ) [S/cm]	Seebeck coefficient (S) [μV/K]	Power factor (PF) [μW/m K]
RT-as deposited	31.9	4.35	33.5	24.1	250.2	145.8
50–60	34.6	4.68	25.8	18.5	397.5	292.5
75–100	20.1	4.91	21.7	16.1	498.3	390.7
125–150	31.8	4.99	13.5	11.2	490.1	302.5
200	–	4.99	5.21	4.56	375.4	165.2
250	–	1.38	5.11	1.25	445.7	25.93

reaching 200 °C in the range of 4.35 to 4.99 cm^2/V s. However, the annealed film at 250 °C showed a significant change in μ_H with an ultralow value of 1.38 cm^2/V s. Additionally, the Seebeck coefficient (S) of as-deposited and annealed films had positive values and further confirms the p-type conductance behavior of CuI films with holes as its major charge carriers (Song et al., 2004). The as-deposited γ-CuI film exhibited an S value of 250.2 μV/K and it has been incremented by 50.2% at the 100 °C annealed film reaching 498.3 μV/K, as presented in Table 4 (Murmu et al., 2021; Kennedy et al., 2020). The S values decreased to 375.4 and 445.7 μV/K at elevated annealing temperatures of 200 and 250 °C, respectively. The 100 °C annealed films owned the highest power factor (PF) of 390.7 μW/m K, which is due to the 50.2% improvement in its S. The annealed CuI films above 100 °C had lower PF reaching 25.93 μW/m K at 250 °C referred to the significant reduction in their σ and S. It is also noticed that the CuI film thickness is turned to be thinner with elevating the annealing temperature from 50 to 100 °C reaching 34.6 and 20.1 nm, respectively.

4. Thermoelectric CuI thin films modules design

The TE modules are designed for direct conversion of the waste heat into electric energy with low operating cost, good reliability, and eco-friendly. Currently, there is a growing interest in developments of micro-electronics leading to the increase in demand for lightweight, high-power-density micro-sized TE devices, and sustainable energy harvesting (Ahiska and Mamur, 2014). The micro-sized TE devices are essential to minimize heat loss and maximize the energy conversion that is difficult to be attained via the conventional rigid and brittle TE devices. The integration of flexible TE modules into micro-systems has significant potential for several practical applications based on self-power source, sensor, or cooler (Jovanovic et al., 2012). This is best achieved through utilizing the advanced thin-film technology in the fabrication of micro-TE devices as it offers free-standing thin-film TE materials favorable for optimum device configurations (Jovanovic et al., 2012). It has facilitated their transformation onto any substrate and then reduced thermal

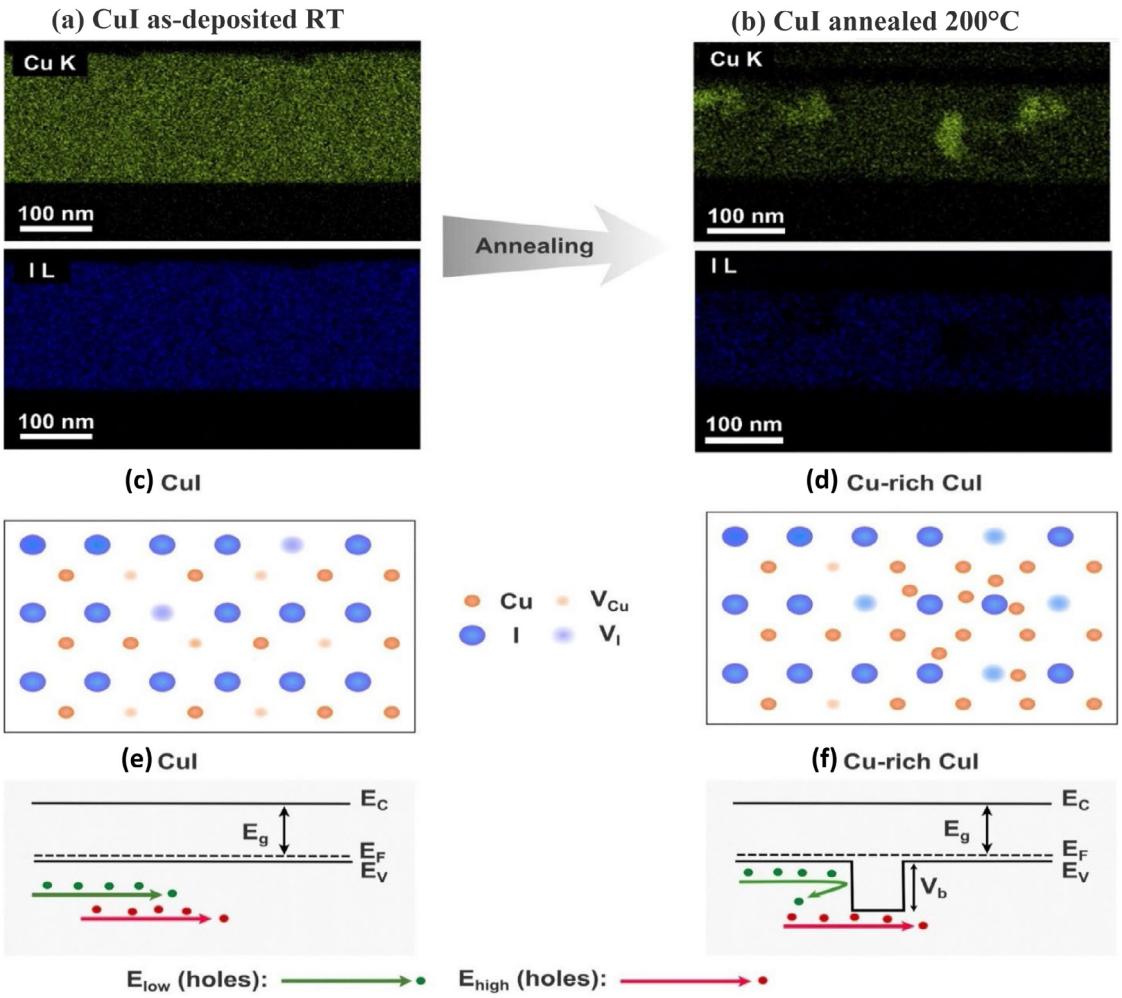

Fig. 11. The Effect of annealing on synthesized CuI thin films characterized using the elemental mapping of I and Cu for (a) as-deposited at RT (25 °C) and (b) annealed at 200 °C. The Schematics of vacancies/atomic distribution and energy filtering mechanism of charge carriers in p-type CuI for (c and e) as-deposited at RT and (d and f) annealed at 200 °C (Murmu et al., 2021), with permission of Springer Nature, copyright 2021.

energy losses for remarkable improvements. The thin-film technology enables also attaining very high ZT values and return in high-efficiency TE devices (Chen et al., 2018a). The thin-film 2D nanomaterials have recorded a high ZT value of 2.4 based on superlattice structure (Chen et al., 2018a). Recently, a thin-film TE generator using organic superlattices has recorded the highest power density of 2.5 W/m^2, which is a hundred times more than the conventional TE generators (Chen et al., 2020b).

However, there are some challenges in the fabrication of thin-film TE modules as poor thermal stability and high preparation cost (Snyder and Toberer, 2010). This limited their use in several practical applications and highlight the need for improvements in their structural design to advance their performance. The basic structures of thin-film devices are the conventional planar-structured modules with a perpendicular heat flux similar to the bulk TE device, as illustrated in Figs. 12a and b (Zhang et al., 2020a). This across-plane device exhibits a convenient connection between TE legs but disables the device to obtain high-temperature differences, which are constrained by thin-film thickness, as shown in Fig. 12c (Chen et al., 2020a). This limits the generated power across TE devices and then many other structures are preferred as in-plane heat transfer structures, as presented in Figs. 12d and e (Zhang et al., 2020a; Chen et al., 2020a). This thin-film structure enables the fabrication of long TE legs and creates a high-temperature gradient across the TE device. The electrical resistance in thin film-based TE devices is built through the plane flow of current. This leads to a new multilayer structure of thin-film TE devices that has a much simpler fabrication process and outstanding performance, as displayed in Fig. 12c (Chen et al., 2020a). In this structure, the electrical current and heat flux flow in parallel to the surface of the thin film.

The thin films in multilayered structure TE device are deposited layer by layer in growth direction across the surface of the thin film in variation to the conventional TE device with in-plane structure. The deposition is in a sequence of thin-film p-type TE layer, an insulating layer, and then an n-type TE layer onto a substrate forming a structure of three layers (Chen et al., 2020a). The use of intentional sheltering enables one end of deposited thin film TE to be in connection with each other forming the p–n junction. This will result in three-layered p–n junctions connected in series along with an insulating layer in between p–n junctions, as demonstrated in Fig. 12f (Chen et al., 2020a). This simple fabrication process enables the thin-film TE device to possess numerous p–n junctions in minor volume size via adjusting the number of thin film layers (Chen et al., 2020a). This multilayered structure enables also the high integration of TE elements and then attaining ultra-high output power through assembling hundreds of p–n TE modules in a minimal range. This breakthrough shows possibilities for simplifications of the manufacturing process and diminishes the need for a large length–width area (Zhang and Zhao, 2015).

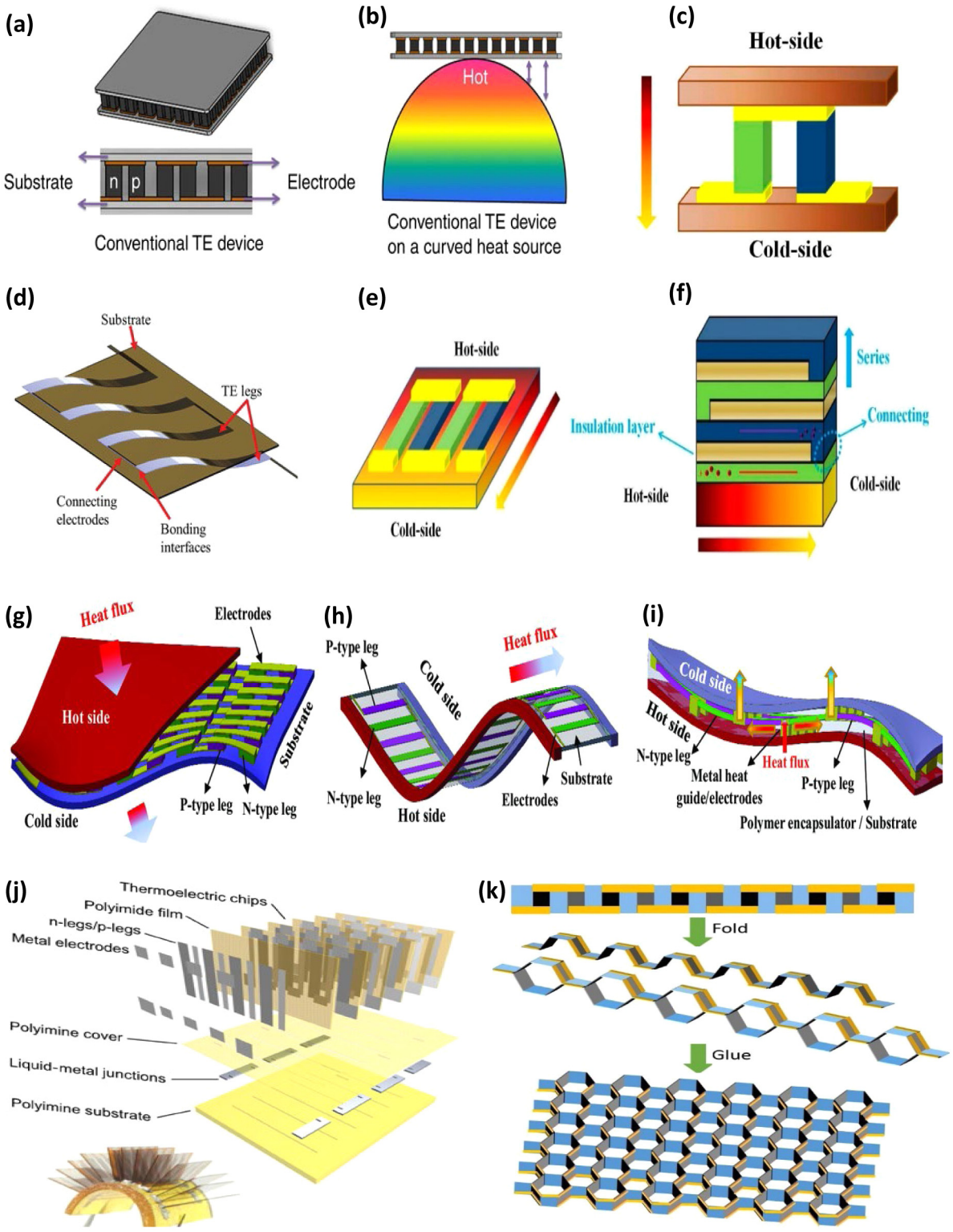

Fig. 12. The Schematics of (a) conventional planar-structured TE device, (b) power generation of conventional TE generator on a curved heat source (Park et al., 2016), with permission of Springer Nature, copyright 2016. (d) Standard module for flexible TE devices (Wang et al., 2019), with permission of Wiley Online Library, copyright 2019. The module designs of thin-film TE device (c) across-plane, (e) in-plane, and (f) multilayer structure (Chen et al., 2020a), with permission of MDPI Publications, copyright 2020. The Configurations of flexible TE devices (g) vertical π-shaped, (h) lateral π-shaped, and (i) Y-shaped (Yang et al., 2021), with permission of Wiley Online Library, copyright 2021. The structural designs of flexible TE devices suitable for human body wear (a) Lego-style design (Ren et al., 2021), with permission of Science Advances, copyright 2021, and (b) honeycomb tension design (Zhao et al., 2019a), with permission of Royal Society of Chemistry, copyright 2019.

The frequently reported configurations of flexible and transparent TE devices are categorized into vertical π-shaped, lateral π-shaped, and Y-shaped TE modules, as illustrated in Figs. 12g, h, and i, respectively (Yang et al., 2021). Each of these TE modules involves three main components, which are the substrate, connecting electrodes, and TE p- and n-type materials. The TE

materials could be made up of inorganic films undergoing large elastic strain or organic materials with good flexibility (Liu et al., 2018b). The substrate of flexible TE modules could be based on flexible fabrics like silk, cloth, Cellulose materials such as paper (Cheng et al., 2018), and polymer fabric or flexible polymer films including polyurethane, poly(dimethylsiloxane), and poly(vinylidene fluoride) (Jouhara et al., 2021). The flexible metals such as Ag and Cu foils, wires, or pastes are used as connecting electrodes in flexible TE devices (Jouhara et al., 2021). They connect the n- and p-type TE materials thermally in parallel but electrically in series. The heat flows in these TE modules from the hot end of the device at the heat source to its cold end at the heat sink. This creates an output voltage that permits the flow of electrons and generates electric power. The TE devices with vertical π-shaped structures have n- and p-type TE legs adhered vertically on top of the flexible substrate or embedded within the substrate, as displayed in Fig. 12g (Yang et al., 2021). The heat flux in this structure is perpendicular to the substrate and then shares a similar configuration to the conventional TE devices with a rigid planar structure.

On the other hand, the flexible TE devices with lateral π-shaped structures have thin TE legs that are laterally adhered to the surface of a flexible substrate. This leads to heat flux in a parallel direction to the substrate, which varies from its flow across TE devices with a vertical π-shaped configuration. Whereas the TE devices with Y-shaped configurations have a combination of vertical and lateral π-shaped configurations. Unlikely, the heat is firstly harvested in a vertical direction from the heat source through metal electrodes to be then transferred across TE legs in a lateral direction. The vertical π-shaped configuration has a more prominent TE performance than the configuration lateral π-shaped due to the parallel flow of heat flux to the substrate instead of its usually perpendicular flow, especially in the TE applications between the surrounding environment and human body (Wang et al., 2020b). Additionally, the vertical configuration could facile adopting short TE legs in TE device to minimize its internal resistance (R_{in}) (Yang et al., 2021). Whereas the Y-shaped and lateral π-shaped configurations have usually longer TE legs and then higher R_{in}. However, these configurations can be based on one type of TE material in case the other type is unavailable to be replaced with a thin metal paste or wire. While the vertical configuration requires both p- and n-type TE materials. These configurations are common in wearable and portable TE devices with high expectations to enrich the user's lives by supporting the unique properties as high mechanical stability, lightweight, high formability, and conformability (Lay-Ekuakille et al., 2009).

Figs. 12j and k show other diversified structural designs suitable for human body wear such as Lego-style design and honeycomb tension structure design (Ren et al., 2021; Zhao et al., 2019a). The Lego-like reconfiguration has shown capabilities in allowing the customization of TE generators for targeted constructions, power, and output voltage considering certain thermal conditions and output of TE chips (Ren et al., 2021). It could be also integrated into a sensor system to produce a self-powered autonomous sensor system (Cheng et al., 2018). Recently, it is reported the first recyclable and self-healable TE generator system based on Lego-like reconfiguration exhibited superior thermoelectric performance and stretchability (Ren et al., 2021). Alternatively, the utilization of honeycomb sandwich structure in TE devices is growing rapidly due to their excellent stiffness to weight and strength to weight characteristics (Peng et al., 2021). The mechanical strength of the honeycomb sandwich structure is based on a combination property of the core, skin, and skin-core interfacial bonding (Peng et al., 2021). The honeycomb-like paper-based TE generator has exhibited stretchability, flexibility, and wear resistance (Peng et al., 2021). Thus, permitting the device to be utilized in a range of complex heat source surfaces. A recent prototype of a honeycomb-like paper-based TE generator applied onto a curved heat source consisting of 96 p–n junctions at ΔT=55 K has shown a maximum output power and an output voltage of 596 nW and 70.5 mV, respectively (Zhao et al., 2019a).

Moreover, the design module of a transparent and flexible thermoelectric generator enables it to be suitable for large-area and limited heat-sink conditions to perform as a power source for window-integrated applications and wireless sensors, as displayed in Fig. 13a (Dong et al., 2018). This module is based on alternating n-type and p-type semiconductors forming thermocouples of p–n junctions. These junctions are connected electrically in series via a conductive electrode and thermally in parallel, as demonstrated in Fig. 13b (Zhu et al., 2013). The TE generators operate in the presence of a temperature gradient (ΔT) between its two bottom and upper ends, as displayed in Fig. 13b. The ΔT will lead to the flow of major charge carriers whether holes in the p-type semiconductor or electrons in the n-type semiconductor. These charges would be at high energy levels at the high-temperature end where the heat is absorbed to derive their movements towards the cold end at which the heat is released. The movements of charges will create a potential difference at the two ends and then result in an output DC voltage. The TE effect could be enhanced via the proper selection of TE module components as discussed in detail in the following sections.

4.1. Substrate materials

The selection of substrate material in the fabrication of TE generators plays a crucial role in its TE performance (Amalina et al., 2013). This is referred to the need for even and uniform distribution of thermal energy among the three main parts of the TE module during its operation namely, p–n thermoelectric couples, conductors, and substrate. The thermal conductivity of the substrate influences its thermal diffusion process based on the Fourier theory, hence affecting the performance of TE devices (Klochko et al., 2019b). The most common in-use substrate materials in the fabrication of thin-film TE converters are Soda-lime glass, Ultra-slim glass (Willow® type), Polyimide (PI, Kapton® type), and Polyethylene Terephthalate (PET), as displayed in Table 5 (Yang et al., 2017a; Schmiedl et al., 2008; Soleimani et al., 2020). The soda-lime glass exhibits the uppermost thermal conductivity (k) of 1.06 W/m K, while the PI Kapton® type records the lowest k of 0.12 W/m K. The increase in k of the substrate leads to a higher maximum ΔT across TE legs, which returns a positive effect on the efficiency of the TE generator and rise dramatically its generated power (Yang et al., 2017a). This improvement in the output power and efficiency is terminated with substrate materials having thermal conductivities exceeding the 22 W/m K at which the ΔT across TE legs is close to ΔT across the whole TE device, which is a fixed value (Yang et al., 2017a). This clarifies the limited influence of substrate materials with high thermal conductivity values on the performance of TE generators.

The transparency of substrate material reflects its ability for allowances of light to pass through it with negligible scattering. This indicates that the substrate has a uniform refractive index opposite to the opaque materials. The tabulated substrates (Table 5) show close transparency in the range of 80%–90% and a refractive index of 1.50–1.70. Considering these optical properties is of high importance to meet the design requirements of transparent and flexible TE devices. It is observed that Young's modulus is highest for glass-based substrates with 75 GPa, whereas polymer-based substrates have not exceeded 3 GPa. This indicates the high elasticity of glass-based substrates in resistance to

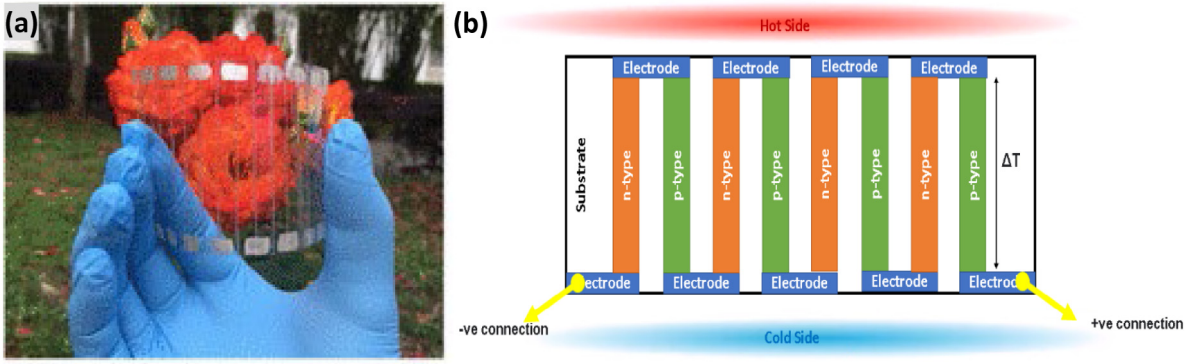

Fig. 13. (a) The Prototype of a typical flexible and transparent thermoelectric generator (Dong et al., 2018), with permission of ACS Publications, copyright 2018. (b) The Typical thin film-based thermoelectric module with alternating p-type (in green) and n-type (in orange) legs connected electrically in series and thermally in parallel forming p–n junctions with top and bottom connecting electrodes (in blue) over substrate material (in white).

Table 5
The physical properties of common flexible and transparent substrates for thin-film thermoelectric generators (Yang et al., 2017a; Schmiedl et al., 2008; Soleimani et al., 2020).

TE substrate material			Soda-Lime Glass	Ultra-Slim Glass (Willow® type)	Polyimide (PI) (Kapton® type)	Polyethylene Terephthalate (PET)
Thermal properties	Thermal conductivity	[W/m K]	1.06	0.96	0.12	0.25
	Softening point	[°C]	720	700	249	250
	Annealing point	[°C]	545	725	400	350
	Thermal expansion coefficient	[ppm/°C]	8	3	20	40
Optical properties	Transparency	[%]	90.0	85.0	86.0	80.0
	Refractive index	–	1.52	1.50	1.70	1.58
Mechanical properties	Young's modulus	[GPa]	72.0	75.0	3.00	2.90
	Density	[g/cm^3]	2.50	2.40	1.42	1.38
Electrical properties	Electrical resistivity	[Ω cm]	7.94*10^9	–	4.00*10^{19}	–

deformation. Thus, high modulus leads to a more rigid and less flexible substrate, hence it is less favorable for flexible TE devices. In addition, the substrates' electrical properties are favorable to be close to insulators with high electrical resistivities to guarantee the development of suitable carrier paths in the thin film circuit. The polymer-based substrates show the highest electrical resistivities reaching 4.0*10^{19} Ω cm in PI Kapton® type.

The temperature of the substrate softening point is at which the material begins to deform or even melt. This leads to the initiation of noticeable changes in its physical properties, which should be considered in the thin-film synthesis processes of TE devices. The temperature of the annealing point needs also to be considered in particular that many fabrication processes of thin films include high-temperature annealing to enhance its TE properties. Thus, it is required to ensure the selection of substrate material with high resistance to deformation in high-temperature environments and having ultrahigh softening and annealing temperatures. The PI polymer shows fulfilling of such requirements as having high thermal stability, excellent flexibility, low cost, and high insulation performance. It has been used as a flexible and stable film for the deposition of $Bi_{0.5}Sb_{1.5}Te_3$ thin films in 0.05 mm thickness via the magnetron sputtering technique (Hu et al., 2021b). This flexible TE thin-film recorded a high power factor (PF) of 23.2mW/cm K^2 near room temperature, which exceeds its bulk counterparts (Hu et al., 2021b). The fabricated thin films have shown a softening temperature of 385 °C, Young's modulus of 3 GPa, k of 0.12 W/m K, and a Shear modulus of 2.7 GPa (Hu et al., 2021b).

The PET substrate shows a competitive performance as characterized by shiny polyester film, transparent, colorless, long-lasting temperature reaching 120 °C, low cost, and lightweight. It has also outstanding electrical insulation and low thermal conductivities reaching 0.25 W/m K (Hou et al., 2018). Its Shear modulus and Young's modulus have recorded 2.2 GPa and 2.9 GPa, respectively (Tappura et al., 2020). However, it is still difficult to fabricate thin-film TE devices on it. It is reported that thin CuI films of 0.1-0.82 μm in thickness have been deposited over the flexible PET substrate via the Successive Ionic Layer Adsorption and Reaction (SILAR) method (Chen et al., 2021c). This single p-type CuI thin film TE material demonstrated an output power of 17.1 μW/m^2 at ΔT equivalent to 35 K (Chen et al., 2021c). It is also reported that the thin film deposition of n-type Bi_2Te_3-In_2Te_3-Ga_2Te_3 over the PET substrate resulted in a film with high thermal conductivities reaching 1.8 W/m K at room temperature of 298.15 K and then a drop in its ZT values to 0.3 at the same temperature (Lee et al., 2020b). Thus, the selection of the suitable substrate material should be taken into consideration for the simple, efficient, low-cost, and integrable synthesis capabilities of TE generators.

4.2. P-type materials

A p-type thermoelectric material is characterized by a high concentration of positively charged carriers namely holes compared to negatively charged carriers as electrons (Lemine et al., 2022). The selection of appropriate p-type semiconducting material is of high importance in identifying the proper fabrication technique and optimum design of flexible and transparent TE devices. The p-type material should own excellent abilities for high energy conversion to attain high efficiency and mechanical property for reliability in long-term applications. Besides that, it should be eco-friendly, flexible, low-cost chemical components,

easy to fabricate, and stable in performance (Uhl et al., 2015). Currently, the flexible TE devices and materials are classified based on the morphology of p- and n-type TE materials involving flexible TE textiles, flexible TE fibers, and flexible TE films (Uhl et al., 2015). The flexible TE films show outstanding performance in TE energy conversion for many novel applications (Yang et al., 2017b). The two-dimensional structure of thin films has improved simultaneously their thermal and electrical properties. There are few p-type materials such as $CuAlO_2$ and CuI with high-band gaps utilized in the preparation of conductive and transparent thin films (Lan et al., 2007). The p-type CuI thin films have much attention as it has shown a significant breakthrough in advancing portable and wearable applications working in the room temperature range. The p-type CuI thin films have recorded a low thermal conductivity, while high Seebeck coefficient and hole conductivity values (Lan et al., 2007).

Lately, the CuI polycrystalline thin films were synthesized at room temperature via reactive sputtering over the transparent glass substrate (Yamada et al., 2017). The copper target has been used in high purity to be sputtered, while iodine vapor has been injected from the gasified iodine source via a needle valve. The hole conduction of synthesized I-doped CuI and undoped p-type CuI thin film is 283 S/cm and 156 S/cm, respectively (Yamada et al., 2017). These CuI thin films recorded a good ZT of 0.21 at 300 K in thickness of 200–300 nm (Yamada et al., 2017). It has been assembled as flexible and transparent TE modules, which opens a new path for next-generation flexible and miniaturized TE devices (Han et al., 2017). On the other hand, the p-type thin films of Copper Aluminum Oxide ($CuAlO_2$) have transparency in the visible region but with lower electrical conductivities. It is reported that the synthesis of good quality and crystallinity p-$CuAlO_2$ films is very difficult for large-scale production (Han et al., 2017). The p-$CuAlO_2$ thin films grown via the RF magnetron sputtering technique on a glass substrate have shown a poor electrical conductivity of 0.32 S/cm and transparency of 75% in the visible region, as displayed in Table 6 (Banerjee et al., 2005). It has shown fairly low charge mobility of 4.07 cm^2/V s and a positive Hall coefficient of +184 cm^3/C in changing the preferential orientation growth of thin films from (015) to (001) direction (Ma et al., 2021a).

However, the p-CuI thin films exhibit a prominent TE performance overcoming the p-$CuAlO_2$, as noticed in Table 6. It has outstanding electrical and transport properties in terms of conductivities, Hall mobility, and hole concentration reaching ultimate values of 283 S/cm, 60 cm^2/V s, and $1.7*10^{20}/cm^3$, respectively. It exhibits optical properties satisfying the design requirement of transparent p-type semiconductors with high transmission up to 90% in a wide wavelength range of 550–1000 nm and an optical band gap around 60 meV. This simultaneous high transparency and conductivity boost its TE properties to attain the lowest thermal conductivities not exceeding 0.55 W/m K and a high Seebeck coefficient up to 562 μV/K. This caused an ultrahigh power factor reaching 471 $\mu W/m\ K^2$ and then the highest ZT value close to 0.29 at room temperature relative to other p-type transparent conductors. Besides that, its moderate values of Young's Modulus ranging in between 37–74G̃Pa and low hardness values of around 1.3 GPa make it appropriate for transparent and flexible electrodes in TE energy conversion applications. To date, the polycrystalline γ-CuI thin films are the highest efficiency TE material that is concurrently transparent and conductive (Chen et al., 2006; Yoon et al., 2017). Thus, it has been of current interest with fulfilling capabilities in planar TE thin films.

4.3. N-type materials

For n-type thermoelectric material, the negatively charged carriers as electrons exist in a high concentration compared to positively charged carriers namely holes (Lemine et al., 2022). The n-type TE material is required to show an equivalent TE performance in conjugate to the p-type material forming the efficient p–n junction modules with ultrahigh energy conversion efficiencies. The transparent metal-based conducting oxides (TCO) are recognized for their widespread in transparent electronic applications, particularly as transparent electrodes in TE junctions and solar cells (Viet Vu et al., 2019). The majority of TCOs currently in the market are transparent n-type semiconductor thin-film with wide-bandgap including CdO, SnO_2, and ZnO (Fan et al., 2015). The Zinc Oxide (ZnO) exhibits stable n-type conduction with good thermal and chemical stabilities, cost-effective, environmentally friendly, and small electronic contribution to its thermal conductivity (Fan et al., 2015). It has small concentrations of charge carriers leading to their moderate electrical conductivity as other TCOs (Fan et al., 2015). This has been overcome by combining it with suitable elements and the selection of appropriate structures via the doping process (Viet Vu et al., 2019). Further advancements in its TE performance have been attained via strengthening the quantum confinement effect to minimize its thermal conductivity (Gayner and Kar, 2016). This approach is to the dimensions of the characteristic wavelength of phonons or electrons ling in the nanometer range (Gayner and Kar, 2016).

Accordingly, the ZnO in thin film form is drawing attention towards more transparent, flexible, lightweight, and integrated TE applications (Ong et al., 2011). The ZnO thin films are doped using different growth techniques based on chemically or physically vacuum processes such as pulse laser deposition, sputtering, and atomic layer deposition (Khors et al., 2011). The chemical processes using solution derived via sol–gel reaction are more simple and lower cost (Viet Vu et al., 2019). It has proven efficiencies in introducing electron donors to ZnO films through doping with Aluminum (Al), Tin (Sn), and Gallium (Ga) (Viet Vu et al., 2019; Khors et al., 2011). This doping is implemented to increase the carrier concentration resulting in incrementing the electrical conductivity of ZnO films. The electrons are the main carriers for electrical transport in n-type ZnO films but contribute to the thermal transport across the film. Thus, the doping concentration of Al, Sn, and Ga should be restricted to 1, 2, and 3 mol% to increase the electron concentration of ZnO films without attaining an incrementation in their thermal conductivity (Klochko et al., 2019a). This will result in an enhancement in TE performance of Al-doped, Sn-doped, and Ga-doped ZnO thin films noted with AZO, SZO, and GZO, respectively. The TE properties associated with transparent oxides of GZO thin films generate outstanding n-type conductivity compared to other doped ZnO-based films, as shown in Fig. 14 (Viet Vu et al., 2019).

The 3 mol% Ga doped ZnO demonstrated the dominant enhanced electrical transport behavior in a temperature range from room temperature to 400 °C, as displayed in Fig. 14 (Viet Vu et al., 2019). This behavior shows the increase in its electrical conductivity over the temperature range with a reverse trend in the Seebeck coefficient of −52 μV/K to −92 μV/K. This reverse trend is characteristic of the TE effect and is referred to as the electron-scattering mechanism occurring at higher temperatures (Liu et al., 2015). This is in parallel to the incrementation of phonons scattering leading to reductions in charge mobility across GZO film. The negative values of the Seebeck coefficient further confirm the n-type semiconducting behavior of GZO films. The high carrier concentration in GZO films leads to a lower Seebeck coefficient and high electrical conductivity compared to other doped ZnO films (Liu et al., 2015). This is due to the

Table 6
The thermoelectric properties of common flexible and transparent p-type materials for thin-film thermoelectric devices measured at room temperature.

P-type thermoelectric material		Copper Iodide (CuI)	Copper Aluminum Oxide ($CuAlO_2$)	Reference
Operating temperature	[K]	300 to 550	300 to 960	Han et al. (2017), Shy and Tseng (2005)
Electrical conductivity (σ_{RT})	[S/cm]	156–283	0.09–0.39	Kennedy et al. (2020), Shy and Tseng (2005)
Hall coefficient (R_H)	[cm^3/C]	0.2–0.7	4.6–22.5	Kennedy et al. (2020), Shy and Tseng (2005)
Hall mobility (μ_H)	[cm^2/V s]	10–60	0.10–4.07	Kennedy et al. (2020), Shy and Tseng (2005)
Hole concentration (n_P)	[1/cm^3]	$5.8*10^{19}$–$1.7*10^{20}$	$2.8*10^{17}$–$1.2*10^{18}$	Kennedy et al. (2020), Shy and Tseng (2005)
Optical bandgap (E_g)	[eV]	3.01–3.11	1.60–3.75	Park et al. (2005), Lin et al. (2016)
Activation energy (E_a)	[meV]	58–62	196–270	Park et al. (2005), Lin et al. (2016)
Thermal conductivity (k)	[W/m K]	0.48–0.55	3.5–1.5	Kaushik et al. (2017), Ichi Yanagiya et al. (2010)
Seebeck coefficient (S)	[μV/K]	160–562	230–120	Kaushik et al. (2017), Ichi Yanagiya et al. (2010)
Power factor (PF)	[μW/m K^2]	443–471	45–72	Faustino et al. (2018), Banerjee et al. (2005)
Figures-of-Merit (ZT)	–	0.21–0.29	0.001–0.017	Faustino et al. (2018), Banerjee et al. (2005)
Transparency (T)	[%]	75–90	60–75	Park et al. (2005), Fares et al. (2018)
Wavelength range (λ)	[nm]	550–1000	300–800	Park et al. (2005), Fares et al. (2018)
Young's modulus (E)	[GPa]	36.6–74.0	97.1–111.5	Chen et al. (2006), Yoon et al. (2017)
Hardness	[GPa]	1.0–1.6	6.50–6.91	Chen et al. (2006), Yoon et al. (2017)

movement of electrons that will transport the heat from the hot end to the cold end building a temperature difference between ends, hence reducing TE voltages. This proven improved electrical transport characterizations of GZO films compared to pristine ZnO films has been frequently reported (Ashida et al., 2009). The GZO films are considered the best doped ZnO film to date due to their significant enhancements in electrical conductivities from 100–124 S/cm (Coroa et al., 2019). This outstanding efficiency of Ga dopant is owing to its minimal lattice deformations, less reactive, high oxidation resistance, and less affected by diffusion issues. Consequently, it has the acceptable electrical behavior for transparent and flexible TE p–n junctions.

4.4. Connecting electrodes

The selection of optimal connecting electrodes is necessary to make outstanding electrical contact of p–n junctions for high-performance and reliable thermoelectric applications. To date, attention is drawn towards developing the next generation of transparent and flexible electrodes for implementation in numerous flexible TE energy conversion modules. These electrodes should exhibit physical and chemical stability, transparency in the visible light range, flexibility, high electrical conductance, and appropriate work function for high-performance flexible and transparent TE devices (Seki et al., 2019). The optical reflection, absorption, and transmission properties are the distinctive features of excellent transparent conducting electrodes (Seki et al., 2019). For instance, Indium Tin Oxide (ITO) films, Graphene, Carbon Single-Walled Nanotubes (SWNTs), poly- (3,4-ethylene dioxythiophene): poly(styrene sulfonic acid) films (PEDOT: PSS), Ag nanogrid, Ag nanowire, and oxide/Ag/oxide films (Dong et al., 2018). These electrodes show a sheet resistance evolution on film thickness with graphene films having the lowest resistivities of $5*10^{-6}$ Ω/sq followed by Ag nanogrid with $5*10^{-5}$ Ω/sq, as displayed in Fig. 15 (Kim et al., 2016a). The Ag nanowire and PEDOT: PSS film show the highest sheet resistivities. Whereas the ITO film exhibits slightly higher sheet resistance of $2–5*10^{-4}$ Ω/sq, which is considered as the lower range achievable by the higher film thickness.

Thus, the outstanding ITO film is commonly used in optoelectronic devices with a thickness exceeding 100 nm and sheet resistance of around 10^{-4} Ω/sq (Lemine et al., 2018). The flexibility of these conventional electrodes is inspected through the material malleability or ductility and their transparency is attainable in nano or microstructures (Lemine et al., 2018). The honeycomb structure increases the flexibility of connecting electrodes and preserves its strength (Aouaj et al., 2009). However, only a few transparent and flexible electrodes own the capabilities to well satisfy all of the pre-mentioned requirements. The ITO is the most promising flexible and transparent electrode that has been broadly adopted in several TE devices (Aouaj et al., 2009). This is referred to its low electrical resistivity ($<1*10^{-3}$ Ω cm), high electron concentration and mobility (10^{21}/cm^3 and 50 cm^2/V s), suitable work function for hole injection (4.4–4.5 eV), outstanding optical transparency (>90% at 550 nm), high physical and chemical durability (Seki et al., 2019). Nevertheless, the conventional ITO electrodes do not well fit the flexible and transparent TE devices. This is due to their rigidity arising from the ionic bonds in ITO electrodes and then leading to the easy formation and propagation of cracks (Chen et al., 2011). These cracks will cause the electrical failure of flexible TE devices (Chen et al., 2011).

Thus, numerous outstanding ITO-based transparent and flexible electrodes have been advanced to avoid the cracking of ITO (Zhang et al., 2011). For instance, ITO nanoparticles, ITO/CuS nanocomposite film, ITO nanowires, Ag nanowire embedded in ITO film, and ITO grew via a continuous roll-to-roll sputtering process (Liu et al., 2015). Recently, highly transparent and bendable ITO electrodes have been processed with simple mesh structures, as demonstrated in Fig. 16 (Sakamoto et al., 2018).

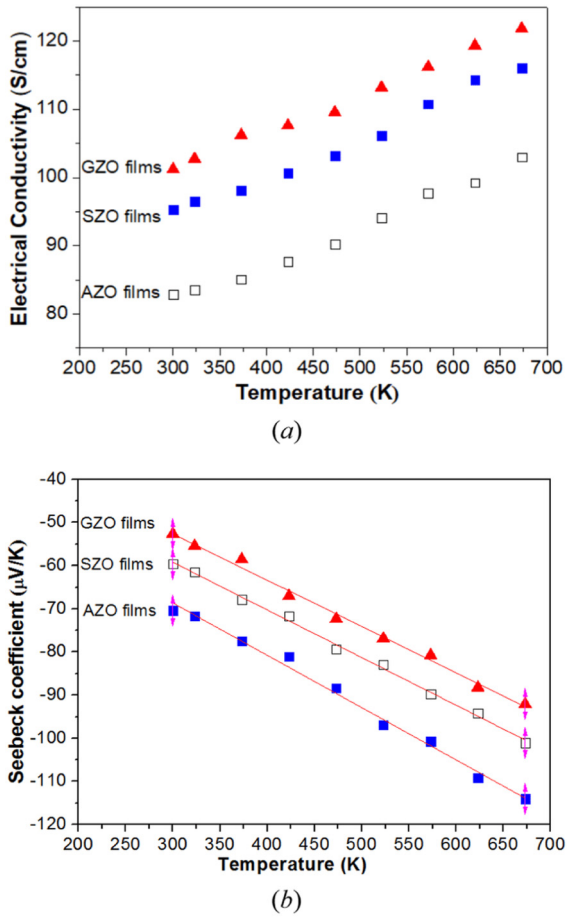

Fig. 14. The Dependence of (a) electrical conductivity and (b) Seebeck coefficient on temperature for n-type flexible and transparent thermoelectric ZnO thin films doped with Al, Sn, and Ga (Viet Vu et al., 2019), with permission of Springer Nature, copyright 2019.

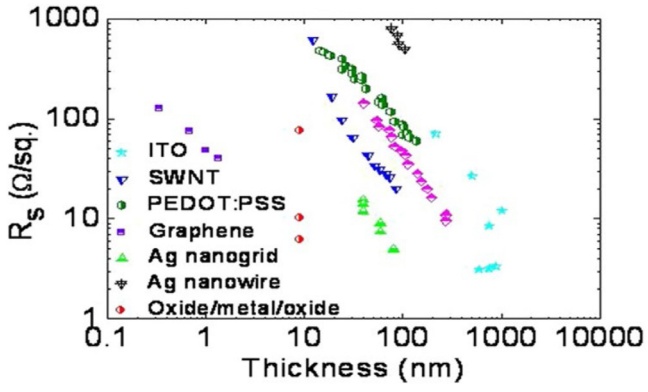

Fig. 15. The Dependence of Sheet resistance (R_s) on film thickness for several transparent conducting electrode films as ITO films, SWNTs, PEDOT: PSS, Ag nanogrid, graphene, oxide/metal/oxide films, and Ag nanowire (Kim et al., 2016a), with permission of Springer Nature, copyright 2016.

These highly flexible ITO electrodes with mesh patterns are synthesized through photolithography and wet etching processes, respectively (Sakamoto et al., 2018). The mesh pattern ensures the prevention of ITO electrodes from cracking under suppressing tensile stress. It also terminates the propagation of cracks if occurred and then maintains its efficient performance in electrical conductivity between the p–n TE legs. Thus, the mesh-patterned ITO electrodes possess an attractive potential for use in transparent and flexible TE devices with reasonable energy conversion efficiencies (Sakamoto et al., 2018).

5. Thermoelectric CuI thin films promising applications

Thermoelectric devices exhibiting flexibility and optical transparency hold unique promise for upcoming electronics in cooling (Hubbard et al., 2020), power generation (Chandel et al., 2022), and personal thermal management (Liu et al., 2020a). The lack of p-type transparent thermoelectric materials hinders the development of invisible thermoelectric elements (Vora-ud et al., 2022). The p-type transparent CuI thin films with superior room-temperature TE performance open the path for multifunctional technologies combining thermoelectricity, flexible electronics, and transparent electronics (K. Almasoudi et al., 2022). The p-type CuI thin films have exhibited diminishing in their thermal conductivity due to the combined effect of heavy element iodine and strong phonon scattering (Zeng et al., 2022). Recently, it is reported that the p-type CuI films have achieved three times enhancements in the magnitude of ZT=0.22 at 300 K compared to other p-type transparent materials. (Faustino et al., 2018). The invisible thermoelectric modules could be fabricated by connecting alternatively the transparent p- and n-type thermoelectric materials. The flexible and invisible thermoelectric module could be utilized in designing novel on-chip power recovery or cooling for miniaturized chips (Kim et al., 2022), body heat-powered wearable devices (Kim et al., 2014b), and thermoelectric windows (D. Bari et al., 2016). The pre-discussed synthesis techniques could be upscaled to produce a large area of transparent CuI thin films on transparent, flexible, and low-cost substrates. Accordingly, the transparent and flexible TE p–n modules based on p-type polycrystalline γ-CuI thin films have shown attractive TE properties for further utilization in a set of promising applications as follows:

5.1. Wearable biosensing

The temperature difference (ΔT) between the ambient air and the human body can reach 80 °C as the ambient temperature usually varies in the range of −40 to 40 °C in different regions and seasons (Kumar et al., 2019). The human body could be considered a permanent source of heat that maintains its temperature to be close to 36.5 °C. Thus, the heat and motion of the human body release a considerable amount of thermal energy that could be recovered into electrical energy with wearable TE generators (TEG) based on CuI thin films (Kumar et al., 2019). The maximum possible efficiency in harvesting the human body heat is based on Carnot efficiency using Eq. (10) considering the relatively low room temperature (20 °C) and normal body temperature (36.5 °C) (Wang et al., 2020b):

$$\eta_{\text{Carnot}} = \frac{T_{\text{body}} - T_{\text{ambient}}}{T_{\text{body}}} = \frac{(310 - 293)\,\text{K}}{310\,\text{K}} = 5.5\% \qquad (10)$$

While the Carnot efficiency decreases to 3.2% in hot ambient temperature (27 °C), which offers the optimum values for energy conversion based on body heat (Wang et al., 2020b). The efficiency of standard wearable TEG for ΔT of 5–20 °C is expected to be only 0.2–0.8%, which is very low compared to the Carnot efficiency (Bahk et al., 2015). It is reported that the total dissipated heat from the human body could be converted into 60–180 W based on the activity (Bahk et al., 2015). This approach is not practical as the generation of such power demands the covering of the whole body with TEGs. Thus, covering a certain part of the body is more practical for high energy recovery potential with thin-film-based TEG to minimize the load power and maximize

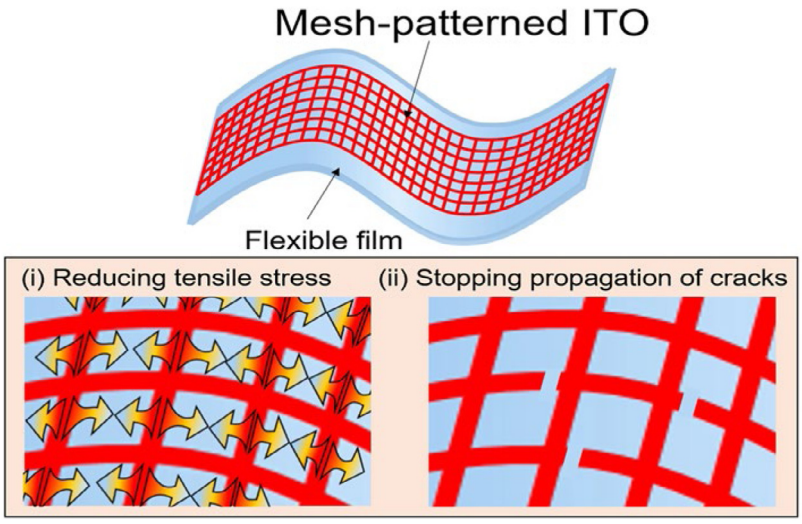

Fig. 16. The Transparent and bendable ITO electrodes in mesh-pattern on flexible film for improving electrode flexibly through reducing the tensile stress and terminating the cracks propagation (Sakamoto et al., 2018), with permission of Springer Nature, copyright 2018.

energy conversion efficiency for such wearable systems (Wang et al., 2020b).

Additionally, heat exchange between the environment and the human body occurs in 3 main heat transfer mechanisms namely radiation, convection, and conduction (Jin et al., 2021). The heat transfer via conduction happens on the direct contact between the substances and bodies. While the heat transfer from the body to the surrounding air is convection and occurs through a transfer medium like blood, gases, or another fluid. The major heat exchange between the body and surroundings is in radiation form (Jin et al., 2021). Thus, the wearable TEG designed to harvest human body heat are utilizing the dissipated heat from the skin and conducted heat to the surrounding matters (Kumar et al., 2019). The placing of TEG on the body with the presence of extrinsic ΔT between the ambiance and body core resulted in steady-state heat flow through the TEG. This intrinsic ΔT across TEG returned in generated voltage (ΔV) through the TE Seebeck effect (Lay-Ekuakille et al., 2009). The maximization of ΔT is crucial for maximizing the heat harvesting across wearable TEG (Lay-Ekuakille et al., 2009). This is a major obstacle caused by the dependent thermal resistances. A typical thermal circuit for wearable TEG attached to human skin is demonstrated in Fig. 17a (Jia et al., 2021). The core temperature of the human body (T_{core}) is 37 °C and the ambient air temperature (T_{air}) is 22 °C forming a normal TEG in between the boundary layer of air (T_{BL}) and T_{skin}. The TEG attached directly to the skin isolates it from the surrounding air and works as its thermal load (Jia et al., 2021).

Thus, the heat flow (W) and temperature drop across TEG (ΔT_{TEG}) are calculated using Eqs. (11) and (12), respectively (Jia et al., 2021):

$$W = \frac{T_{core} - T_{air}}{R_{body} + R_{air} + R_{TEG}} \tag{11}$$

$$\Delta T_{TEG} = T_{skin} - T_{BL} = \frac{R_{TEG}}{R_{body} + R_{air} + R_{TEG}} * (T_{core} - T_{air}) \tag{12}$$

Where R_{body} is the body thermal resistance with the attached TEG, while R_{air} is the sink thermal resistance caused by the radiation and convention on the external side of TEGs. The total thermal resistance of a thermal circuit is dependent on the high thermal resistance of ambient air and the human body. Thus, ΔT_{TEG} is strongly less than the calculated ΔT between the body with the surrounding air. The three main resistances influencing the efficiency of wearable TEG are illustrated in Fig. 17b (Jia et al., 2021). The main sources of thermal resistance are R_{air} and R_{body}, which could contribute to limiting the performance of wearable TEG as follows (Wang et al., 2020b):

1. The thermal insulation of the human body results in resistance between the body core and TEG.
2. The formed contact resistance between TEG and the skin interface is referred to as skin roughness.
3. The air convection influences the thermal resistance at ambiance and the TEG interface.

Consequently, a typical heat sink is employed to enhance energy conversion efficiency by enlarging the existing surface area. It is critical to diminish the above three resistances, as well as select appropriate design parameters for TEG to harvest efficiently the body heat (Guk et al., 2019). The optimal thermal resistance for wearable TEG is estimated using Eq. (13) as follows (Wang et al., 2020b):

$$R_{TEG,\ optimal} = \frac{R_{par,0}\left(R_{body} + R_{air}\right)}{2\left(R_{body} + R_{air}\right) + R_{par,0}} \tag{13}$$

Where the $R_{par,0}$ is the parallel parasitic thermal resistance in a TEG due to the imaginary removal of TE material (Lay-Ekuakille et al., 2009). The thermal energy generated from human skin is caused by its metabolic activity and then it varies from one part of the body to another, as displayed in Fig. 17c (Jia et al., 2021). The forehead has recorded the highest temperatures and gradually decreases downward the body, hence feet record the lowermost temperature. Thus, it is important to consider the skin temperature in selecting the ideal locations for optimum energy harvesting. The output power dependence on the original ΔT formed in between the room and human body temperatures. Accordingly, the different power magnitudes are derivable from different parts of the human body. The harvested power from human skin can reach up to 5 mW after 8 h in an interior environment through clipping silicon thermopiles to the external surfaces of a person's clothes (Lay-Ekuakille et al., 2009). The TEG shows lower power generation if worn on the chest or wrists than when it is worn in a higher place of the arm (Lay-Ekuakille et al., 2009).

The output power is even lower if the TEG is suspended on the T-shirt of a person, as presented in Fig. 17d-I (Jia et al., 2021). The upper arm produces higher output power in particular when the person moves during walking. However, the different locations

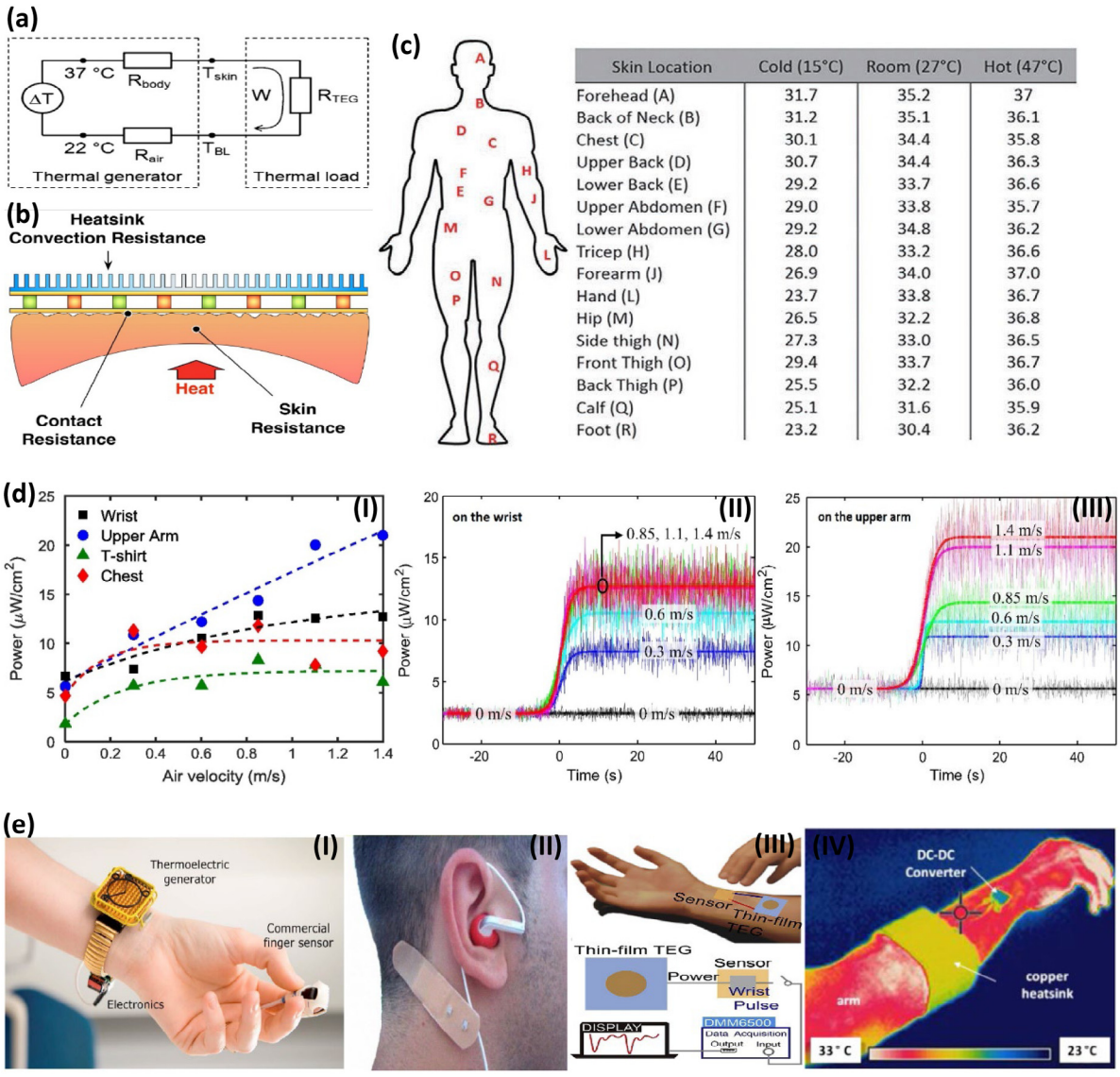

Skin Location	Cold (15°C)	Room (27°C)	Hot (47°C)
Forehead (A)	31.7	35.2	37
Back of Neck (B)	31.2	35.1	36.1
Chest (C)	30.1	34.4	35.8
Upper Back (D)	30.7	34.4	36.3
Lower Back (E)	29.2	33.7	36.6
Upper Abdomen (F)	29.0	33.8	35.7
Lower Abdomen (G)	29.2	34.8	36.2
Tricep (H)	28.0	33.2	36.6
Forearm (J)	26.9	34.0	37.0
Hand (L)	23.7	33.8	36.7
Hip (M)	26.5	32.2	36.8
Side thigh (N)	27.3	33.0	36.5
Front Thigh (O)	29.4	33.7	36.7
Back Thigh (P)	25.5	32.2	36.0
Calf (Q)	25.1	31.6	35.9
Foot (R)	23.2	30.4	36.2

Fig. 17. (a) The Schematic of the thermal circuit for a typical thermoelectric generator (TEG) attached to the skin (Leonov and Vullers, 2009b), with permission of Springer Nature, copyright 2009. (b) The illustration of three main resistance directly affecting the performance of TEG (Suarez et al., 2016), with permission of Royal Society of Chemistry, copyright 2016. (c) The variation of human skin temperatures at different skin locations and ambient temperatures (Webb, 1992), with permission of Springer, copyright 1992. (d) The output TE powers from TEG (I) are worn on the chest, T-shirt, upper arm, and wrist. The output TEG power on (II) upper arm and (III) wrist varies with variant walking speeds of humans (Hyland et al., 2016), with permission of Elsevier Ltd., copyright 2016. (e) The biomedical applications of TEG for (I) body-powered wireless pulse oximeter (Leonov and Vullers, 2009a), with permission of American Institute of Physics, copyright 2009. Powering (II) biomedical hearing aids (Lay-Ekuakille et al., 2009), with permission of IEEE, copyright 2009. The (III) wrist pulse monitor via pressure sensing (Wang et al., 2020b), with permission of Elsevier Ltd., copyright 2020. The (IV) photo-thermal image of the human arm attached to TE device at room temperature (Settaluri et al., 2012), with permission of Elsevier Publishing, copyright 2012.

of the body generate similar output powers when the person is not moving, as shown in Figs. 17d-II, III (Jia et al., 2021). The electrocardiogram sensors exhibit ideal integration in the upper chest and arm (Lay-Ekuakille et al., 2009). Additionally, the first practical application of wearable TEG for biomedical applications is the wireless pulse oximeter, as displayed in Fig. 17e-I (Jia et al., 2021). The pulse oximeter was fully powered by a TEG in watch-style to harvest human body heat. The device consumed around 62 μW and transmitted every 15 s its processed measurement results (Jia et al., 2021). The connected TEG to the device resulted in a full energy autonomous system and returned in producing 100 μW by TEG at an ambient temperature of 22 °C more than the required input power of 89 μW from TEG (Uhl et al., 2015). It is also reported that the wearable TEG is capable to extract the warmth from body tissues for power supplying of hearing aids, as shown in Fig. 17e-II (Jia et al., 2021). The self-powered pressure sensing system has the capabilities to assess health monitoring. For instance, the flexible TEG is taped directly to human skin to harvest its heat, while the pressure-sensing system is positioned in the human body at different parts to monitor the motion activities and physiological signals, as illustrated in Figs. 17e-III, IV (Wang et al., 2020b; Li et al., 2019). The measured pulse signals from the wrist are then transmitted to the laptop for analysis and visualization (Uhl et al., 2015).

5.2. Energy harvesting

The hybrid energy conversion device is based on a bottom layer of thermoelectric to convert waste heat into electricity, center two layers of pyroelectric/photothermal polymer to convert extra light into electricity and heat, and then followed by a top photovoltaic layer works on converting the visible-light

energy into electricity, as demonstrated in Fig. 18a (Kim et al., 2016b). Recently, the new generation of hybrid energy devices is pairing solar cells with heat harvesters (Kim et al., 2016b). This enhanced its capability to capture more of the sun's energy and then convert it into electricity than the solar cell alone (Gong and Krishnan, 2019). The scaling-up of this hybrid device into larger sizes could lead to energy-saving windows acting as commercial solar panels and overcoming the limited energy harvesting of panels to only part of the radiation in exposure to it (Longtin et al., 2013). The remaining solar spectrum is not conserved and lost as heat and then capturing this heat requires combining solar cells with TE devices to harvest the non-conserved heat into electricity (Longtin et al., 2013). The combining of all these materials together is challenging and the selection of proper material is of high importance to transfer the light and heat from one part of the hybrid energy device into the others.

The CuI thin films have high hole conductivity and well-aligned VBM with the developing solar absorber layers as Methylammonium Lead Iodide ($MAPbI_3$) perovskite (Choi et al., 2014). Thus, the TEG based on CuI thin films is utilized as a low-cost and promising energy hybrid device for perovskite solar cells (Choi et al., 2014). This is beneficial for enhancements of efficiency in power conversion and solar cell stability. It is reported that the CuI thin films integrated into solar cells with a thickness of 1.5 μm have been deposited on a porous $MAPbI_3/TiO_2$ layer using the computerized drop-casting technique at low temperatures and have shown good power conversion efficiencies reaching 6.0% in remarkable photocurrent stability (Choi et al., 2014). The previous hybrid devices have not shown enough output power and then conductive polymers are used to improve the efficiency of the hybrid device to attain sufficient voltage satisfying the power requirements of electrochromic windows, which darken in response to electricity (Kim et al., 2018). Recently, the multilayer device involves 3 different energy harvesters targeting to capture more of the available visible light and heat (Kim et al., 2018). The dye-sensitized solar cell is the top layer owing a low efficiency and advantage in its transparency. The uncaptured solar radiation is then converted into electricity by passing into the other downward layers.

The center layer is the core of the device and it is based on a stack of transparent polymer electrodes, pyroelectric polymer covered with conductive on two sides, and then transparent PEDOT polymer (Tung et al., 2011). This part is responsible for converting the uncaptured visible light to heat and then part of this heat to electricity. The bottom photothermal/pyroelectric layer is pasted with conductive paste to the TE layer aiming to convert the remained heat energy into electric energy, as displayed in Fig. 18a (Kim et al., 2016b). The addition of a TE conversion device into the solar cell has boosted its overall output power efficiency by 20% in comparison to a solar cell alone (Kim et al., 2016b). This design of the hybrid device has attracted attention due to its boosted output voltage resulting in enough power for a light-emitting diode (LED) and electrochromic display, which was not attainable via solar cell alone (Motoasca, 2019). Currently, the works are drawn to make larger versions of this hybrid energy device to power windows, which are darkened in response to heat and sun to improve building cooling. The power conversion efficiency of the hybrid device has increased significantly to 41.3% at concentrated light (Kim et al., 2016b). The combination of unsimilar heat-converting devices with solar cells instead of using the devices of TE or pyroelectric separately has increased the overall power conversion efficiency of the hybrid device with minor loss across connections between them (Motoasca, 2019). Thus, it is demanded to optimize the conversion efficiency of each layer in the hybrid device through the use of advanced nanostructured thin films to broaden the energy harvesting onto large areas as windows.

Additionally, the pre-discussed 3-layer hybrid structure based on sandwiching the photothermal/pyroelectric film in between the photovoltaic cell and TE module has shown the photocurrent density–voltage (J–V) characteristic curve, as displayed in Fig. 18b (Kim et al., 2016b). This hybrid device is based on photovoltaic cells connected in series. The enhanced photoconversion efficiency (PCE) reaching 15%–20% confirms the photothermal effect of the hybrid device to be higher than the photovoltaic cell alone. The light intensity contributes to enhancing the PCE of the device as its incrementation will lead to a higher temperature gradient and then PCE reaching 41.3%, as presented in Fig. 18c (Kim et al., 2016b). This multilayer hybrid energy conversion harvesting system boosts the energy conversion efficiency in a simpler structure and assists in building the next generation of self-powered smart windows (D. Bari et al., 2016). The photothermal film has a crucial role in converting uncaptured light into a beneficial heat source, which will result in enough energy conversion efficiency and output voltage for electrochromic windows (D. Bari et al., 2016). Thus, the integrated system of the window, energy converters, energy storage, switching, and circuits needs further optimization to minimize the energy loss caused by the integration (D. Bari et al., 2016). The main challenge is attaining a flexible self-powered based on the smart-film device utilizing efficient hybrid energy harvesters.

5.3. Smart miniaturized electronics

The flexible thin film-based TE device has shown a high ZT value referred to the ultra-low thermal and enhanced electrical conductivities (Yang et al., 2017b). Thus, it is crucial to examine its real-time performance for the structural design of TE devices. It is reported that the thin films have been commonly used for a wearable electronic power source with generated output voltage from body heat reaching 5.3 mV at normal body temperature, as shown in Fig. 19a (Karthikeyan et al., 2020). This voltage is satisfying the standard power requirements of the wristwatch through storage of the output power from the TE generator via an external circuit, as illustrated in Fig. 19b (Karthikeyan et al., 2020). The corresponding infrared photo-thermal images demonstrate the thermal profile of the temperature gradient applied on the TE device, as displayed in Figs. 19d, e, and f (Karthikeyan et al., 2020). The real-time load features of the TE device based on flexible thin films have shown current(I)-voltage(V)-power(P) characteristics at dissimilar temperature gradients (ΔT) from 20 to 120 °C, as presented in Fig. 19g (Karthikeyan et al., 2020). The measured output power for various external resistance has an ultrahigh peak at 0.366 μW in ΔT close to 120 °C. A P–V curve exhibits a characteristic rise in output P with every increase in ΔT. Consequently, the TE device displays a maximum TE performance at the highest ΔT of 120 °C with output current and voltage of 6 μA and 250 mV, respectively. This is the highest TE performance recorded for an in-plane flexible thin-film-based TE device (Nesarajah and Frey, 2017; Terasaki, 2005).

Additionally, the real-life application of flexible TE devices in the industry has been investigated with different types of heat sources (Chen, 2016). For instance, the thin film-based TE device has been connected in series on the surface of an exhaust pipe with hot air as a waste heat harvesting source, as demonstrated in Fig. 19c (Karthikeyan et al., 2020). The curve of load characteristics shows a constant current and voltage up to 10 μA and 500 mV, as displayed in Fig. 19h (Karthikeyan et al., 2020). The infrared images illustrate the property of metallic glass for TE materials in thin-film structure with sustaining the ΔT. Consequently, the incrementation of surface area for TE devices based on thin film boosts the harvesting of a large amount of waste heat into the surroundings. It is reported that a large area TE device of

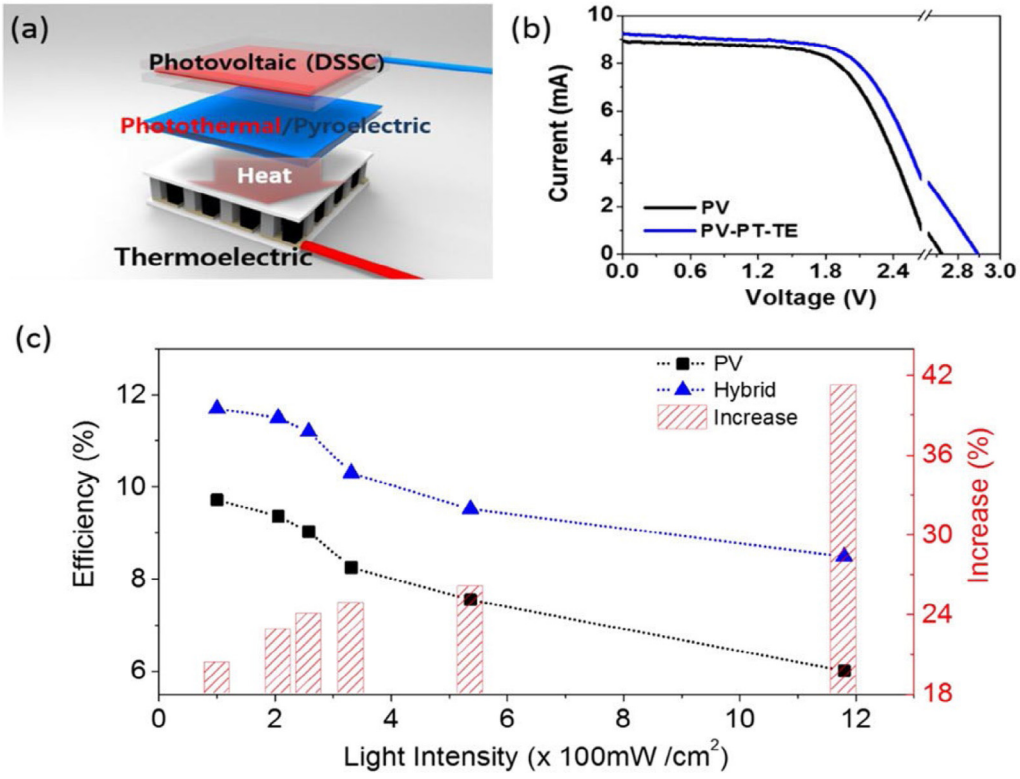

Fig. 18. (a) The Schematic of a hybrid energy device based on 3 layers of dye-sensitized solar photovoltaic cell, photothermal/pyroelectric device, and then followed by thermoelectric device. (b) The characteristic curves of photocurrent density–voltage (J–V) of photovoltaic and photothermally driven TE module. (c) The Dependence of conversion efficiency and increase percent in hybrid device efficiency on light intensity (Kim et al., 2016b), with permission of SPIE, copyright 2016.

50 cm^2 has been fabricated based on 32 p–n TE pairs and enfolded about the human wrist for direct conversion of its wasted heat into electricity resulting in an efficient power supply to LED in small intensity (Minnich et al., 2009). The produced output voltage is dependent on ΔT between the ambient (ΔT=10 °C) and human wrist temperature. This is stabilized with LTC 3108 energy harvester circuit for powering the LED (Minnich et al., 2009). The stability in TE device performance is proven over 150 thermal cycles on either curved or flat surfaces without any significant change in the device's internal electrical resistance (Zhao et al., 2019b).

6. Challenges and limitations

The flexible and transparent TE devices based on p-type CuI thin films have undergone notable progress in the past decade. The high ZT values were reported for flexible CuI films deposited using different developing fabrication methods to endow the target with high TE performance and reserve good flexibility and transparency at the device level (Coroa et al., 2019). The intrinsic plastic deformability of inorganic CuI TE films has been also discovered. It has been reported many flexible CuI-based TE devices in different configurations and growth techniques generate electricity at μW-level in the same temperature gradient (Murmu et al., 2021; Coroa et al., 2019; Liu et al., 2021; Klochko et al., 2019b). These devices have shown sufficient ability to support the electrical power of miniaturized electronics such as a pulse oximeter (Kumar et al., 2019), glucose sensor (Wang et al., 2020b), and electroencephalogram in wearables (Hyland et al., 2016). The application of flexible CuI TE devices has not been limited in power supply for wearable electronics. It has been also integrated into self-powering electronics attached to human skin for detecting environmental thermal stimuli (Bahk et al., 2015). It could be integrated into wearable virtual reality (VR) devices to form hot or cold spirits and bring the good immersive practice to the wearers (Jouhara et al., 2021).

However, it should be noted that there are still many areas for optimization to advance the flexible and transparent CuI TE devices for large-scale applications. Primary, the generated power density by the flexible TE device is considerably lower than conventional bulk TE devices (Karthikeyan et al., 2020). Though the application of normalized maximum power density has not shown any obvious difference. This poor power density of CuI flexible TE devices originated principally from the flexible TE materials possessing poorer ZT and PF than the bulk TE materials in conventional rigid TE devices (Wang et al., 2020a). Additionally, the TE thin films in flexible TE devices are commonly fabricated through printing or deposition methods compared to the bulk TE materials undergoing long-term consolidation and annealing processes (Choi et al., 2018). Thus, the printed or deposited thin film TE materials probably possess poor crystallinity, unoptimized carrier concentration, or low density (Choi et al., 2018). This would result in lowering power density at the device level and then poor TE performance. It is frequently observed the high sensitivity of power density for flexible TE devices to electric or thermal contact resistance, particularly nearby the interfaces (Yu et al., 2020). Whereas the conventional bulk TE devices having a thickness in mm or cm showed negligible deterioration within their power density from electrical contact resistivities of less than 10 μΩ cm^2 (Yu et al., 2020).

Therefore, the TE legs of flexible TE devices should have a length of less than 100 μm or 10 μm to ensure their mechanical flexibility (Picard et al., 2013). This leads to high sensitivity of electric contact resistivity with small magnitude to induce large deterioration on the power density of flexible TE device. This could be the main reason for relatively low power density in high flexibility TE devices based on CuI thin films (Zhang

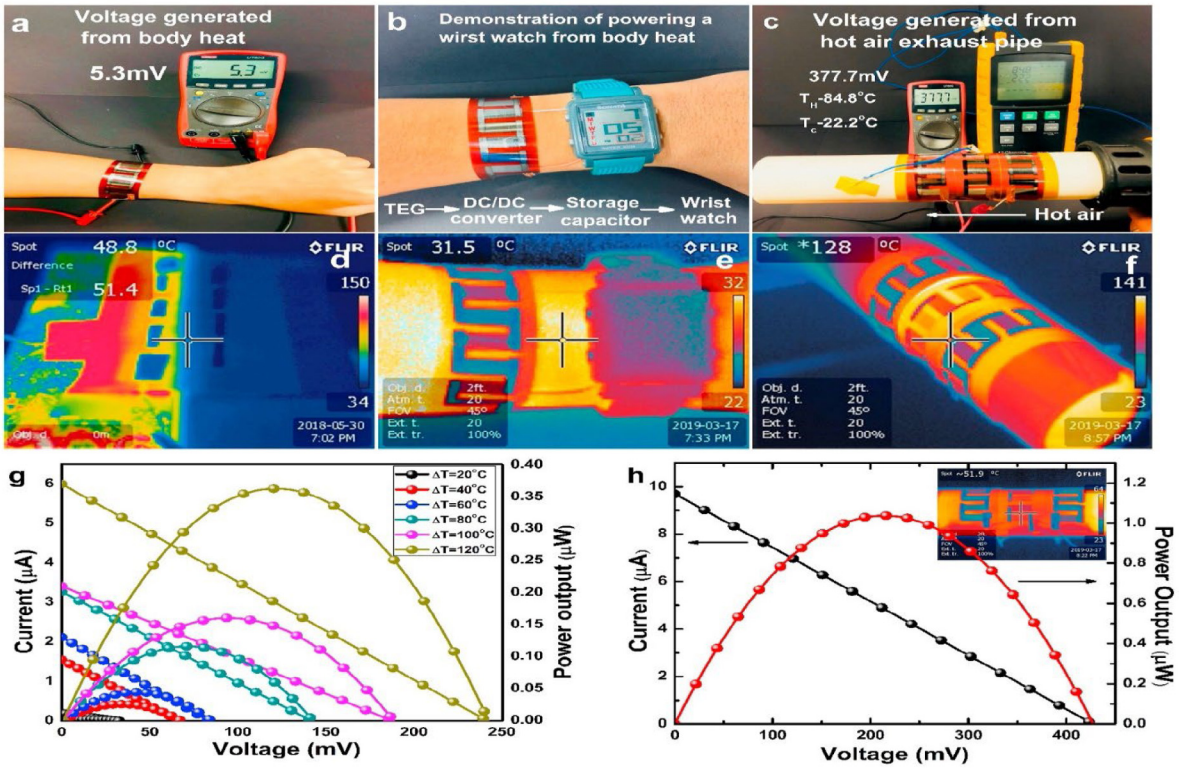

Fig. 19. The Capability of a flexible TE device based on the thin film in generating an output voltage from the heat of (a) the human body and then (b) supplying electricity to wearable electronics for the replacement of chemical batteries. (c) The Harvesting of high-temperature industrial power from heat exchangers. (d), (e), and (f) are the infrared photo-thermal images of TE devices at different heat sources with the capability of conserving a temperature difference. (g) The Load characteristics performance varied at different temperature gradients from a single industrial TE generator. (h) The Load characteristics performance at a temperature gradient of 120 °C for industrial TE generators connected in series on an alumina pipe (Karthikeyan et al., 2020), with permission of Elsevier Ltd., copyright 2020.

et al., 2021). Thus, the two main approaches to improving the power density for flexible TE devices are through diminishing the thermal/electric contact resistances across the interfaces and enhancing the flexible TE performance of TE materials (Chu et al., 2020). The theoretical structure design is also demanded to maintain flexible TE devices (Terasaki, 2005). The structure of a flexible TE device includes its legs number, dimension, TE material, substrate thickness, filler materials among legs, and fill factor (Ortega et al., 2017). These all require a good design for sufficient heat harvesting from human skin by considering the curve surface of the skin, the complex heat flux distribution, and the small temperature gradient between the ambient and human skin. Additionally, the flexible TE devices have frequently experienced stretching or bending process during the operation and then the mechanical performance particularly near the area of the interface needs more attention. Recently, the Ag paste has shown the best electrical contact of TE materials to electrodes, while its mechanical performance has been infrequently examined (Zhang et al., 2015).

On the other hand, the cost is also an important factor to be considered for large-scale applications of flexible TE devices based on CuI thin films. It demands the TE material to be cheap, earth-abundant, and undergo a facile fabrication process to easiness its mass production at a low cost. The lower-cost TE devices are usually based on organic TE materials, which are recognized with poorer TE performance compared to the inorganic TE materials and devices (Gayner and Kar, 2016). The inorganic TE thin films and flexible TE devices have grown through physical techniques such as magnetron sputtering, molecular beam epitaxy, and pulsed laser deposition usually exhibit better quality and higher power density but are more expensive than those synthesized via printing techniques like inkjet printing, dispenser printing, and screening printing (Choi et al., 2018). Accordingly, the trade-off between cost and performance is usually necessary for transparent and flexible TE devices in real applications. Thus, the development of transparent and flexible TE devices based on p-type CuI thin films is still very complicated compared to conventional TE devices based on bulk TE materials.

Moreover, the main reported challenges to enhancements of TE performance for the CuI thin films are moisture attacks and instabilities under O_2 exposure. The degradation of CuI films has been attributed to grain growth, recrystallization, undesired CuI oxidation, and iodine loss. However, still, additional efforts are demanded to demonstrate the degradation mechanism of CuI, especially when exposed to the air to ensure its stabilized TE performance for commercialization. The optimum effective and direct approach to overcome the CuI degradation is through encapsulating or passivating the device for its physical isolation from the external stimuli in the surrounding environment. It is also observed that the higher stability is expected to be a result of improvements in component engineering or film quality. The diffusion of moisture/O_2 in polycrystalline p-type CuI thin films occurs mainly along with the pinholes and grain boundaries (Zhang et al., 2020c). The pristine CuI films exhibit a rapid capability for crystallization and facile aggregation with poor topography. Thus, the solvent/additive engineering methods are predictable to grow uniform, pinhole-free, high-quality, and dense CuI thin film for better TE performance.

The CuI films have not shown any weight variation at operation temperatures under 300 °C in the air (Coroa et al., 2019). Though, the mutual failure of CuI film in TE devices is referred to as iodine decomposition at elevated temperatures. This occurs particularly in harsh environments with high temperatures or

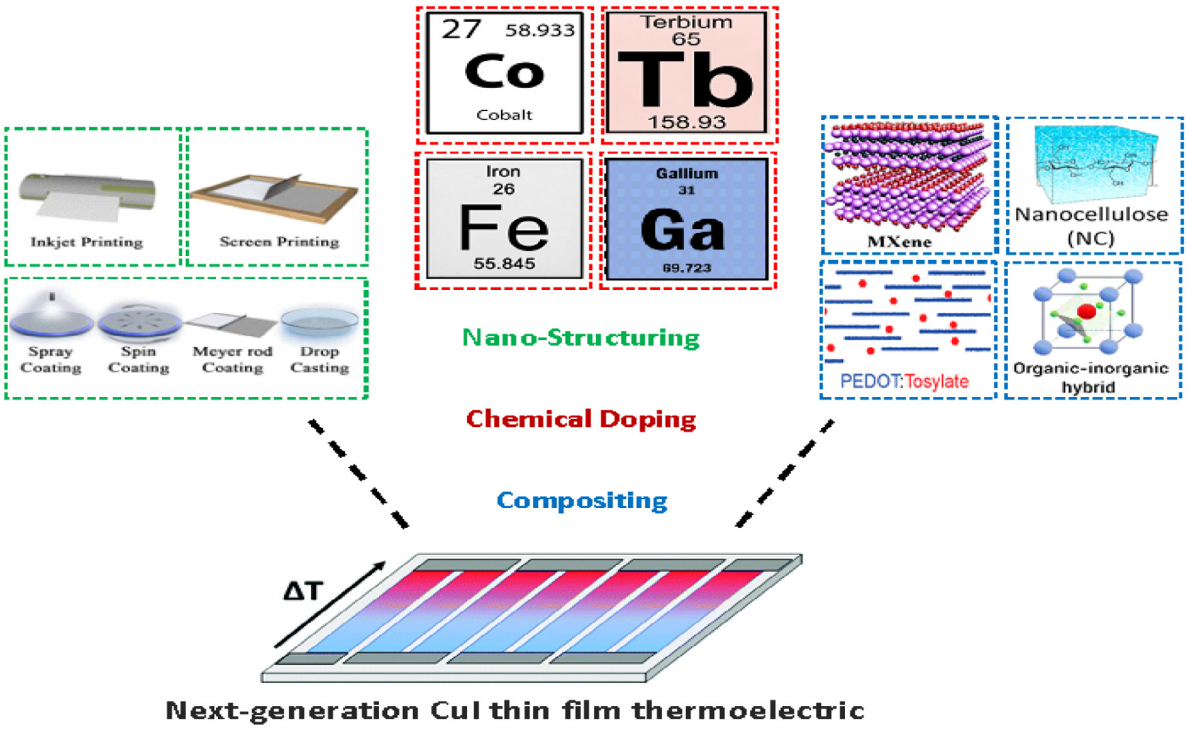

Fig. 20. Prospects in boosting the thermoelectric performance of next-generation flexible and transparent TE devices based on p-type CuI thin films.

gradients leading to either irreversible or reversible iodine decomposition. The irreversible case led to the evaporation of iodine and leaving the CuI film, while in reversible cases the iodine ions are temporarily dissociated in the lattice with the ability to return to their original positions (Yang et al., 2016a). This could be reduced through the encapsulation of CuI films resulting in a great advantage to TE device processing simplicity and performance. Additionally, the p-type CuI thin films have air-sensitive features, which are essential to be considered for the advancement of practicable patterning processes and materials. This is critical for circuit integration and additional practical applications.

7. Outlook and future prospects

The prospects indicate that the next generation of CuI thin film TE devices will be based on three main approaches namely nano-structuring, chemical doping, and compositing, as shown in Fig. 20. The deposition techniques are preferred to be printing or coating for large-scale production at low processing costs (Choi et al., 2018). The chemical doping of gamma phase p-type CuI films with proper activators will enhance its Seebeck coefficient (S) and electrical conductivity (σ). Among different metallic dopants, Cobalt (Co), Terbium (Tb), Iron (Fe), and Gallium (Ga) are the most effective for boosting the TE performance of CuI films (Salah et al., 2020). The concentration of these dopants needs optimization to maximize the PF and ZT of doped CuI film. Recently, the doping of CuI nanoparticles with 0.05 mol% Tb has shown good boosting of their PF from 30 to 210 $\mu W/m\ K^2$ (Salah et al., 2020). Such enhancement is associated with the integration of this dopant in mixed chemical states, which is expected to be a similar case in the film structure.

The compositing approach with MXene, Nanocellulose, PEDOT: Tosylate, and organic–inorganic hybrid will lower further the thermal conductivity (k) of CuI films (Rousti et al., 2021; Salas et al., 2010; Li et al., 2021b; Karthikeyan et al., 2021). This is through offering additional scattering sites for strong phonons scattering at grain boundaries and matrix/filler interfaces. For instance, the compositing of 2D γ-CuI nanoflakes with 5 Vol.% of Ti_3C_2 MXene has exhibited an interlaced architecture of CuI/Ti_3C_2 composite and suppression of high- to mid-frequency phonons (Karthikeyan et al., 2021). This could be superpositioned on the CuI films for tuning their ZT values as the MXenes hold equivalent band alignment with CuI and exhibit metallic transport behavior. The adopting and optimizing of these different advancing approaches will result in CuI films with the desired "electron–crystal, phonon–glass" model for future sustainable energy sources. This will also satisfy the power requirement of medical implantable devices and wearable electronics.

The consideration of the following key points is also essential to achieving high-performance flexible and transparent TE devices based on CuI films for reliable power management.

1. CuI TE material: needs further enhancements of its intrinsic TE properties. The ZT is the critical parameter in evaluating the performance of TE generators. The trade-off exists in TE primary parameters namely the Seebeck coefficient, electrical conductivity, and thermal conductivity. The basic objective on the CuI material level is the effective decoupling of these parameters. A great promise for further exploration is through synthesizing nanostructured and low-dimensional TE materials in 2D or 1D, which will lead simultaneously to confines thermal vibration and anisotropic charge transport. The effects of phonon scattering and energy filtering in single-component TE CuI could be enhanced with composition. The composition with foreign particles has repeatedly shown improvement in the TE properties as in ionic TE conductors through ion–dipole interaction (Uhl et al., 2015). Thus, the optimum design of composites is feasible by an adjusted nanostructure to maximize the TE-enhanced effects. There is also a need to investigate the components' interactions and phonon/electron transportation modes across TE composites based on CuI films.

2. CuI synthesis techniques: the performance of flexible TE devices is strongly impacted by the synthesizing techniques. The PVD techniques have retained good TE performance for inorganic TE materials but are quite time-consuming and costly (Karthikeyan et al., 2020). Whereas, the CVD methods are attracting great attention to develop solution-processable TE materials due to their facile, low cost, and scalability for device assembly. Thus, it is greatly needed to develop stable and high-performance CuI TE inks to enhance such printing methods.
3. CuI film flexibility: the flexibility of TE devices is frequently attained via depositing TE materials in a thick layer with a thickness of μm over a flexible substrate (Li et al., 2019). The flexibility in such design denotes flexibility in bending and is commonly characterized via the bending radius. Good compressibility and stretchability are essential for wearable and miniaturized electronics. Thus, the development of free-standing flexible TE devices based on intrinsic flexible TE material could have great future potential. The applications of most flexible TE devices still depend on the perpendicular ΔT to the heat source (Siddique et al., 2017). The majority of the flexible TE devices are based on thin-film structure and under through-plane ΔT it is challenging to make complete utilization of TE thin films. Thus, appropriate structural design with mechanical creativity might assist in improving the use effectiveness of flexible TE devices in practice. In addition, the electrical contacts between the TE legs are necessary to have good adaptability. The development of integral devices might reduce the contact resistances through an alternating pattern of n- and p-legs on a single configuration lacking extra contacts.
4. Performance enhancements of CuI TE-based devices: this is essential in widening the use of TE technology in more potential applications. Presently emerges the advancements of innovative TE devices integrating different effects of energy conversion as a future approach, which is currently in its early phase. The performance of such hybrid energy harvesting devices is still distant from the power requirements of practical applications, even though the concept is demonstrated sufficiently. Thus, excessive efforts are required towards the performance improvements of such hybrid technology devices for multi-energy harvesting and their potentiality in other multifunctional devices.

8. Conclusions

In summary, thermoelectric devices based on flexible and transparent CuI thin films have witnessed tremendous development in the past decade, particularly in the field of microelectronic thin-film devices. The CuI thin films could be easily fabricated using dissimilar physical or chemical deposition techniques at plastic-compatible temperatures in comparison to other conventional p-type metal oxide and chalcogenide TE materials. The deposition by vacuum methods is based on masks to accomplish the processed patterns compared to solution processes demanding template-assisted patterning machinery or inkjet printing to comprehend the cohesive device array. The spin-coating and thermal evaporation processes have enabled the deposition of thin films CuI at low deposition temperatures with smooth surface morphology. The high film quality p-type CuI with higher conductivity has been deposited through the physical vapor methods. The application of CuI thin films as the p-type TE material within flexible and transparent TE devices requires smooth surface roughness to preserve its good optical transparency. The high conductivity of p-type CuI films favors the iodine-rich deposition condition. The further boosting of CuI thin films' electrical conductivity demands the iodine substitution with chalcogen elements as S^{2-}, which is feasible and worth to be pursued. Future studies had better pay more consideration to the stability difficulties of CuI thin film-based TE devices by developing a suitable encapsulation technique or passivation material to ensure strong device operation in the air. The influence of the dielectric environment on charge transport property within CuI thin films still needs more investigation. The low production cost, intrinsically high mobility, and conductivity of p-type CuI thin films simplify its optimization process towards the stabilized performance of flexible and transparent TE devices.

CRediT authorship contribution statement

Aicha S. Lemine: Conceptualization, Writing – original draft. **Jolly Bhadra:** Writing – review & editing. **Noora J. Al-Thani:** Writing – review & editing. **Zubair Ahmad:** Writing – review & editing.

Declaration of competing interest

The authors declare that they have no known competing financial interests or personal relationships that could have appeared to influence the work reported in this paper.

Data availability

Data will be made available on request.

Acknowledgments

This work was supported by Qatar University Grant no. GTRA-17722. The statements made herein are solely the responsibility of the authors. Open Access funding is provided by the Qatar National Library. All authors have read and agreed to the published version of the manuscript.

References

Ahiska, R.R., Mamur, H., 2014. A review: Thermoelectric generators in renewable energy. Int. J. Renew. Energy Res. 4, 128–136. http://dx.doi.org/10.1016/j.prevetmed.2004.11.005.

Alam, H., Ramakrishna, S., 2013. A review on the enhancement of figure of merit from bulk to nano-thermoelectric materials. Nano Energy. 2, 190–212. http://dx.doi.org/10.1016/j.nanoen.2012.10.005.

Amalina, M.N., Azilawati, Y., Rasheid, N.A., Rusop, M., 2013. The properties of copper (I) iodide (CuI) thin films prepared by mister atomizer at different doping concentration. Procedia Eng. 56, 731–736. http://dx.doi.org/10.1016/j.proeng.2013.03.186.

Amalina, M.N., Zainun, A.R., Rusop, M., 2010. Photoconductivity of copper (I) iodide (CuI) thin films for dye-sensitized solar cells. In: ICECE 2010-6th Int. Conf. Electr. Comput. Eng. pp. 757–760. http://dx.doi.org/10.1109/ICELCE.2010.5700803.

Annadi, A., Zhang, N., Lim, D.B.K., Gong, H., 2019. Hole transport modulations in low dimensional γ-CuI films: Implication for high figure of merit and thin film transistors. ACS Appl. Electron. Mater. 1, 1029–1037. http://dx.doi.org/10.1021/acsaelm.9b00177.

Aouaj, M.A., Diaz, R., Belayachi, A., Rueda, F., Abd-Lefdil, M., 2009. Comparative study of ITO and FTO thin films grown by spray pyrolysis. Mater. Res. Bull. 44, 1458–1461. http://dx.doi.org/10.1016/j.materresbull.2009.02.019.

Ashida, T., Miyamura, A., Oka, N., Sato, Y., Yagi, T., Taketoshi, N., Baba, T., Shigesato, Y., 2009. Thermal transport properties of polycrystalline tin-doped indium oxide films. J. Appl. Phys. 105, 0–4. http://dx.doi.org/10.1063/1.3093684.

Baerlocher, C., Mccusker, L.B., 1994. Practical aspects of powder diffraction data analysis. Stud. Surf. Sci. Catal. 85, 391–428. http://dx.doi.org/10.1016/S0167-2991(08)60775-2.

Bahk, J.H., Fang, H., Yazawa, K., Shakouri, A., 2015. Flexible thermoelectric materials and device optimization for wearable energy harvesting. J. Mater. Chem. C. 3, 10362–10374. http://dx.doi.org/10.1039/c5tc01644d.

Bai, Z., Chen, S.C., Lin, S.S., Shi, Q., Lu, Y.B., Song, S.M., Sun, H., 2021. Review in optoelectronic properties of p-type CuCrO2 transparent conductive films. Surf. Interfaces 22, 100824. http://dx.doi.org/10.1016/j.surfin.2020.100824.

Banerjee, A.N., Maity, R., Ghosh, P.K., Chattopadhyay, K.K., 2005. Thermoelectric properties and electrical characteristics of sputter-deposited p-CuAlO2 thin films. Thin Solid Films. 474, 261–266. http://dx.doi.org/10.1016/j.tsf.2004.08.117.

Brahmbhatt, S., Agrawal, J., 2015. A design of thermoelectric cooler and optimization. Int. J. Sci. Technol. Eng. 2, 24–30.

Carvalhaes-Dias, P., Cabot, A., Siqueira Dias, J.A., 2018. Evaluation of the thermoelectric energy harvesting potential at different latitudes using solar flat panels systems with buried heat sink. Appl. Sci. 8, http://dx.doi.org/10.3390/app8122641.

Chandel, R., Singh, S., Prasad, D., Prakash, R., 2022. Review on thermoelectric systems for enhancing photovoltaic power generation. Sustain. Energy Technol. Assessm. 53, 102585. http://dx.doi.org/10.1016/j.seta.2022.102585.

Chen, J., 2016. Design and analysis of a thermoelectric energy harvesting system for powering sensing nodes in nuclear power plant.

Chen, X., Dai, W., Wu, T., Luo, W., Yang, J., Jiang, W., Wang, L., 2018a. Thin film thermoelectric materials: classification, characterization, and potential for wearable applications. Coatings 8, http://dx.doi.org/10.3390/coatings8070244.

Chen, Y., Fan, Z., Zhang, Z., Niu, W., Li, C., Yang, N., Chen, B., Zhang, H., 2018b. Two-dimensional metal nanomaterials: Synthesis, properties, and applications. Chem. Rev. 118, 6409–6455. http://dx.doi.org/10.1021/acs.chemrev.7b00727.

Chen, W., Gong, H., Zeng, K., 2006. Mechanical properties of Cu–Al–O thin films prepared by plasma-enhanced chemical vapor deposition. J. Vac. Sci. Technol. A Vacuum, Surfaces, Film. 24, 537–541. http://dx.doi.org/10.1116/1.2191860.

Chen, G.M., Ma, L.Y., Huang, I.Y., Wu, T.E., 2011. Development of a novel transparent micro-thermoelectric generator for solar energy conversion. In: NEMS 2011-6th IEEE Int. Conf. Nano/Micro Eng. Mol. Syst.. pp. 976–979. http://dx.doi.org/10.1109/NEMS.2011.6017518.

Chen, T., Zheng, Z., Liang, G., Fan, P., 2020a. A new design of a thin-film thermoelectric device based on multilayer-structure module. Nanomaterials 10, http://dx.doi.org/10.3390/nano10050990.

Chen, X., Zhou, Z., Lin, Y.H., Nan, C., 2020b. Thermoelectric thin films: Promising strategies and related mechanism on boosting energy conversion performance. J. Mater. 6, 494–512. http://dx.doi.org/10.1016/j.jmat.2020.02.008.

Chen, S., Zhou, F., Wei, K., Chen, N., Zhong, M., Zhao, J., 2021c. Preparation of cuprous iodide transparent thermoelectric materials by SILAR method. IOP Conf. Ser. Earth Environ. Sci. 647, http://dx.doi.org/10.1088/1755-1315/647/1/012070.

Cheng, H., Du, Y., Wang, B., Mao, Z., Xu, H., Zhang, L., Zhong, Y., Jiang, W., Wang, L., Sui, X., 2018. Flexible cellulose-based thermoelectric sponge towards wearable pressure sensor and energy harvesting. Chem. Eng. J. 338, 1–7. http://dx.doi.org/10.1016/j.cej.2017.12.134.

Choi, H., Jeong, J., Kim, H.B., Kim, S., Walker, B., Kim, G.H., Kim, J.Y., 2014. Cesium-doped methylammonium lead iodide perovskite light absorber for hybrid solar cells. Nano Energy. 7, 80–85. http://dx.doi.org/10.1016/j.nanoen.2014.04.017.

Choi, H., Kim, Y.J., Kim, C.S., Yang, H.M., Oh, M.W., Cho, B.J., 2018. Enhancement of reproducibility and reliability in a high-performance flexible thermoelectric generator using screen-printed materials. Nano Energy 46, 39–44. http://dx.doi.org/10.1016/j.nanoen.2018.01.031.

Chu, J., Huang, J., Liu, R., Liao, J., Xia, X., Zhang, Q., Wang, C., Gu, M., Bai, S., Shi, X., Chen, L., 2020. Electrode interface optimization advances conversion efficiency and stability of thermoelectric devices. Nat. Commun. 11, 1–8. http://dx.doi.org/10.1038/s41467-020-16508-x.

Coroa, J., Morais Faustino, B.M., Marques, A., Bianchi, C., Koskinen, T., Juntunen, T., Tittonen, I., Ferreira, I., 2019. Highly transparent copper iodide thin film thermoelectric generator on a flexible substrate. RSC Adv. 9, 35384–35391. http://dx.doi.org/10.1039/c9ra07309d.

D. Bari, M., Loureiro, J., Pudas, M., Tappura, K., Jaakkola, K., Ruoho, M., Tittonen, I., Volz, S., Pavan, C., Costabello, K., Bollen, 2016. Transflexteg: large area transparent thin film thermoelectric devices for smart window and flexible applications. In: 14th Eur. Conf. Thermoelectr. ECT, pp. 1–2. http://dx.doi.org/10.3030/645241.

Dey, A., Bajpai, O.P., Sikder, A.K., Chattopadhyay, S., Shafeeuulla Khan, M.A., 2016. Recent advances in CNT/graphene based thermoelectric polymer nanocomposite: A proficient move towards waste energy harvesting. Renew. Sustain. Energy Rev. 53, 653–671. http://dx.doi.org/10.1016/j.rser.2015.09.004.

Dong, X., Xiong, S., Luo, B., Ge, R., Li, Z., Li, J., Zhou, Y., 2018. Flexible and transparent organic-inorganic hybrid thermoelectric modules. ACS Appl. Mater. Interfaces. 10, 26687–26693. http://dx.doi.org/10.1021/acsami.8b08696.

Dong, Z., Xu, H., Liang, F., Luo, C., Wang, C., Cao, Z.-Y.Y., Chen, X.-J.J., Zhang, J., Wu, X., 2019. Raman characterization on two-dimensional materials-based thermoelectricity. Molecules. 24, 88. http://dx.doi.org/10.3390/molecules24010088.

Fan, P., Zheng, Z.H., Li, Y.Z., Lin, Q.Y., Luo, J.T., Liang, G.X., Cai, X.M., Zhang, D.P., Ye, F., 2015. Low-cost flexible thin film thermoelectric generator on zinc based thermoelectric materials. Appl. Phys. Lett. 106, 1–5. http://dx.doi.org/10.1063/1.4909531.

Fares, C., Ren, F., Hays, D.C., Gila, B.P., Tadjer, M., Hobart, K.D., Pearton, S.J., 2018. Valence band offsets for CuI on (-201) bulk Ga2O3 and epitaxial (010) (Al0.14Ga0.86)2O3. Appl. Phys. Lett. 113, http://dx.doi.org/10.1063/1.5055941.

Faustino, B.M.M., Gomes, D., Faria, J., Juntunen, T., Gaspar, G., Bianchi, C., Almeida, A., Marques, A., Tittonen, I., Ferreira, I., 2018. CuI p-type thin films for highly transparent thermoelectric p-n modules. Sci. Rep. 8, 1–10. http://dx.doi.org/10.1038/s41598-018-25106-3.

Garner, S., Chowdhury, D., Lewis, S., 2019. Ultrathin Glass Substrates for Thin, Lightweight, Flexible OLED Lighting. http://dx.doi.org/10.1002/msid.1045.

Gayner, C., Kar, K.K., 2016. Recent advances in thermoelectric materials. Prog. Mater. Sci. 83, 330–382. http://dx.doi.org/10.1016/j.pmatsci.2016.07.002.

Gong, J., Krishnan, S., 2019. Mathematical Modeling of Dye-Sensitized Solar Cells. Elsevier Inc. http://dx.doi.org/10.1016/B978-0-12-814541-8.00002-1.

Graužinyte, M., Botti, S., Marques, M.A.L., Goedecker, S., Flores-Livas, J.A., 2019. Computational acceleration of prospective dopant discovery in cuprous iodide. Phys. Chem. Chem. Phys. 21, 18839–18849. http://dx.doi.org/10.1039/c9cp02711d.

Guk, K., Han, G., Lim, J., Jeong, K., Kang, T., Lim, E.K., Jung, J., 2019. Evolution of wearable devices with real-time disease monitoring for personalized healthcare. Nanomaterials 9, 1–23. http://dx.doi.org/10.3390/nano9060813.

Hamid Elsheikh, M., Shnawah, D.A., Sabri, M.F.M., Said, S.B.M., Haji Hassan, M., Ali Bashir, M.B., Mohamad, M., 2014. A review on thermoelectric renewable energy: Principle parameters that affect their performance. Renew. Sustain. Energy Rev. 30, 337–355. http://dx.doi.org/10.1016/j.rser.2013.10.027.

Han, M.K., Jin, Y., Lee, D.H., Kim, S.J., 2017. Thermoelectric properties of Bi2Te3: CuI and the effect of its doping with Pb atoms. Materials (Basel) 10, http://dx.doi.org/10.3390/ma10111235.

He, J., Tritt, T.M., 2017. Advances in thermoelectric materials research: looking back and moving forward. Science (80-.) 357, http://dx.doi.org/10.1126/science.aak9997.

Hou, W., Nie, X., Zhao, W., Zhou, H., Mu, X., Zhu, W., Zhang, Q., 2018. Fabrication and excellent performances of Bi0.5Sb1.5Te3/epoxy flexible thermoelectric cooling devices. Nano Energy 50, 766–776. http://dx.doi.org/10.1016/j.nanoen.2018.06.020.

Hu, X., Fan, X., Feng, B., Kong, D., Liu, P., Xu, C., Kuang, Z., Li, G., Li, Y., 2021a. Decoupling seebeck coefficient and resistivity, and simultaneously optimizing thermoelectric and mechanical performances for N-type BiTeSe alloy by multi-pass equal channel angular extrusion. Mater. Sci. Eng. B Solid-State Mater. Adv. Technol. 263, 114846. http://dx.doi.org/10.1016/j.mseb.2020.114846.

Hu, H.H., Tan, X., Guo, Z., Wang, H., Zhou, Z., Xiong, C., Li, Z., Liu, G., Noudem, J.G., Jiang, J., Yang, G., Sang, L., Mitchell, D.R.G., Fei Yun, F., Wai See, K., Jumlat Ahmed, A., Sayyar, S., Bake, A., Liu, P.P., Chen, L., Yue, Z., Cortie, D., Wang, X., Hu, H.H., Tan, X., Guo, Z., Wang, H., Zhou, Z., Xiong, C., Li, Z., Liu, G., Noudem, J.G., Jiang, J., Hu, X., Fan, X., Feng, B., Kong, D., Liu, P.P., Xu, C., Kuang, Z., Li, G., Li, Y., Zhuang, H.L., Pei, J., Cai, B., Dong, J., Hu, H.H., Sun, F.H., Pan, Y., Snyder, G.J., Li, J.F., 2021b. Synergistically optimized thermoelectric and mechanical properties in p-type BiSbTe by a microdroplet deposition technique. Chem. Eng. J. 263, 114846. http://dx.doi.org/10.1002/ente.202001024.

Hubbard, W.A., Mecklenburg, M., Lodico, J.J., Chen, Y., Ling, X.Y., Patil, R., Kessel, W.A., Flatt, G.J.K., Chan, H.L., Vareskic, B., Bal, G., Zutter, B., Regan, B.C., 2020. Electron-transparent thermoelectric coolers demonstrated with nanoparticle and condensation thermometry. ACS Nano. 14, 11510–11517. http://dx.doi.org/10.1021/acsnano.0c03958.

Hyland, M., Hunter, H., Liu, J., Veety, E., Vashaee, D., 2016. Wearable thermoelectric generators for human body heat harvesting. Appl. Energy. 182, 518–524. http://dx.doi.org/10.1016/j.apenergy.2016.08.150.

Ichi Yanagiya, S., Van Nong, N., Xu, J., Pryds, N., 2010. The effect of (Ag, Ni, Zn)-addition on the thermoelectric properties of copper aluminate. Materials (Basel) 3, 318–328. http://dx.doi.org/10.3390/ma3010318.

Inudo, S., Miyake, M., Hirato, T., 2013. Electrical properties of CuI films prepared by spin coating. Phys. Status Solidi Appl. Mater. Sci. 210, 2395–2398. http://dx.doi.org/10.1002/pssa.201329319.

Jaldurgam, F.F., Ahmad, Z., Touati, F., 2021. Synthesis and performance of large-scale cost-effective environment-friendly nanostructured thermoelectric materials. Nanomaterials 11, http://dx.doi.org/10.3390/nano11051091.

Jia, Y., Jiang, Q., Sun, H., Liu, P., Hu, D., Pei, Y., Liu, W., Crispin, X., Fabiano, S., Ma, Y., Cao, Y., 2021. Wearable thermoelectric materials and devices for self-powered electronic systems. Adv. Mater. 33, 1–46. http://dx.doi.org/10.1002/adma.202102990.

Jin, L., Sun, T., Zhao, W., Wang, L., Jiang, W., 2021. Durable and washable carbon nanotube-based fibers toward wearable thermoelectric generators application. J. Power Sources. 496, 229838. http://dx.doi.org/10.1016/j.jpowsour.2021.229838.

Jouhara, H., Zabnieńska Góra, A., Khordehgah, N., Doraghi, Q., Ahmad, L., Norman, L., Axcell, B., Wrobel, L., Dai, S., 2021. Thermoelectric generator (TEG) technologies and applications. Int. J. Thermofluids. 9, http://dx.doi.org/10.1016/j.ijft.2021.100063.

Jovanovic, V., Ghamaty, S., Bass, J.C., 2012. New thermoelectric materials and applications. In: Intersoc. Conf. Therm. Thermomechanical Phenom. Electron. Syst. ITHERM. pp. 1159–1169. http://dx.doi.org/10.1109/ITHERM.2012.6231554.

Jun, T., Kim, J., Sasase, M., Hosono, H., 2018. Material design of p-type transparent amorphous semiconductor, Cu–Sn–I. Adv. Mater. 30, 1–5. http://dx.doi.org/10.1002/adma.201706573.

Junior, O.H.A., Calderon, N.H., Silva De Souza, S., 2018. Characterization of a thermoelectric generator (TEG) system for waste heat recovery. Energies 11, http://dx.doi.org/10.3390/en11061555.

K. Almasoudi, M., Saeed, A., Salah, N., Alshahrie, A., Hasan, P.M.Z., Melaibari, A., Koumoto, C.u.I., 2022. A promising halide for thermoelectric applications below 373 K. ACS Appl. Energy Mater. 1–3. http://dx.doi.org/10.1021/acsaem.2c01929.

Kanatzidis, M.G., 2010. Nanostructured thermoelectrics: The new paradigm? Chem. Mater. 22, 648–659. http://dx.doi.org/10.1021/cm902195j.

Karthikeyan, V., Surjadi, J.U., Wong, J.C.K., Kannan, V., Lam, K.H., Chen, X., Lu, Y., Roy, V.A.L., 2020. Wearable and flexible thin film thermoelectric module for multi-scale energy harvesting. J. Power Sources. 455, 227983. http://dx.doi.org/10.1016/j.jpowsour.2020.227983.

Karthikeyan, V., Theja, V.C.S., De Souza, M.M., Roy, V.A.L., 2021. Hierarchically interlaced 2D copper Iodide/MXene composite for high thermoelectric performance. Phys. Status Solidi Rapid Res. Lett. 2100419. http://dx.doi.org/10.1002/pssr.202100419.

Kaushik, D.K., Selvaraj, M., Ramu, S., Subrahmanyam, A., 2017. Thermal evaporated Copper Iodide (CuI) thin films: A note on the disorder evaluated through the temperature dependent electrical properties. Sol. Energy Mater. Sol. Cells. 165, 52–58. http://dx.doi.org/10.1016/j.solmat.2017.02.030.

Kawazoe, H., Yasukawa, M., Hyodo, H., Kurita, M., Yanagi, H., Hosono, H., 1997. P-type electrical conduction in transparent thin films of CuAlO2. Nature 389, 939–942. http://dx.doi.org/10.1038/40087.

Kennedy, J.V., Murmu, P.P., Karthik, V., Liu, Z., Jovic, V., Mori, T., Yang, W.L., Smith, K.E., 2020. Influence of carrier density and energy barrier scattering on a high seebeck coefficient and power factor in transparent thermoelectric copper iodide. ACS Appl. Energy Mater. 3, 10037–10044. http://dx.doi.org/10.1021/acsaem.0c01724.

Khors, A., Zak, Abd. Majid, W.H., Abrishami, M.E., Yousefi, R., 2011. X-ray analysis of ZnO nanoparticles by Williamson-Hall and size-strain plot methods. Solid State Sci. 13, 251–256. http://dx.doi.org/10.1016/j.solidstatesciences.2010.11.024.

Kim, J., Da Silva, W.J., Bin Mohd Yusoff, A.R., Jang, J., 2016a. Organic devices based on nickel nanowires transparent electrode. Sci. Rep. 6, 1–7. http://dx.doi.org/10.1038/srep19813.

Kim, H.S., Kikuchi, K., Itoh, T., Iida, T., Taya, M., 2014a. Design of segmented thermoelectric generator based on cost-effective and light-weight thermoelectric alloys. Mater. Sci. Eng. B Solid-State Mater. Adv. Technol. 185, 45–52. http://dx.doi.org/10.1016/j.mseb.2014.02.005.

Kim, H.J., Kim, S.M., Lee, S., Sung, S.K., Min, J.W., Lim, K.H., Lee, T.K., Song, H.E., Kim, Y., Kim, J., Lee, Y., 2022. Rapid evaluation system for photovoltaic cell and thermoelectric generator hybrid devices depending on temperature via transparent heater. ACS Appl. Energy Mater. 5, 2669–2674. http://dx.doi.org/10.1021/acsaem.2c00298.

Kim, J.U., Lee, S., Kang, S.J., Il Kim, T., 2018. Materials and design of nanostructured broadband light absorbers for advanced light-to-heat conversion. Nanoscale 10, 21555–21574. http://dx.doi.org/10.1039/c8nr06024j.

Kim, E., Park, T., Na, J., Kim, B., Kim, Y., Shin, H., 2016b. Photothermal effect of conducting polymer electrodes for hybrid energy harvester. In: SPIE Newsroom. pp. 1–4. http://dx.doi.org/10.1117/2.1201604.006377.

Kim, S.J., We, J.H., Cho, B.J., 2014b. A wearable thermoelectric generator fabricated on a glass fabric. Energy Environ. Sci. 7, 1959–1965. http://dx.doi.org/10.1039/c4ee00242c.

Klochko, N.P., Barbash, V.A., Petrushenko, S.I., Kopach, V.R., Klepikova, K.S., Zhadan, D.O., Yashchenko, O.V., Dukarov, S.V., Sukhov, V.M., Khrypunova, A.L., 2021. Thermoelectric textile devices with thin films of nanocellulose and copper iodide. J. Mater. Sci. Mater. Electron. 32, 23246–23265. http://dx.doi.org/10.1007/s10854-021-06810-9.

Klochko, N.P., Klepikova, K.S., Kopach, V.R., Tyukhov, I.I., Starikov, V.V., Sofronov, D.S., Khrypunova, I.V., Zhadan, D.O., Petrushenko, S.I., Dukarov, S.V., Lyubov, V.M., Kirichenko, M.V., Khrypunova, A.L., 2019a. Development of semi-transparent ZnO/FTO solar thermoelectric nanogenerator for energy efficient glazing. Sol. Energy 184, 230–239. http://dx.doi.org/10.1016/j.solener.2019.04.002.

Klochko, N.P., Zhadan, D.O., Klepikova, K.S., Petrushenko, S.I., Kopach, V.R., Khrypunov, G.S., Lyubov, V.M., Dukarov, S.V., Khrypunova, A.L., 2019b. Semi-transparent copper iodide thin films on flexible substrates as p-type thermolegs for a wearable thermoelectric generator. Thin Solid Films. 683, 34–41. http://dx.doi.org/10.1016/j.tsf.2019.05.025.

Kokubun, M., Watanabe, Y., Wada, H., 1971. Electrical properties of CuI thin films. Japan. J. Appl. Phys. 10, 864–867. http://dx.doi.org/10.1143/JJAP.10.864.

Krishnaiah, M., Kumar, A., Kushwaha, A.K., Song, J., Jin, S.H., 2021. Thickness dependent photodetection properties of solution-processed CuI films: Towards cost-effective flexible visible photodetectors. Mater. Lett. 305, 130815. http://dx.doi.org/10.1016/j.matlet.2021.130815.

Kumar, P.M., Babu, V.J., Subramanian, A., Bandla, A., Thakor, N., Ramakrishna, S., Wei, H., 2019. The design of a thermoelectric generator and its medical applications. Designs 3, 1–26. http://dx.doi.org/10.3390/designs3020022.

Kurtoglu, M., Naguib, M., Gogotsi, Y., Barsoum, M.W., 2012. First principles study of two-dimensional early transition metal carbides. MRS Commun. 2, 133–137. http://dx.doi.org/10.1557/mrc.2012.25.

Labonte, D., Lenz, A.K., Oyen, M.L., 2017. On the relationship between indentation hardness and modulus, and the damage resistance of biological materials. Acta Biomater. 57, 373–383. http://dx.doi.org/10.1016/j.actbio.2017.05.034.

Lal, S., Gautam, D., Razeeb, K.M., 2019. Optimization of annealing conditions to enhance thermoelectric performance of electrodeposited p-type BiSbTe thin films. APL Mater. 7, http://dx.doi.org/10.1063/1.5049586.

Lan, W., Zhang, M., Dong, G., Wang, Y., Yan, H., 2007. Improvement of CuAlO2 thin film electrical conduction by the anisotropic conductivity. J. Mater. Res. 22, 3338–3343. http://dx.doi.org/10.1557/jmr.2007.0437.

Lay-Ekuakille, A., Vendramin, G., Trotta, A., Mazzotta, G., 2009. Thermoelectric generator design based on power from body heat for biomedical autonomous devices. In: 2009 IEEE Int. Work. Med. Meas. Appl. MeMeA 2009. pp. 1–4. http://dx.doi.org/10.1109/MEMEA.2009.5167942.

Lee, K.H., il Kim, S., Kim, H.S., Kim, S.W., 2020a. Band convergence in thermoelectric materials: Theoretical background and consideration on Bi-Sb-Te alloys. ACS Appl. Energy Mater. 3, 2214–2223. http://dx.doi.org/10.1021/acsaem.9b02131.

Lee, S., Lee, H.J., Ji, Y., Choi, S.M., Lee, K.H., Hong, K., 2020b. Vacancy engineering of a solution processed CuI semiconductor: tuning the electrical properties of inorganic P-channel thin-film transistors. J. Mater. Chem. C. 8, 9608–9614. http://dx.doi.org/10.1039/d0tc02005b.

Lee, J.H., Lee, B.H., Kang, J., Diware, M., Jeon, K., Jeong, C., Lee, S.Y., Kim, K.H., 2021. Characteristics and electronic band alignment of a transparent P-CuI/N-SiZnSnO heterojunction diode with a high rectification ratio. Nanomaterials 11, http://dx.doi.org/10.3390/nano11051237.

Lemine, A.S., El-Makaty, F.M., Al-Ghanim, H.A., Youssef, K.M., 2022. Experimental and modeling analysis of p-type Bi0.4Sb1.6Te3 and graphene nanocomposites. J. Mater. Res. Technol. 16, 1702–1712. http://dx.doi.org/10.1016/j.jmrt.2021.12.096.

Lemine, A.S., Zagho, M.M., Altahtamouni, T.M., Bensalah, N., 2018. Graphene a promising electrode material for supercapacitors—A review. Int. J. Energy Res. 42, 4284–4300. http://dx.doi.org/10.1002/er.4170.

Leonov, V., Vullers, R.J.M., 2009a. Wearable electronics self-powered by using human body heat: The state of the art and the perspective. J. Renew. Sustain. Energy. 1, 062701. http://dx.doi.org/10.1063/1.3255465.

Leonov, V., Vullers, R.J.M., 2009b. Wearable thermoelectric generators for body-powered devices. J. Electron. Mater. 38, 1491–1498. http://dx.doi.org/10.1007/s11664-008-0638-6.

Li, C., Jiang, F., Liu, C., Liu, P., Xu, J., 2019. Present and future thermoelectric materials toward wearable energy harvesting. Appl. Mater. Today. 15, 543–557. http://dx.doi.org/10.1016/j.apmt.2019.04.007.

Li, J.F., Pan, Y., Wu, C.F., Sun, F.H., Wei, T.R., 2017a. Processing of advanced thermoelectric materials. Sci. China Technol. Sci. 60, 1347–1364. http://dx.doi.org/10.1007/s11431-017-9058-8.

Li, H., Zong, Y., Li, X., Ding, Q., Jiang, Y., Han, W., 2021b. Biodegradable cui/bcnf composite thermoelectric film for wearable energy harvesting. Cellulose 28, 10707–10714. http://dx.doi.org/10.1007/s10570-021-04244-4.

Liang, A., Jiang, X., Hong, X., Jiang, Y., Shao, Z., Zhu, D., 2018. Recent developments concerning the dispersion methods and mechanisms of graphene. Coatings 8, http://dx.doi.org/10.3390/coatings8010033.

Lin, G., Zhao, F., Zhao, Y., Zhang, D., Yang, L., Xue, X., Wang, X., Qu, C., Li, Q., Zhang, L., 2016. Luminescence properties and mechanisms of CuI thin films fabricated by vapor iodization of copper films. Materials (Basel) 9, http://dx.doi.org/10.3390/ma9120990.

Liu, W., Hu, J., Zhang, S., Deng, M., Han, C.G., Liu, Y., trends, New., 2017. Strategies and opportunities in thermoelectric materials: A perspective. Mater. Today Phys. 1, 50–60. http://dx.doi.org/10.1016/j.mtphys.2017.06.001.

Liu, W., Jie, Q., Kim, H.S., Ren, Z., 2015. Current progress and future challenges in thermoelectric power generation: From materials to devices. Acta Mater. 87, 357–376. http://dx.doi.org/10.1016/j.actamat.2014.12.042.

Liu, C., Li, F., Ma, L.-P., Cheng, H.-M., 2010. Advanced materials for energy storage. Adv. Mater. 22, E28–E62. http://dx.doi.org/10.1002/adma.200903328.

Liu, Y., Shi, Y., Li, J., Guo, X., Wang, Y., Xiang, Q., Guo, S., Ze, R., Zeng, J., Xiang, Y., Hao, F., 2020a. Comprehensive performance prediction and power promotion for wearable thermoelectric generator with flexible encapsulation in practical application. Energy Convers. Manag. 220, http://dx.doi.org/10.1016/j.enconman.2020.113080.

Liu, H., Yuan, X., Lu, P., Shi, X., Xu, F., He, Y., Tang, Y., Bai, S., Zhang, W., Chen, L., Lin, Y., Shi, L., Lin, H., Gao, X., Zhang, X., Chi, H., Uher, C., 2013. Ultrahigh thermoelectric performance by electron and phonon critical scattering in Cu2Se1-xIx. Adv. Mater. 25, 6607–6612. http://dx.doi.org/10.1002/adma.201302660.

Liu, A., Zhu, H., Kim, M.G., Kim, J., Noh, Y.Y., 2021. Engineering copper iodide (CuI) for multifunctional p-type transparent semiconductors and conductors. Adv. Sci. 8, 1–19. http://dx.doi.org/10.1002/advs.202100546.

Liu, A., Zhu, H., Park, W.T., Kang, S.J., Xu, Y., Kim, M.G., Noh, Y.Y., 2018b. Room-temperature solution-synthesized p-type copper(I) iodide semiconductors for transparent thin-film transistors and complementary electronics. Adv. Mater. 30, http://dx.doi.org/10.1002/adma.201802379.

Longtin, J.P., Zuo, L., Hwang, D., Fu, G., Tewolde, M., Chen, Y., Sampath, S., 2013. Fabrication of thermoelectric devices using thermal spray: application to vehicle exhaust systems. J. Therm. Spray Technol. 22, 577–587. http://dx.doi.org/10.1007/s11666-013-9903-1.

Lv, Y., Xu, Z., Ye, L., Zhang, Z., Su, G., Zhuang, X., 2015. Large γ-CuI semiconductor single crystal growth by a temperature reduction method from an NH4I aqueous solution. CrystEngComm. 17, 862–867. http://dx.doi.org/10.1039/c4ce02045f.

Ma, L., Dong, C., Li, W., Xie, E., Lan, W., 2021a. Heavy-ion irradiation assisted modification of p-type transparent CuAlO2 films: Electrical, optical and thermoelectric properties. Vacuum 193, 110498. http://dx.doi.org/10.1016/j.vacuum.2021.110498.

Ma, Z., Wei, J., Song, P., Zhang, M., Yang, L., Ma, J., Liu, W., Yang, F., Wang, X., 2021b. Review of experimental approaches for improving zT of thermoelectric materials. Mater. Sci. Semicond. Process. 121, 105303. http://dx.doi.org/10.1016/j.mssp.2020.105303.

Malik, O., la Hidalga-Wade, F.J.D., 2017. Surface-barrier photodiodes with transparent electrodes for high-performance detection in the UV-NIR spectrum. Optoelectron. Adv. Device Struct. http://dx.doi.org/10.5772/67469.

Martín-González, M., Caballero-Calero, O., Díaz-Chao, P., 2013. Nanoengineering thermoelectrics for 21st century: Energy harvesting and other trends in the field. Renew. Sustain. Energy Rev. 24, 288–305. http://dx.doi.org/10.1016/j.rser.2013.03.008.

Mehdizadeh Dehkordi, A., Zebarjadi, M., He, J., Tritt, T.M., 2015. Thermoelectric power factor: Enhancement mechanisms and strategies for higher performance thermoelectric materials. Mater. Sci. Eng. R Rep. 97, 1–22. http://dx.doi.org/10.1016/j.mser.2015.08.001.

Mehta, R.J., Zhang, Y., Karthik, C., Singh, B., Siegel, R.W., Borca-Tasciuc, T., Ramanath, G., 2012. A new class of doped nanobulk high-figure-of-merit thermoelectrics by scalable bottom-up assembly. Nature Mater. 11, 233–240. http://dx.doi.org/10.1038/nmat3213.

Minnich, A.J., Dresselhaus, M.S., Ren, Z.F., Chen, G., 2009. Bulk nanostructured thermoelectric materials: Current research and future prospects. Energy Environ. Sci. 2, 466–479. http://dx.doi.org/10.1039/b822664b.

Molina-Lopez, F., 2020. Emerging thermoelectric generators based on printed and flexible electronics technology. In: Proc. IEEE Sensors. pp. 1–4. http://dx.doi.org/10.1109/SENSORS47125.2020.9278922, (2020).

Motoasca, E., 2019. Energy sustainability through the use of thermoelectric materials in waste heat recovery systems recent developments and challenges. Energy, Environ. Sustain. 237–254. http://dx.doi.org/10.1007/978-981-13-3284-5_11.

Murmu, P.P., Karthik, V., Chong, S.V., Rubanov, S., Liu, Z., Mori, T., Yi, J., Kennedy, J., 2021. Effect of native defects on thermoelectric properties of copper iodide films. Emergent Mater. 4, 761–768. http://dx.doi.org/10.1007/s42247-021-00190-w.

Nandy, S., Maiti, U.N., Ghosh, C.K., Chattopadhyay, K.K., 2007. Optical and electrical properties of amorphous CuAlO2 thin film deposited by RF magnetron sputtering. In: Proc. 14th Int. Work. Phys. Semicond. Devices. IWPSD, pp. 443–445. http://dx.doi.org/10.1109/IWPSD.2007.4472544.

Nesarajah, M., Frey, G., 2017. Optimized design of thermoelectric energy harvesting systems for waste heat recovery from exhaust pipes. Appl. Sci. 7, 634. http://dx.doi.org/10.3390/app7060634.

O'Dwyer, C., Chen, R., He, H., Lee, J., Razeeb, K.M., 2017. Scientific and technical challenges in thermal transport and thermoelectric materials and devices. ECS J. Solid State Sci. Technol. 6, N3058–N3064. http://dx.doi.org/10.1149/2.0091703jss.

Oh, J., Yoo, H., Choi, J., Kim, J.Y., Lee, D.S., Kim, M.J., Lee, J.C., Kim, W.N., Grossman, J.C., Park, J.H., Lee, S.S., Kim, H., Son, J.G., 2017. Significantly reduced thermal conductivity and enhanced thermoelectric properties of single- and bi-layer graphene nanomeshes with sub-10 nm neck-width. Nano Energy. 35, 26–35. http://dx.doi.org/10.1016/j.nanoen.2017.03.019.

Ong, K.P., Singh, D.J., Wu, P., 2011. Analysis of the thermoelectric properties of n-type ZnO. Phys. Rev. B - Condens. Matter Mater. Phys. 83, 1–5. http://dx.doi.org/10.1103/PhysRevB.83.115110.

Ortega, S., Ibáñez, M., Liu, Y., Zhang, Y., Kovalenko, M.V., Cadavid, D., Cabot, A., 2017. Bottom-up engineering of thermoelectric nanomaterials and devices from solution-processed nanoparticle building blocks. Chem. Soc. Rev. 46, 3510–3528. http://dx.doi.org/10.1039/c6cs00567e.

Park, S.H., Jo, S., Kwon, B., Kim, F., Ban, H.W., Lee, J.E., Gu, D.H., Lee, S.H., Hwang, Y., Kim, J.S., Bin Hyun, D., Lee, S., Choi, K.J., Jo, W., Son, J.S., 2016. High-performance shape-engineerable thermoelectric painting. Nature Commun. 7, 1–10. http://dx.doi.org/10.1038/ncomms13403.

Park, K., Ko, K.Y., Seo, W.S., 2005. Thermoelectric properties of CuAlO2. J. Eur. Ceram. Soc. 25, 2219–2222. http://dx.doi.org/10.1016/j.jeurceramsoc.2005.03.034.

Parker, D., Singh, D.J., 2011. Potential thermoelectric performance from optimization of hole-doped Bi2Se3. Phys. Rev. X. 1, 1–9. http://dx.doi.org/10.1103/PhysRevX.1.021005.

Peng, K., Zhou, Z., Wang, H., Wu, H., Ying, J., Han, G., Lu, X., Wang, G., Zhou, X., Chen, X., 2021. Exceptional performance driven by planar honeycomb structure in a new high temperature thermoelectric material BaAgAs. Adv. Funct. Mater. 31, 1–9. http://dx.doi.org/10.1002/adfm.202100583.

Picard, M., Turenne, S., Vasilevskiy, D., Masut, R.A., 2013. Numerical simulation of performance and thermomechanical behavior of thermoelectric modules with segmented bismuth-telluride-based legs. J. Electron. Mater. 42, 2343–2349. http://dx.doi.org/10.1007/s11664-012-2435-5.

Qiu, J., Yan, Y., Luo, T., Tang, K., Yao, L., Zhang, J., Zhang, M., Su, X., Tan, G., Xie, H., Kanatzidis, M.G., Uher, C., Tang, X., 2019. 3D printing of highly textured bulk thermoelectric materials: mechanically robust BiSbTe alloys with superior performance. Energy Environ. Sci. http://dx.doi.org/10.1039/c9ee02044f.

Ren, W., Sun, Y., Zhao, D., Aili, A., Zhang, S., Shi, C., Zhang, J., Geng, H., Zhang, J., Zhang, L., Xiao, J., Yang, R., 2021. High-performance wearable thermoelectric generator with self-healing, recycling, and lego-like reconfiguring capabilities. Sci. Adv. 7, http://dx.doi.org/10.1126/sciadv.abe0586.

Riffat, S.B., Ma, X., 2003. Thermoelectrics: A review of present and potential applications. Appl. Therm. Eng. 23, 913–935. http://dx.doi.org/10.1016/S1359-4311(03)00012-7.

Rousti, A.M., Maji, T., Drew, C., Kumar, J., Christodouleas, D., 2021. High-performance thermoelectric fabric based on PEDOT:Tosylate/CuI. Appl. Mater. Today. 25, 101180. http://dx.doi.org/10.1016/j.apmt.2021.101180.

Ruan, S., Luo, D., Li, M., Wang, J., Ling, L., Yu, A., Chen, Z., 2021. Synthesis and functionalization of 2D nanomaterials for application in lithium-based energy storage systems. Energy Storage Mater. 38, 200–230. http://dx.doi.org/10.1016/j.ensm.2021.03.001.

Sakamoto, K., Kuwae, H., Kobayashi, N., Nobori, A., Shoji, S., Mizuno, J., 2018. Highly flexible transparent electrodes based on mesh-patterned rigid indium tin oxide. Sci. Rep. 8, 3–4. http://dx.doi.org/10.1038/s41598-018-20978-x.

Salah, N., Abusorrah, A.M., Salah, Y.N., Almasoudi, M., Baghdadi, N., Alshahri, A., Koumoto, K., 2020. Effective dopants for CuI single nanocrystals as a promising room temperature thermoelectric material. Ceram. Int. 46, 27244–27253. http://dx.doi.org/10.1016/j.ceramint.2020.07.209.

Salas, E.C., Sun, Z., Lu, A., Tour, J.M., 2010. Reduction of graphene oxide via bacterial respiration. ACS Nano 4, 4852–4856. http://dx.doi.org/10.1021/nn101081t.

Saleemi, M., 2014. Nano-EngineeredThermoelectric Materials for Waste Heat Recovery Doctoral dissertation. KTH Royal Institute of Technology.

Schmiedl, E., Wissmann, P., Finzel, H.U., 2008. The electrical resistivity of ultrathin copper films. Z. Naturf. Sect. A J. Phys. Sci. 63, 739–744. http://dx.doi.org/10.1515/zna-2008-10-1118.

Seki, Y., Takahashi, M., Takashiri, M., 2019. Effects of different electrolytes and film thicknesses on structural and thermoelectric properties of electropolymerized poly(3, 4-Ethylenedioxythiophene) films. RSC Adv. 9, 15957–15965. http://dx.doi.org/10.1039/c9ra02310k.

Settaluri, K.T., Lo, H., Ram, R.J., 2012. Thin thermoelectric generator system for body energy harvesting. J. Electron. Mater. 41, 984–988. http://dx.doi.org/10.1007/s11664-011-1834-3.

Shi, S., Sun, J., Zhang, J., Cao, Y., 2005. A novel application of the CuI thin film for preparing thin copper nanowires. Phys. B Condens. Matter. 362, 231–235. http://dx.doi.org/10.1016/j.physb.2005.02.019.

Shy, J.H., Tseng, B.H., 2005. Characterization of CuAlO2 thin film prepared by rapid thermal annealing of an Al2O3/Cu2O/sapphire structure. J. Phys. Chem. Solids. 66, 2123–2126. http://dx.doi.org/10.1016/j.jpcs.2005.09.062.

Siddique, A.R.M., Mahmud, S., Van Heyst, B., 2017. A review of the state of the science on wearable thermoelectric power generators (TEGs) and their existing challenges. Renew. Sustain. Energy Rev. 73, 730–744. http://dx.doi.org/10.1016/j.rser.2017.01.177.

Sirimanne, P.M., Rusop, M., Shirata, T., Soga, T., Jimbo, T., 2003. Characterization of CuI thin films prepared by different techniques. Mater. Chem. Phys. 80, 461–465. http://dx.doi.org/10.1016/S0254-0584(02)00547-3.

Snyder, G.J., Toberer, E.S., 2010. Complex thermoelectric materials. Mater. Sustain. Energy A Collect. Peer-Rev. Res. Rev. Artic. Nat. Publ. Gr. 7, 101–110. http://dx.doi.org/10.1142/9789814317665_0016.

Soleimani, Z., Zoras, S., Ceranic, B., Shahzad, S., Cui, Y., 2020. A review on recent developments of thermoelectric materials for room-temperature applications. Sustain. Energy Technol. Assess. 37, 100604. http://dx.doi.org/10.1016/j.seta.2019.100604.

Song, Q., Xia, S., Chen, S., Cui, Z., 2004. A new structure for measuring the thermal conductivity of thin film. In: Proc. 2004 Int. Conf. Inf. Acquis. ICIA 2004. pp. 77–79. http://dx.doi.org/10.1109/icia.2004.1373323.

Soni, A., Shen, Y., Yin, M., Zhao, Y., Yu, L., Hu, X., Dong, Z., Khor, K.A., Dresselhaus, M.S., Xiong, Q., 2012. Interface driven energy filtering of thermoelectric power in spark plasma sintered Bi 2Te 2.7Se 0.3 nanoplatelet composites. Nano Lett. 12, 4305–4310. http://dx.doi.org/10.1021/nl302017w.

Suarez, F., Nozariasbmarz, A., Vashaee, D., Öztürk, M.C., 2016. Designing thermoelectric generators for self-powered wearable electronics. Energy Environ. Sci. 9, 2099–2113. http://dx.doi.org/10.1039/c6ee00456c.

Tan, Q., Zhao, L.D., Li, J.F., Wu, C.F., Wei, T.R., Xing, Z.B., Kanatzidis, M.G., 2014. Thermoelectrics with earth abundant elements: Low thermal conductivity and high thermopower in doped SnS. J. Mater. Chem. A. 2, 17302–17306. http://dx.doi.org/10.1039/c4ta04462b.

Tappura, K., Jaakkola, K., 2018. A thin-film thermoelectric generator for large-area applications. Proceedings 2, 779. http://dx.doi.org/10.3390/proceedings2130779.

Tappura, K., Juntunen, T., Jaakkola, K., Ruoho, M., Tittonen, I., Ritasalo, R., Pudas, M., 2020. Large-area implementation and critical evaluation of the material and fabrication aspects of a thin-film thermoelectric generator based on aluminum-doped zinc oxide. Renew. Energy 147, 1292–1298. http://dx.doi.org/10.1016/j.renene.2019.09.093.

Terasaki, I., 2005. Introduction to thermoelectricity. Mater. Energy Convers. Devices 339–357. http://dx.doi.org/10.1533/9781845690915.3.339.

Tervo, J., Manninen, A., Ilola, R., Hänninen, H., 2009. State-of-the-art of thermoelectric materials - processing. In: Properties and Applications.

Tung, V.C., Kim, J., Cote, L.J., Huang, J., 2011. Sticky interconnect for solution-processed tandem solar cells. J. Am. Chem. Soc. 133, 9262–9265. http://dx.doi.org/10.1021/ja203464n.

Twaha, S., Zhu, J., Yan, Y., Li, B., 2016. A comprehensive review of thermoelectric technology: Materials, applications, modelling and performance improvement. Renew. Sustain. Energy Rev. 65, 698–726. http://dx.doi.org/10.1016/j.rser.2016.07.034.

Uhl, S., Pellet, M., Tschanz, J., Laux, E., Journot, T., Jeandupeux, L., Keppner, H., 2015. Fabrication of highly-integrated thermoelectric generators based on ionic liquids. Mater. Today Proc. 2, 669–674. http://dx.doi.org/10.1016/j.matpr.2015.05.084.

Van Toan, N., Tuoi, T.T.K., Ono, T., 2020. Thermoelectric generators for heat harvesting: From material synthesis to device fabrication. Energy Convers. Manag. 225, 113442. http://dx.doi.org/10.1016/j.enconman.2020.113442.

Viet Vu, D., Hai Le, D., Xuan Nguyen, C., Quang Trinh, T., 2019. Comparison of structural and electric properties of ZnO-based n-type thin films with different dopants for thermoelectric applications. J. Sol-Gel Sci. Technol. 91, 146–153. http://dx.doi.org/10.1007/s10971-019-05024-0.

Vora-ud, A., Chaarmart, K., Kasemsin, W., Boonkirdram, S., Seetawan, T., 2022. Transparent thermoelectric properties of copper iodide thin films. Phys. B Condens. Matter. 625, 413527. http://dx.doi.org/10.1016/j.physb.2021.413527.

Wan, C., Wang, Y., Wang, N., Norimatsu, W., Kusunoki, M., Koumoto, K., 2010. Development of novel thermoelectric materials by reduction of lattice thermal conductivity. Sci. Technol. Adv. Mater. 11, http://dx.doi.org/10.1088/1468-6996/11/4/044306.

Wang, J., Li, J., Li, S.S., 2011a. Native p-type transparent conductive CuI via intrinsic defects. J. Appl. Phys. 110, http://dx.doi.org/10.1063/1.3633220.

Wang, J., Li, G., Li, L., 2016. Synthesis strategies about 2D materials. Two-Dimensional Mater. - Synth. Charact. Potential Appl. 1–20. http://dx.doi.org/10.5772/63918.

Wang, X., Suwardi, A., Lim, S.L., Wei, F., Xu, J., 2020a. Transparent flexible thin-film p–n junction thermoelectric module. Npj Flex. Electron. 4, 1–9. http://dx.doi.org/10.1038/s41528-020-00082-9.

Wang, Y., Yang, L., Shi, X.L., Shi, X., Chen, L., Dargusch, M.S., Zou, J., Chen, Z.G., 2019. Flexible thermoelectric materials and generators: Challenges and innovations. Adv. Mater. 31, 1–47. http://dx.doi.org/10.1002/adma.201807916.

Wang, Y., Zhu, W., Deng, Y., Fu, B., Zhu, P., Yu, Y., Li, J., Guo, J., 2020b. Self-powered wearable pressure sensing system for continuous healthcare monitoring enabled by flexible thin-film thermoelectric generator. Nano Energy. 73, http://dx.doi.org/10.1016/j.nanoen.2020.104773.

Webb, P., 1992. Temperatures of skin, subcutaneous tissue, muscle and core in resting men in cold, comfortable and hot conditions. Eur. J. Appl. Physiol. Occup. Physiol. 64, 471–476. http://dx.doi.org/10.1007/BF00625070.

Yadav, A., Deshmukh, P.C., Roberts, K., Jisrawi, N.M., Valluri, S.R., 2019. An analytic study of the Wiedemann–Franz law and the thermoelectric figure of merit. J. Phys. Commun. 3, 13. http://dx.doi.org/10.1088/2399-6528/ab444a.

Yamada, N., Ino, R., Ninomiya, Y., 2016. Truly transparent p-type γ-CuI thin films with high hole mobility. Chem. Mater. 28, 4971–4981. http://dx.doi.org/10.1021/acs.chemmater.6b01358.

Yamada, N., Ino, R., Tomura, H., Kondo, Y., Ninomiya, Y., 2017. High-mobility transparent p-type CuI semiconducting layers fabricated on flexible plastic sheets: Toward flexible transparent electronics. Adv. Electron. Mater. 3, http://dx.doi.org/10.1002/aelm.201700298.

Yang, H., Kannappan, S., Pandian, A.S., Jang, J.-H., Lee, Y.S., Lu, W., 2017a. Graphene supercapacitor with both high power and energy density. Nanotechnology 28, 445401. http://dx.doi.org/10.1088/1361-6528/aa8948.

Yang, C., Kneib, M., Lorenz, M., Grundmann, M., 2016a. Room-temperature synthesized copper iodide thin filmas degenerate p-type transparent conductor with a boosted figure of merit. Proc. Natl. Acad. Sci. USA 113, 12929–12933. http://dx.doi.org/10.1073/pnas.1613643113.

Yang, C., Kneiß, M., Schein, F.L., Lorenz, M., Grundmann, M., 2016b. Room-temperature domain-epitaxy of copper iodide thin films for transparent CuI/ZnO heterojunctions with high rectification ratios larger than 109. Sci. Rep. 6, 1–8. http://dx.doi.org/10.1038/srep21937.

Yang, S., Qiu, P., Chen, L., Shi, X., 2021. Recent developments in flexible thermoelectric devices. Small Sci. 1, 2100005. http://dx.doi.org/10.1002/smsc.202100005.

Yang, G., Sang, L., Mitchell, D.R.G., Fei Yun, F., Wai See, K., Jumlat Ahmed, A., Sayyar, S., Bake, A., Liu, P., Chen, L., Yue, Z., Cortie, D., Wang, X., 2022. Enhanced thermoelectric performance and mechanical strength of n-type BiTeSe materials produced via a composite strategy. Chem. Eng. J. 428, 131205. http://dx.doi.org/10.1016/j.cej.2021.131205.

Yang, C., Souchay, D., Kneiß, M., Bogner, M., Wei, H.M., Lorenz, M., Oeckler, O., Benstetter, G., Fu, Y.Q., Grundmann, M., 2017b. Transparent flexible thermoelectric material based on non-toxic earth-abundant p-type copper iodide thin film. Nature Commun. 8, 4–10. http://dx.doi.org/10.1038/ncomms16076.

Yang, J., Xi, L., Qiu, W., Wu, L., Shi, X., Chen, L., Yang, J., Zhang, W., Uher, C., Singh, D.J., 2016c. On the tuning of electrical and thermal transport in thermoelectrics: an integrated theory–experiment perspective. Npj Comput. Mater. 2, 15015. http://dx.doi.org/10.1038/npjcompumats.2015.15.

Yoon, S.M., Madavali, B., Yoon, Y.N., Hong, S.J., 2017. Investigation of the microstructure and thermoelectric properties of P-type BiSbTe alloys by usage of different revolutions per minute (RPM) during mechanical milling. Arch. Metall. Mater. 62, 1167–1171. http://dx.doi.org/10.1515/amm-2017-0171.

Yu, Y., Zhu, W., Kong, X., Wang, Y., Zhu, P., Deng, Y., 2020. Recent development and application of thin-film thermoelectric cooler. Front. Chem. Sci. Eng. 14, 492–503. http://dx.doi.org/10.1007/s11705-019-1829-9.

Yue, S., Gu, M., Liu, X., Zhang, J., Huang, S., Liu, B., Ni, C., 2017. Effect of ZnI2 cosolute on quality and performance of γ-CuI ultrafast scintillation crystal grown via evaporation method in acetonitrile solvent. Opt. Mater. (Amst). 66, 308–313. http://dx.doi.org/10.1016/j.optmat.2016.12.030.

Zebarjadi, M., Esfarjani, K., Dresselhaus, M.S., Ren, Z.F., Chen, G., 2012. Perspectives on thermoelectrics: From fundamentals to device applications. Energy Environ. Sci. 5, 5147–5162. http://dx.doi.org/10.1039/c1ee02497c.

Zeng, F., Zhao, X., Luo, M., Wang, W., Qing, X., Lu, Y., Zhong, W., Liu, Q., Luo, J., Li, M., Wang, D., 2022. A transparent PEDOT:PSS/PVA-co-PE/epoxy thermoelectric composite device with excellent flexibility and environmental stability. Compos. Sci. Technol. 218, 109153. http://dx.doi.org/10.1016/j.compscitech.2021.109153.

Zhang, Q., Ai, X., Wang, L., Chang, Y., Luo, W., Jiang, W., Chen, L., 2015. Improved thermoelectric performance of silver nanoparticles-dispersed Bi2Te3composites deriving from hierarchical two-phased heterostructure. Adv. Funct. Mater. 25, 966–976. http://dx.doi.org/10.1002/adfm.201402663.

Zhang, T., Chen, H., Zheng, X., 2020a. Fiber-based infrasound sensing. In: Adv. Fiber Sens. Technol.. pp. 81–98. http://dx.doi.org/10.1007/978-981-15-5507-7_5.

Zhang, Z., Guo, Y., Robertson, J., 2020b. Electronic structure of amorphous copper iodide: A p -type transparent semiconductor. Phys. Rev. Mater. 4, 54603. http://dx.doi.org/10.1103/PhysRevMaterials.4.054603.

Zhang, S., Sakane, M., Nagasawa, T., Kobayashi, K., 2011. Mechanical properties of copper thin films used in electronic devices. Procedia Eng. 10, 1497–1502. http://dx.doi.org/10.1016/j.proeng.2011.04.250.

Zhang, L., Shi, X.L., Yang, Y.L., Chen, Z.G., 2021. Flexible thermoelectric materials and devices: From materials to applications. Mater. Today. 46, 62–108. http://dx.doi.org/10.1016/j.mattod.2021.02.016.

Zhang, K.X., Wang, S.W., Bai, L.Y., Wang, Y., Ou, K., Zhang, Y.W., Yi, L.X., 2019. Defect energy level and transition mechanism of CuI thin film by low-temperature spectrum. J. Lumin. 214, 116522. http://dx.doi.org/10.1016/j.jlumin.2019.116522.

Zhang, Z., Zhang, Y., Sui, X., Li, W., Xu, D., 2020c. Performance of thermoelectric power-generation system for sufficient recovery and reuse of heat accumulated at cold side of TEG with water-cooling energy exchange circuit. Energies 13, http://dx.doi.org/10.3390/en13215542.

Zhang, X., Zhao, L.D., 2015. Thermoelectric materials: Energy conversion between heat and electricity. J. Mater. 1, 92–105. http://dx.doi.org/10.1016/j.jmat.2015.01.001.

Zhao, X., Han, W., Jiang, Y., Zhao, C., Ji, X., Kong, F., Xu, W., Zhang, X., 2019a. A honeycomb-like paper-based thermoelectric generator based on a Bi2Te3/bacterial cellulose nanofiber coating. Nanoscale 11, 17725–17735. http://dx.doi.org/10.1039/c9nr06197e.

Zhao, X., Han, W., Zhao, C., Wang, S., Kong, F., Ji, X., Li, Z., Shen, X., 2019b. Fabrication of transparent paper-based flexible thermoelectric generator for wearable energy harvester using modified distributor printing technology. ACS Appl. Mater. Interfaces. 11, 10301–10309. http://dx.doi.org/10.1021/acsami.8b21716.

Zheng, X.F., Liu, C.X., Yan, Y.Y., Wang, Q., 2014. A review of thermoelectrics research - recent developments and potentials for sustainable and renewable energy applications. Renew. Sustain. Energy Rev. 32, 486–503. http://dx.doi.org/10.1016/j.rser.2013.12.053.

Zhu, W., Deng, Y., Wang, Y., Wang, A., 2013. Finite element analysis of miniature thermoelectric coolers with high cooling performance and short response time. Microelectron. J. 44, 860–868. http://dx.doi.org/10.1016/j.mejo.2013.06.013.